1991-06

A diagnostic study of the velocity structure of a meandering jet in the California current system using a primitive equation model

Mallette, James R.

Monterey, California. Naval Postgraduate School

NAVAL POSTGRADUATE SCHOOL

Monterey, California

THESIS

A DIAGNOSTIC STUDY OF THE VELOCITY STRUCTURE OF A MEANDERING JET IN THE CALIFORNIA CURRENT SYSTEM USING A PRIMITIVE EQUATION MODEL

James R. Mallette, Jr.

June, 1991

Thesis Advisor: Robert L. Haney

Approved for public release; distribution is unlimited

REPORT DOCUMENTATION PAGE

1a REPORT SECURITY CLASSIFICATION Unclassified	1b RESTRICTIVE MARKINGS
2a SECURITY CLASSIFICATION AUTHORITY	3 DISTRIBUTION/AVAILABILITY OF REPORT Approved for public release; distribution is unlimited.
2b DECLASSIFICATION/DOWNGRADING SCHEDULE	
4 PERFORMING ORGANIZATION REPORT NUMBER(S)	5 MONITORING ORGANIZATION REPORT NUMBER(S)
6a NAME OF PERFORMING ORGANIZATION Naval Postgraduate School 6b OFFICE SYMBOL (*If applicable*) 35	7a NAME OF MONITORING ORGANIZATION Naval Postgraduate School
6c ADDRESS (*City, State, and ZIP Code*) Monterey, CA 93943-5000	7b ADDRESS (*City, State, and ZIP Code*) Monterey, CA 93943-5000
8a NAME OF FUNDING/SPONSORING ORGANIZATION 8b OFFICE SYMBOL (*If applicable*)	9 PROCUREMENT INSTRUMENT IDENTIFICATION NUMBER
8c ADDRESS (*City, State, and ZIP Code*)	10 SOURCE OF FUNDING NUMBERS Program Element No / Project No / Task No / Work Unit Accession Number

11 TITLE (*Include Security Classification*)
A DIAGNOSTIC STUDY OF THE VELOCITY STRUCTURE OF A MEANDERING JET IN THE CALIFORNIA CURRENT SYSTEM USING A PRIMITIVE EQUATION MODEL

12 PERSONAL AUTHOR(S) James R. Mallette, Jr.

13a TYPE OF REPORT	13b TIME COVERED	14 DATE OF REPORT (*year, month, day*)	15 PAGE COUNT
Master's Thesis	From To	June 1991	99

16 SUPPLEMENTARY NOTATION
The views expressed in this thesis are those of the author and do not reflect the official policy or position of the Department of Defense or the U.S. Government.

17 COSATI CODES			18 SUBJECT TERMS (*continue on reverse if necessary and identify by block number*)
FIELD	GROUP	SUBGROUP	diagnostic model, California Current, CTZ, dynamical modes

19 ABSTRACT (*continue on reverse if necessary and identify by block number*)

A high resolution 20-level, primitive equation model is initialized using sigma-theta data acquired during a Coastal Transition Zone (CTZ) cruise from 6 to 12 July 1988 near Point Arena, California for the purpose of diagnosing the three-dimensional dynamically balanced flow field for the region. The major feature in the region during the cruise period was a strong meandering jet which flowed equatorward and offshore, oriented in a northeast to southwest direction. A density diagnostic version of the model, in which the sigma-theta is held constant during the 72 hour integration time, is compared with a robust diagnostic version of the model, in which the sigma-theta field is allowed to adjust dynamically within the constraints of a damping time scale. The density diagnostic version of the model produces vertical velocities which are an order of magnitude larger than vertical velocities calculated from bio-optical data collected in the same location and at the same time as the CTZ cruise. The robust diagnostic version produced vertical velocities within the range of vertical velocities calculated from the bio-optical data. The horizontal pattern of vertical velocity from the robust diagnostic version also compared well with patterns seen in trough/ridge systems in the Gulf Stream. In particular, there is horizontal convergence and downwelling all along the offshore directed part of the meandering jet. Vertical cross-section comparisons between model velocity data and ADCP velocity data collected during the cruise revealed differences which may be caused by factors neglected by the model (e.g. bottom topography, wind forcing, and heat fluxes).

20 DISTRIBUTION/AVAILABILITY OF ABSTRACT	21 ABSTRACT SECURITY CLASSIFICATION	
☒ UNCLASSIFIED/UNLIMITED ☐ SAME AS REPORT ☐ DTIC USERS	Unclassified	
22a NAME OF RESPONSIBLE INDIVIDUAL R. L. Haney	22b TELEPHONE (*Include Area code*) (408) 646-5217	22c OFFICE SYMBOL Code MR/Hy

DD FORM 1473, 84 MAR — 83 APR edition may be used until exhausted; All other editions are obsolete

Approved for public release; distribution is unlimited.

A Diagnostic Study of the Velocity Structure of a Meandering Jet in the California Current System Using a Primitive Equation Model

by

James R. Mallette, Jr.
Lieutenant, United States Navy
B.S., University of Florida, 1978

Submitted in partial fulfillment
of the requirements for the degree of

MASTER OF SCIENCE IN METEOROLOGY AND PHYSICAL OCEANOGRAPHY

from the

NAVAL POSTGRADUATE SCHOOL
June 1991

Author: [redacted]
James R., Mallette, Jr.

Approved by: [redacted]
Robert L. Haney, Thesis Advisor

[redacted]
Timothy P. Stanton, Second Reader

[redacted]
Robert L. Haney, Chairman
Department of Meteorology

ABSTRACT

A high resolution 20-level, primitive equation model is initialized using sigma-θ (σ_θ) data acquired during a Coastal Transition Zone (CTZ) cruise from 6 to 12 July 1988 near Point Arena, California for the purpose of diagnosing the three-dimensional dynamically balanced flow field for the region. The major feature in the region during the cruise period was a strong meandering jet which flowed equatorward and offshore, oriented in a northeast to southwest direction. A density diagnostic version of the model, in which the σ_θ field is held constant during the 72 hour integration time, is compared with a robust diagnostic version of the model, in which the σ_θ field is allowed to adjust dynamically within the constraints of a damping time scale. The density diagnostic version of the model produces vertical velocities which are an order of magnitude larger than vertical velocities calculated from bio-optical data collected in the same location and at the same time as the CTZ cruise. The robust diagnostic version produced vertical velocities within the range of vertical velocities calculated from the bio-optical data. The horizontal pattern of vertical velocity from the robust diagnostic version also compared well with patterns seen in trough/ridge systems in the Gulf Stream. In particular, there is horizontal convergence and downwelling all along the offshore directed part of the meandering jet. Vertical cross-section comparisons between model velocity data and ADCP velocity data collected during the cruise revealed differences which may be caused by factors neglected by the model (e.g. bottom topography, wind forcing, and heat fluxes).

TABLE OF CONTENTS

LIST OF TABLES

LIST OF FIGURES

ACKNOWLEDGEMENTS

I am indebted to Professor Robert L. Haney and Professor Timothy P. Stanton for their professional advice and guidance during the research and writing of this thesis. I also thank Mr. Robert Hale, staff meteorologist, for his help in solving various computer programming problems associated with the primitive equation model on which most of the results are based.

Finally, I am forever grateful to my family for the support I receive in whatever endeavor I undertake.

I. INTRODUCTION

A. BACKGROUND - THE CALIFORNIA CURRENT

The California Current is the southeastward extension of the North Pacific Drift which flows across the Pacific Ocean from west to east at about 45° N (Tchernia, 1980). This current flows toward the equator, and is considered a cold, eastern boundary current. It, along with three other currents, comprises the California Current System. The other three currents are: the California Undercurrent, the Davidson Current and the Southern California Countercurrent (Hickey, 1979). These currents are all poleward flowing, the Davidson Current and the Southern California Countercurrent being surface currents, and the California Undercurrent flowing beneath the surface. The Davidson Current is found north of Point Conception during the fall and winter. The Southern California Countercurrent exists to the south of Point Conception in the California Bight.

The California Current System impacts the west coast states climatically and economically. Upwelling associated with it brings colder, nutrient rich water to the surface, supporting marine life there (Brink, 1983; Huyer, 1983). The colder water at the surface also cools the relatively warm air flowing over it, producing mild weather conditions and fog along the coast (Foster, 1989).

Cold filaments, which occur in the California Current System from Vancouver Island to Point Conception, are of particular interest. These filaments consist of cold, salty inshore water which has been carried as far as 300-400 km offshore from the coast

(Strub and the CTZ Group, 1990). Infrared and visible color satellite images reveal these filaments in the California Current System as well as in other eastern boundary currents (Traganza et al, 1983; Abbott and Zion, 1985; Flament et al., 1985; Kelly, 1985).

The Coastal Transition Zone (CTZ) experiment examines some of these cold filaments in detail. Its purpose is to study the physical, chemical and biological structure of the filaments which occurred off the northern California coast during the spring and summer of 1987 and 1988 (Strub and the CTZ Group, 1990). The goals of the CTZ experiment are: understand the interaction processes between the cold filament water and the open ocean water; study the effect the filaments have on the biology and metereology of the coastal zone; develop maps of the current, hydrographic, nutrient, and particle fields; and use numerical models to investigate what driving forces, dynamics, topography and stratification is necessary to duplicate the observed characterisitcs of these filaments (CTZ Group, 1988).

B. OBJECTIVE

The objective of this thesis research is to diagnose the velocity fields obtained from a 20-level robust primitive equation model using sigma-θ (σ_θ) data from a cruise made during the 1988 CTZ field experiment. The cruise domain is from approximately 37°10′ to 39°21′N and 123°50′ to 126°40′W, and covers about one meander of the California Current.

The same domain and model, lacking the robust feature, were used previously to diagnose the velocity fields from temperature data collected during the same experiment (de Jesus, 1990).

II. DATA ACQUISITION AND PROCESSING

A. DATA ACQUISITION

Data from a Naval Postgraduate School cruise made from 6 to 12 July 1988 on the R/V POINT SUR that was part of the CTZ experiment are used here. This cruise is subsequently referred to as CTZR1.

Acoustic doppler current profiler (ADCP) data and conductivity, temperature and depth (CTD) data were collected during the cruise. CTD measurements were made with an NBIS CTD system. Temperature measurement accuracy and salinity measurement accuracy were about ±0.01 C and ±0.003 psu respectively. Data were collected to a depth of 500 m. The ADCP made by RD Instruments operated continuously during the cruise. The transducer had a nominal range of 350 m and operated at 150 kHz with a 4 m pulse length. Returning echoes were sampled selectively in 4 m bins to produce a vertically-averaged, ship relative velocity. Relative velocity profiles were made every three minutes. Reliable data were collected to depths as shallow as 25 m (Huyer et al., 1990; de Jesus, 1990).

The horizontal sampling grid spacing is nominally 25 by 40 km (Stanton et al., 1990). The actual station grid extends approximately 120 nm offshore and 110 nm alongshore, roughly parallel to the California coast and southwest of Point Arena (Figures 1 and 2). The alongshore sections are approximately 20 nm apart and have individual stations approximately 13 to 14 nm apart (de Jesus, 1990). Not all of the stations in the

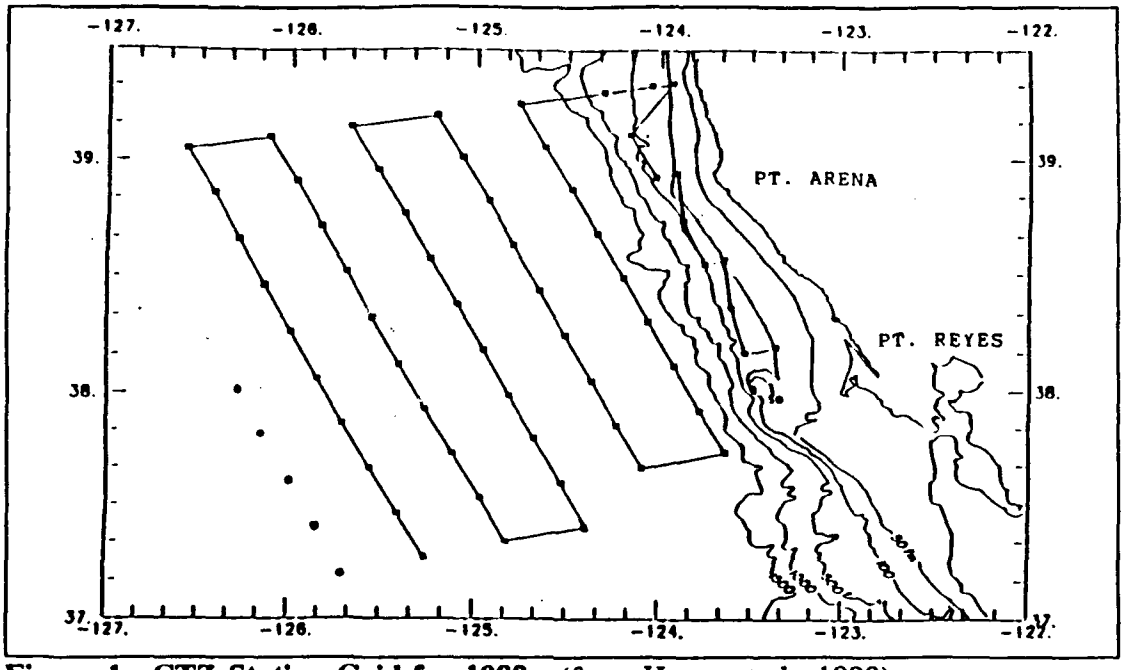

Figure 1. CTZ Station Grid for 1988: (from Huyer et al., 1990).

CTZ grid are included in the model domain to eliminate coastal effects (Figure 2) (de Jesus, 1990).

B. DATA PROCESSING

The sigma-θ (σ_θ) data were derived from the CTD data and objectively analyzed using the optimal interpolation method described, for example, by Carter and Robinson (1987). This method and some of the following procedures were similar to those used by de Jesus (1990) for temperature data, but with some differences as described below.

The spatial mean σ_θ profile for the cruise and, the objectively analyzed σ_θ at each of the points in a grid with 4 km horizontal spacing was obtained with a vertical spacing corresponding to the upper 7 levels of the numerical model as given in Table 1. This mean σ_θ profile was calculated at meter depth intervals in the upper 500 m, corresponding

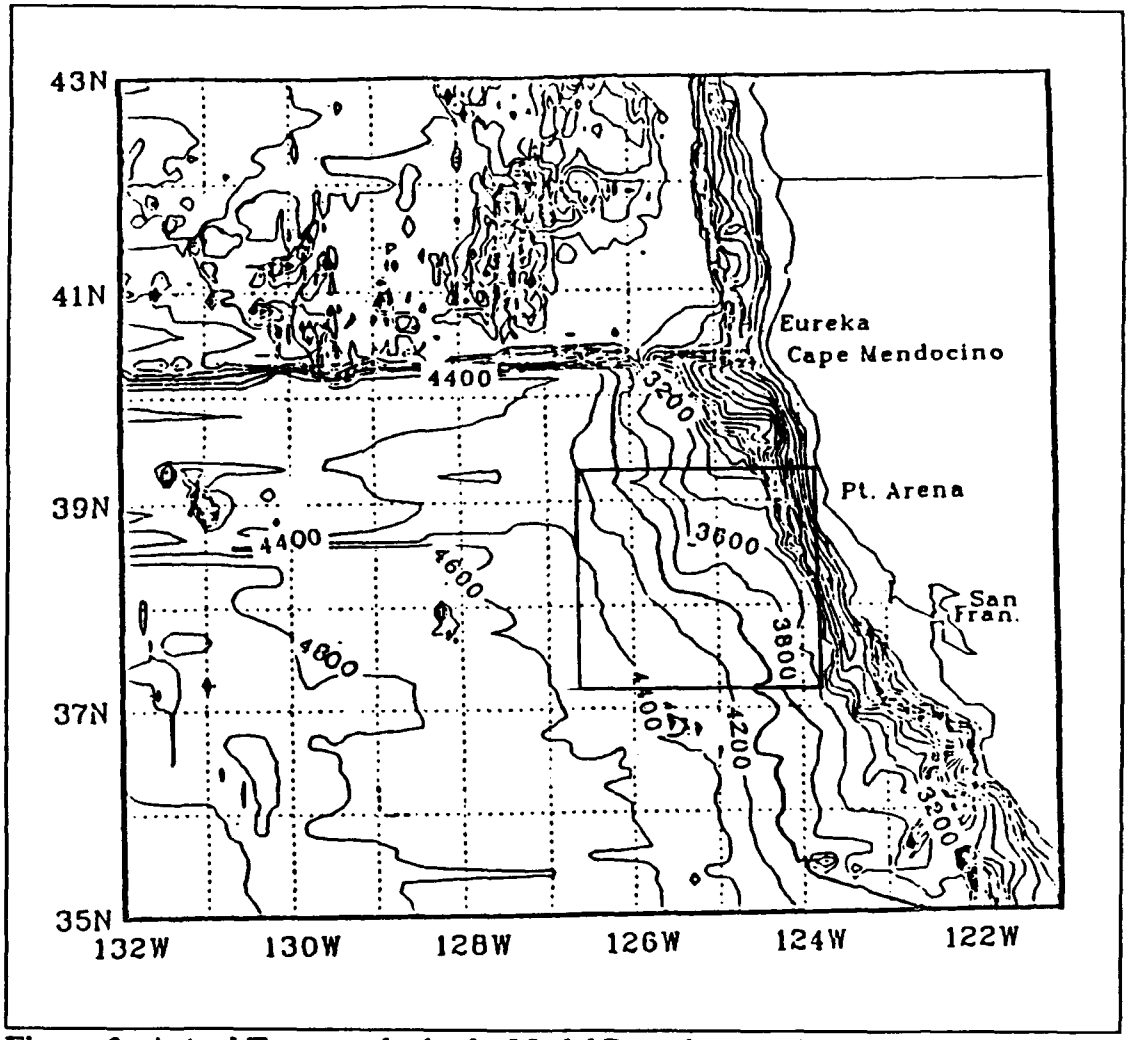

Figure 2. Actual Topography in the Model Domain: The box shows the area of the model domain. Depths are in meters.

to the depths at which observed data were collected, and then averaged in the vertical to every 10 m.

The mean σ_θ profile was extended to 4000 m by fitting an exponential curve to the mean profile in the upper 500 m using a centered difference scheme around 450 m. The σ_θ at 4000 m was left to be determined by the exponential curve, increasing the degrees

of freedom and allowing continuity of σ_θ and its vertical derivative at the interface between the observations and the extrapolation (i.e. at 450 m).

This extended mean σ_θ profile was used to calculate the first three dynamical vertical modes $\sigma_{\theta 1}(k)$, $\sigma_{\theta 2}(k)$, and $\sigma_{\theta 3}(k)$ following the procedure described in Rienecker et al. (1987) and outlined below.

The initial definition made was the perturbation

$$\sigma'_\theta(i,j,k) = \sigma_\theta(i,j,k) - \overline{\sigma}_\theta(k), \qquad \{1\}$$

where i, j, and k are the gridpoint indices for the x, y, and z directions, respectively, $\sigma_\theta'(i,j,k)$ is the perturbation part of σ_θ at the gridpoint, $\sigma_\theta(i,j,k)$ is the objectively analyzed σ_θ at the gridpoint, and $\overline{\sigma}_\theta(k)$ is the mean σ_θ at level k.

To extend the perturbation below 500 m, $\sigma_\theta'(i,j,k)$ is assumed to be a linear combination of the first three dynamical vertical modes, such that

$$\sigma'_\theta(i,j,k) = a_1(i,j)\sigma_{\theta 1}(k) + a_2(i,j)\sigma_{\theta 2}(k) + a_3(i,j)\sigma_{\theta 3}(k), \qquad \{2\}$$

where $a_1(i,j)$ is the weighting given to $\sigma_{\theta 1}(k)$, $a_2(i,j)$ is the weighting given to $\sigma_{\theta 2}(k)$ and $a_3(i,j)$ is the weighting given to $\sigma_{\theta 3}(k)$. Solutions for a_1, a_2, and a_3 at each horizontal grid point i,j need to be calculated.

The procedure for determining a_1, a_2, and a_3 followed by de Jesus (1990) involved solving a system of four equations in three unknowns (a_1, a_2, and a_3) using a linear least squares method. This procedure, referred to as the "mean conserving" formulation, was

also used here. In addition, two new procedures were used which gave different results for the vertical profiles below 500 meters. They were considered possibilities for better representing the physical condition of the ocean in the cruise domain.

The "mean conserving" formulation of the linear least squares method is outlined briefly as are the two new, possibly more physical, formulations. For the sake of comparison, vertical profiles of σ_θ' are calculated at representative (i,j) points using each of the three methods. Arguments are made concerning which of the three methods are considered the best for representing the characteristics of the ocean. Finally, an exact method of solving for a_1, a_2, and a_3 using four equations and four unknowns is compared with the linear least squares method, and arguments are made for using the linear least squares method instead of the exact method. These issues are discussed further below.

Following the "mean conserving" formulation of the linear least squares method, four equations are derived from equation {2}:

$$<\sigma'_\theta(i,j,k)> = a_1<\sigma_{\theta 1}(k)> + a_2<\sigma_{\theta 2}(k)> + a_3<\sigma_{\theta 3}(k)>, \qquad \{3\}$$

$$<\sigma_{\theta 1}(k)\sigma'_\theta(i,j,k)> = a_1<\sigma_{\theta 1}(k)\sigma_{\theta 1}(k)> + a_2<\sigma_{\theta 1}(k)\sigma_{\theta 2}(k)> + a_3<\sigma_{\theta 1}(k)\sigma_{\theta 3}(k)>, \qquad \{4\}$$

$$<\sigma_{\theta 2}(k)\sigma'_\theta(i,j,k)> = a_1<\sigma_{\theta 2}(k)\sigma_{\theta 1}(k)> + a_2<\sigma_{\theta 2}(k)\sigma_{\theta 2}(k)> + a_3<\sigma_{\theta 2}(k)\sigma_{\theta 3}(k)>, \qquad \{5\}$$

$$<\sigma_{\theta 3}(k)\sigma'_\theta(i,j,k)> = a_1<\sigma_{\theta 3}(k)\sigma_{\theta 1}(k)> + a_2<\sigma_{\theta 3}(k)\sigma_{\theta 2}(k)> + a_3<\sigma_{\theta 3}(k)\sigma_{\theta 3}(k)>. \qquad \{6\}$$

The bracketed (< >) terms are a vertical average, defined as

$$<Q> \equiv \sum_1^7 Q\ \Delta\ z(k)\ /\ \sum_1^7 \Delta\ z(k). \qquad \{7\}$$

where Q is any expression inside the brackets, $\Delta z(k)$ is the vertical thickness between adjacent k levels in the model, and the limits 1 and 7 with the summation sign correspond to levels 1 and 7 in the model(Table 1). Therefore, <Q> is the vertical average of Q(k) over the top seven levels of the model, which are encompassed by the analyzed observations (i.e. the upper 500 meters). Equation {3} is the statement of "conservation of the mean" in this formulation.

This system of four equations in three unknowns (a_1, a_2, a_3) is solved by the linear least squares method. This means that none of the four equations are satisfied exactly, but that there is a residual error in each one. After a_1, a_2, and a_3 are found for each i,j point in the domain of the model, equation {2} is used to find $\sigma_\theta'(i,j,k)$ for k = 8 to k = 20 (i.e. from 500 meters to 4000 meters) (Table 1). From Equation {1}, $\sigma_\theta(i,j,k)$ is found for all 20 levels in the model.

The first of the two new formulations alluded to above represents an energy-related approach to arriving at solutions for a_1, a_2, and a_3. It involves the replacement of equation {3} by

$$<\sigma_\theta'(i,j,k)\sigma_\theta'(i,j,k)> = a_1<\sigma_\theta'(i,j,k)\sigma_{\theta 1}(k)> + a_2<\sigma_\theta'(i,j,k)\sigma_{\theta 2}(k)> + a_3<\sigma_\theta'(i,j,k)\sigma_{\theta 3}(k)>. \qquad \{8\}$$

The $\sigma_\theta'^2$ on the left hand side of the equation is an energy term. Since this equation puts a constraint on the energy of the σ_θ' in the upper ocean where the observations occur, this is called the "energy conserving" formulation of the problem.

The second of the new formulations puts a constraint on the continuity of σ_θ' at the interface between the observations and the region of extrapolation below. In this case, the interface occurs at level 7 in the model. Therefore, equation {3} is replaced by

$$\sigma_\theta'(i,j,7) = a_1\sigma_{\theta 1}(7) + a_2\sigma_{\theta 2}(7) + a_3\sigma_{\theta 3}(7). \qquad \{9\}$$

Because of the constraint at the interface, this is called the "interface matching" formulation. Since both of the new formulations are also solved using a linear least squares method, there is a residual error in each equation as there is with the first formulation.

When comparing the results of vertical profiles using these three formulations, differences among them can readily be seen. In the CTZR1 cruise domain, two points where σ_θ' is large in the upper levels of the ocean are used to illustrate these differences (Figures 4 and 5).

The (i,j) gridpoint (27,36), which is approximately map coordinate (x,y) point (110,144) in Figure 3, is located in a region of low density water, with $\sigma_\theta < 24.4$ kg/m^3 at 65 m. Figure 4 shows the vertical profile of σ_θ' at this point for the three different formulations of the linear least squares solution to a_1, a_2, and a_3 in equation {2}. Clearly, the observed profiles in the upper 500 meters are the same in each case. Also, below about 2000 meters the profiles are the same. In the deep ocean, the water characteristics are such that the dynamical modes are all small in amplitude so that changing the formulation of the solution does not affect the profile. Between these two levels, the three formulations produce three different profiles. The σ_θ' profile for the "interface

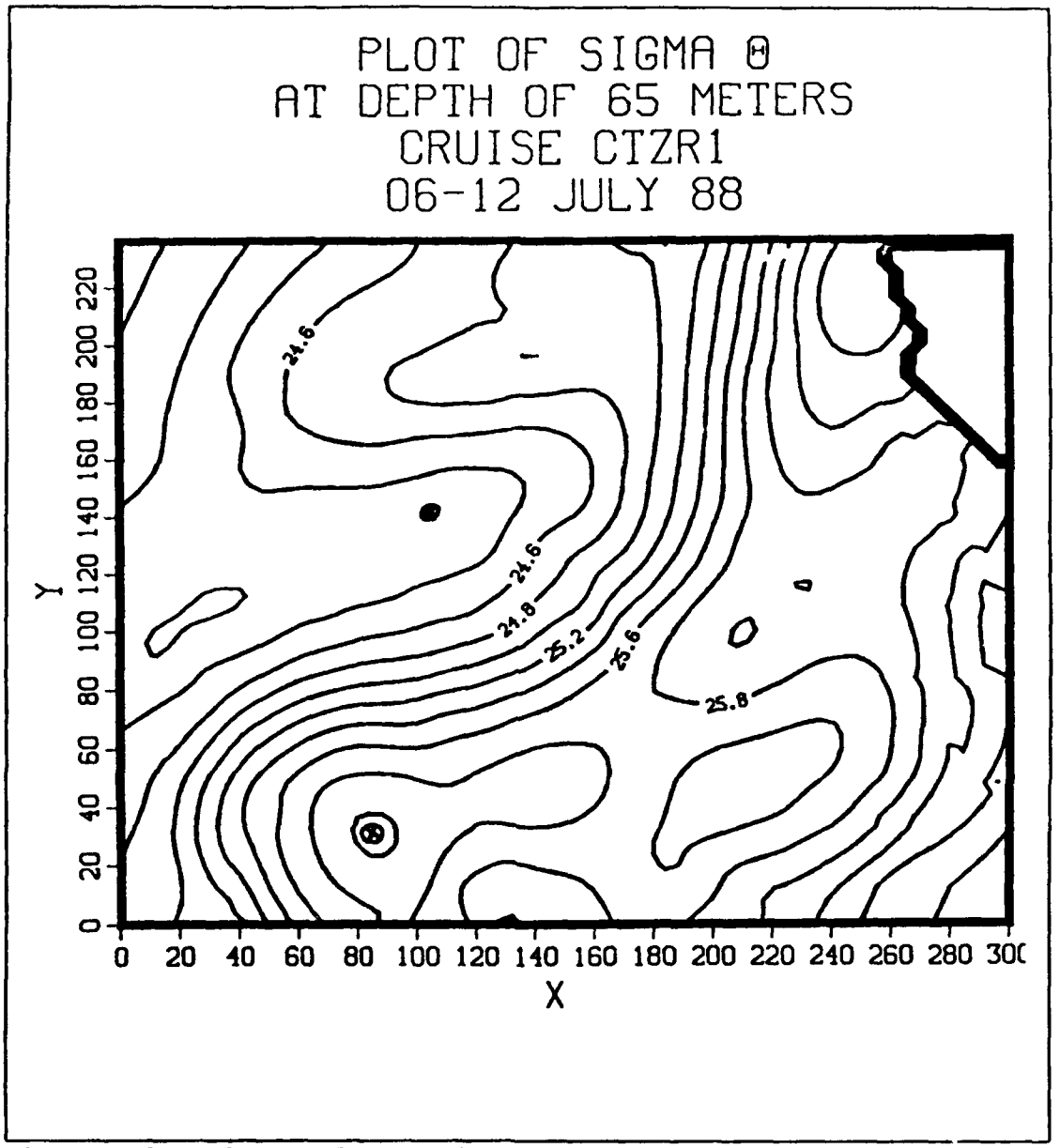

Figure 3. Plot of σ_θ at 65 Meters Depth(Model Level 3), Cruise CTZR1, 06-12 July 1988: The two points of interest are marked.

matching" formulation has the smallest amplitude of all. The constraint on having continuity at the interface between the observations and the extrapolation is the cause of this reduced amplitude. The "energy conserving" formulation is also smaller in amplitude

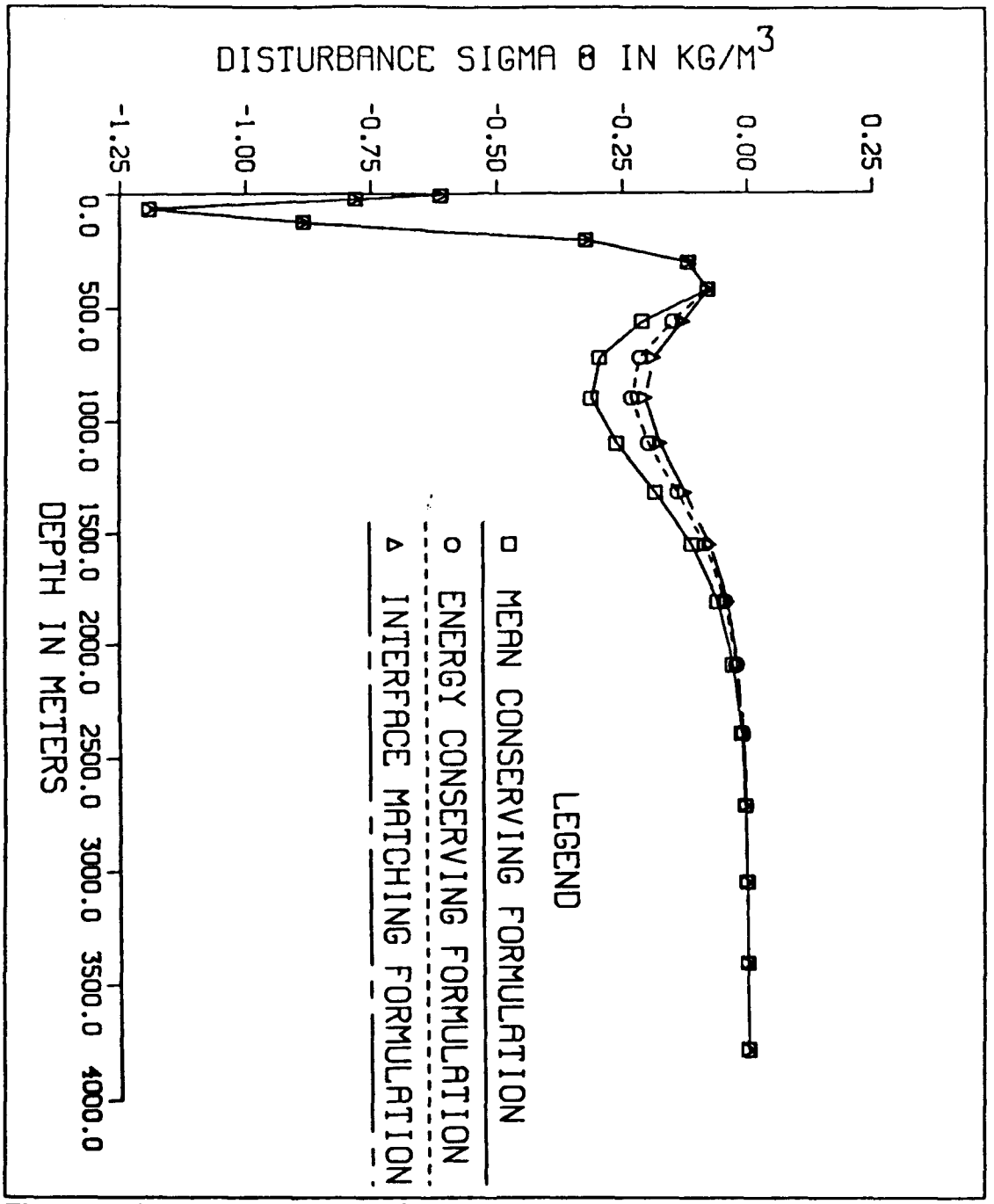

Figure 4. Vertical Profiles of σ_θ' at Map Coordinate Point (110,144): The symbols(located at the 20 model levels) and the lines for each formulation are given by the legend.

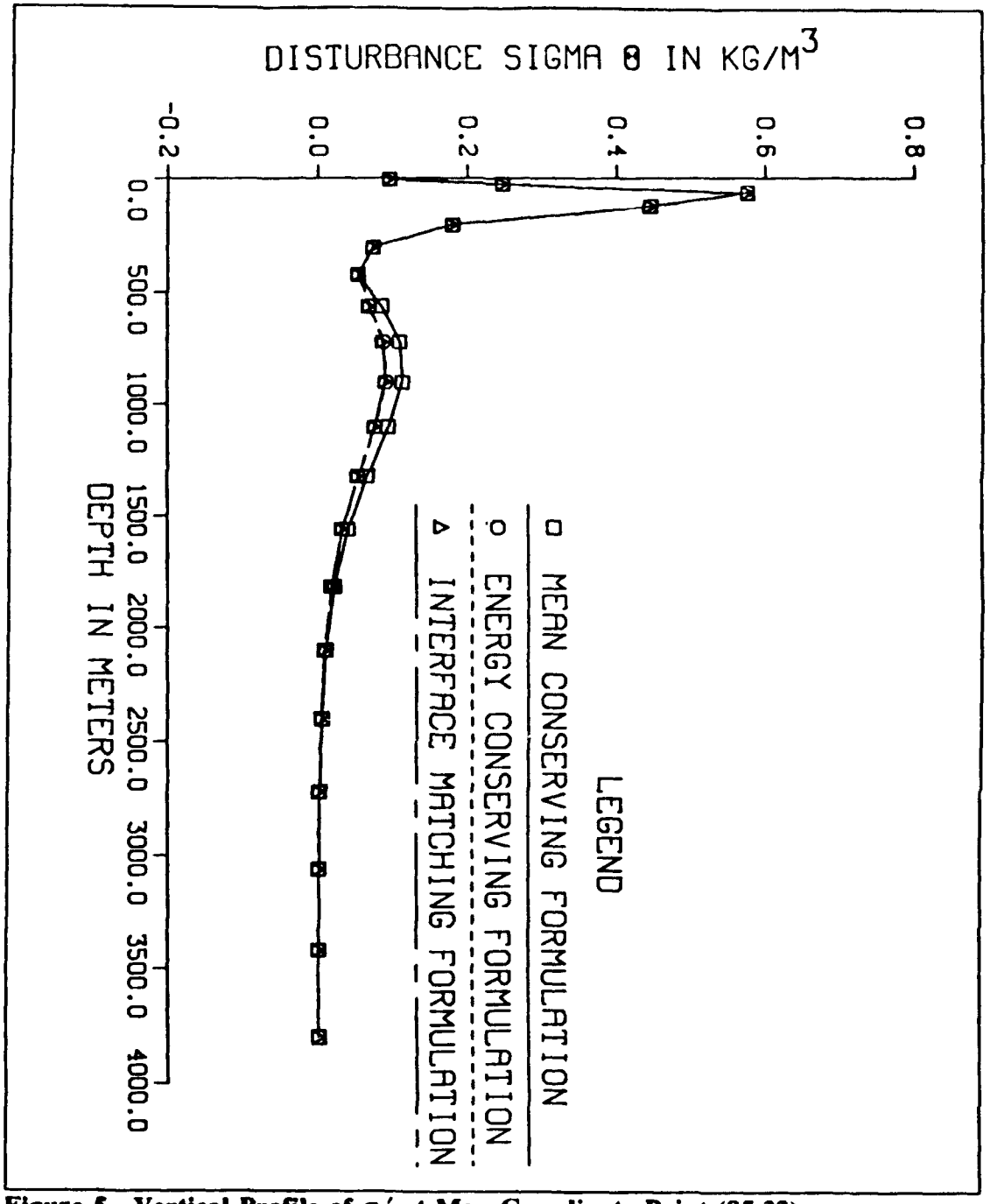

Figure 5. Vertical Profile of σ_θ' at Map Coordinate Point (85,32): The legend is the same as in Figure 4.

than the "mean conserving" formulation of the solution. Comparing the profiles in Figure 4 with the three vertical dynamical modes shown in Figure 6 suggests that mode 2 and mode 3 are the main contributors to the structure of the vertical profile of σ_θ' at the level between 500 and 2000 meters.

The (i,j) gridpoint (21,8), which roughly corresponds to map coordinate (x,y) point (85,32), is in an area of high density water at 65 m as shown in Figure 3. The vertical profiles of the three formulations at this point are not as distinctly different as those at point (110,144) as seen when comparing Figure 5 with Figure 4. At point (85,32), the "interface matching" formulation and the "energy conserving" formulation have a smaller amplitude than the "mean conserving" formulation in the level between 500 meters and 2000 meters. This illustrates the differences among the points in the cruise domain resulting from the 3 different extrapolation formulations. On the other hand, the similarities of the profiles above 500 meters and below 2000 meters can be explained using the arguments made previously for point (110,144).

Of the three formulations described above, which is the "best" to use for input into the model? The "mean conserving" formulation suffers because it places no constraint on the amplitude of σ_θ'. The best example of this is a sine wave. The mean of a sine wave is the same no matter what its amplitude. The "energy conserving" formulation may alias high wave number energy observed in the upper 500 m (which actually belong to higher dynamical modes) onto the lower wave number modes, which is due to the energy dependence caused by the squared term on the left-hand side of equation (8). This would tend to increase the amplitude of σ_θ' compared to a method that did not alias

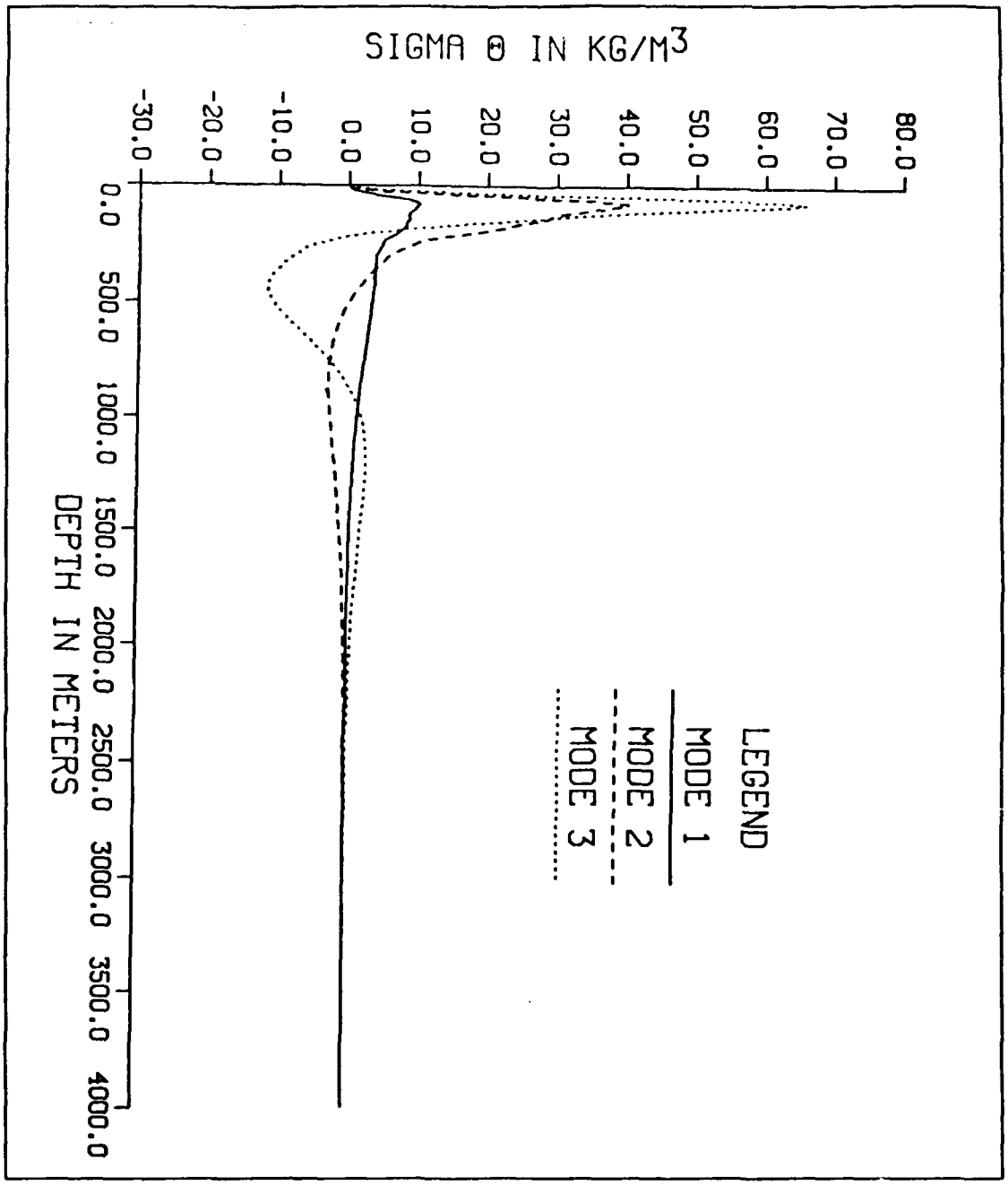

Figure 6. First Three Vertical Dynamical Modes of σ_θ for CTZR1: Computed from the extended spatial mean vertical profile of σ_θ calculated from the objective analysis.

the high wave number variability into the solution. Therefore, the "interface matching" formulation seems to be the "best" to use for the model. As stated above, it places a constraint on the σ_θ' at the interface between the observed data and the extrapolated data, and does not alias high wave number variability onto the three low wave number modes. The problems associated with the other two methods are, therefore, eliminated. However, before a definite conclusion can be made about the relative ability of these formulations to depict sub-500 m variability, they should be tested with full water column observed data. Because of the arguments given above, the "interface matching" formulation is used in this study. Maps of a_1, a_2, and a_3 using the "interface matching" formulation are shown in Figures 7, 8, and 9. These modal amplitudes have large spatial coherence, and their patterns closely correspond to the σ_θ field in Figure 3.

The problem of solving for a_1, a_2, and a_3 in equation {2} could have been done exactly with four equations and four unknowns using variational techniques found in Hildebrand (1965). In Hildebrand (1965; see pp. 119-121), it is shown that the problem of determining a_1, a_2 and a_3 that minimizes the root mean square difference between the observed σ_θ' and the σ_θ' given by {2} in the upper 500 m subject to the constraint {9}, can be expressed as an unconstrained minimization problem which leads to the following four equations

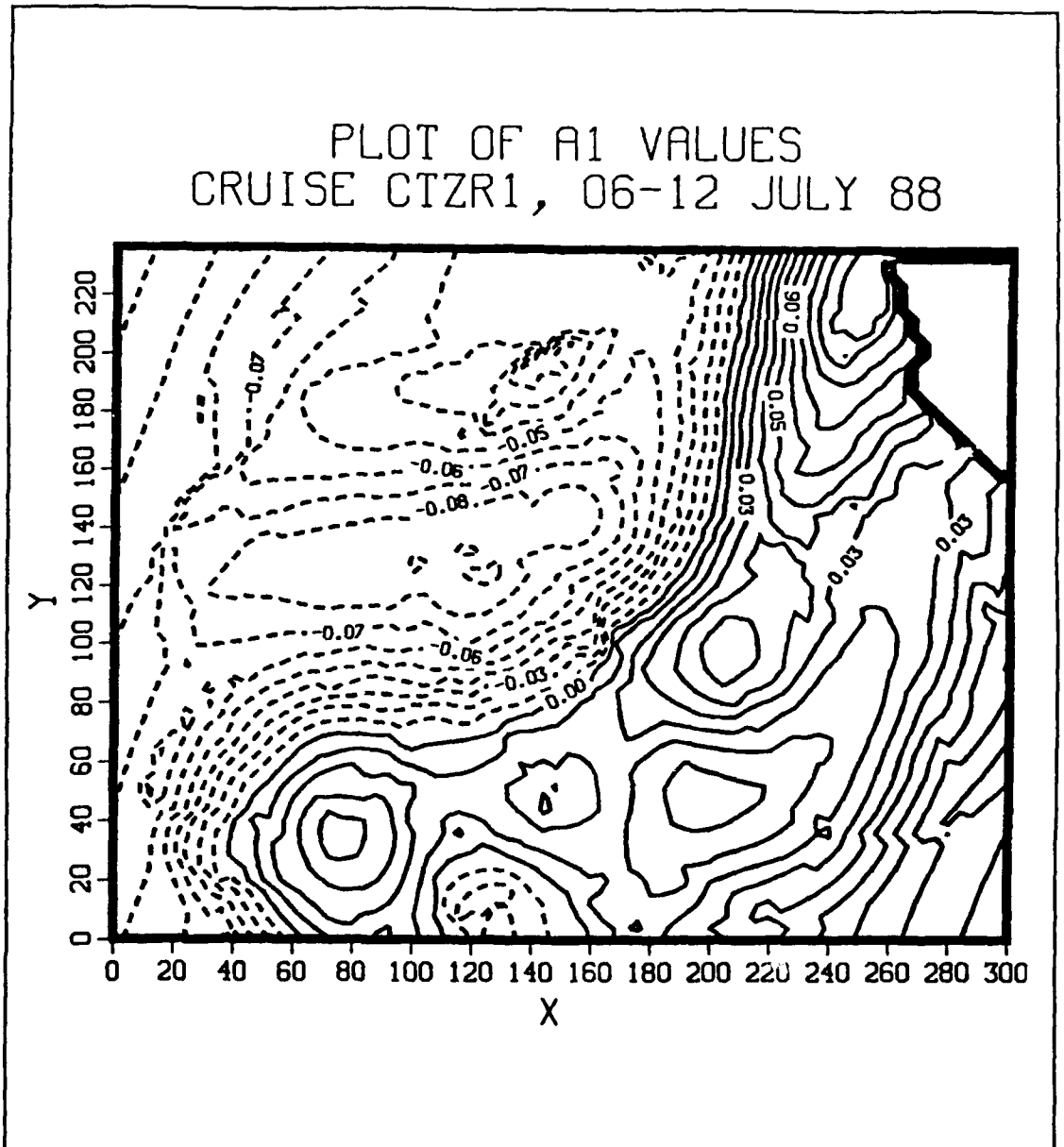

Figure 7. Plot of A_1 Values, Cruise CTZR1: Obtained from "interface matching" formulation described in text.

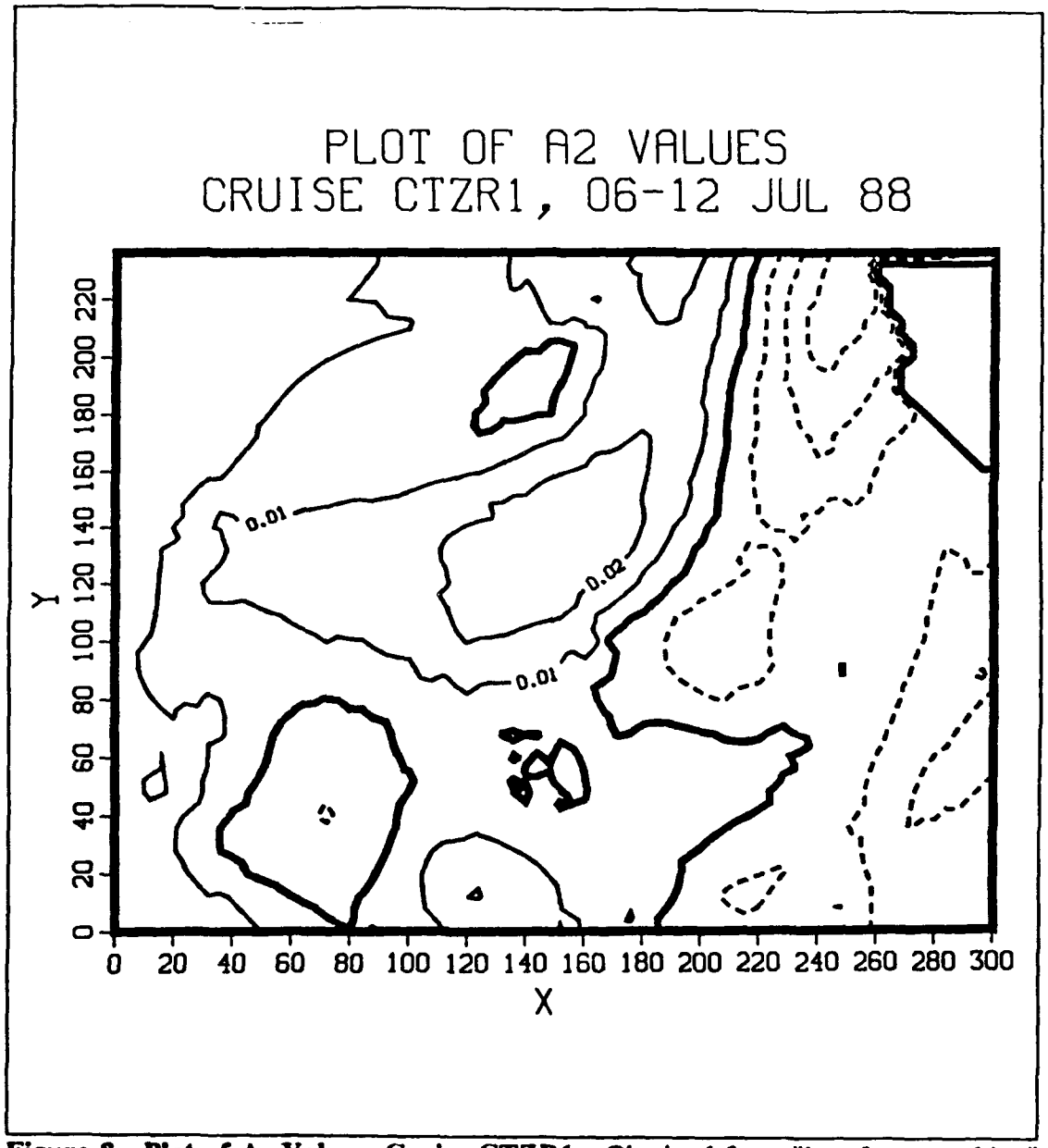

Figure 8. Plot of A_2 Values, Cruise CTZR1: Obtained from "interface matching" formulation described in text.

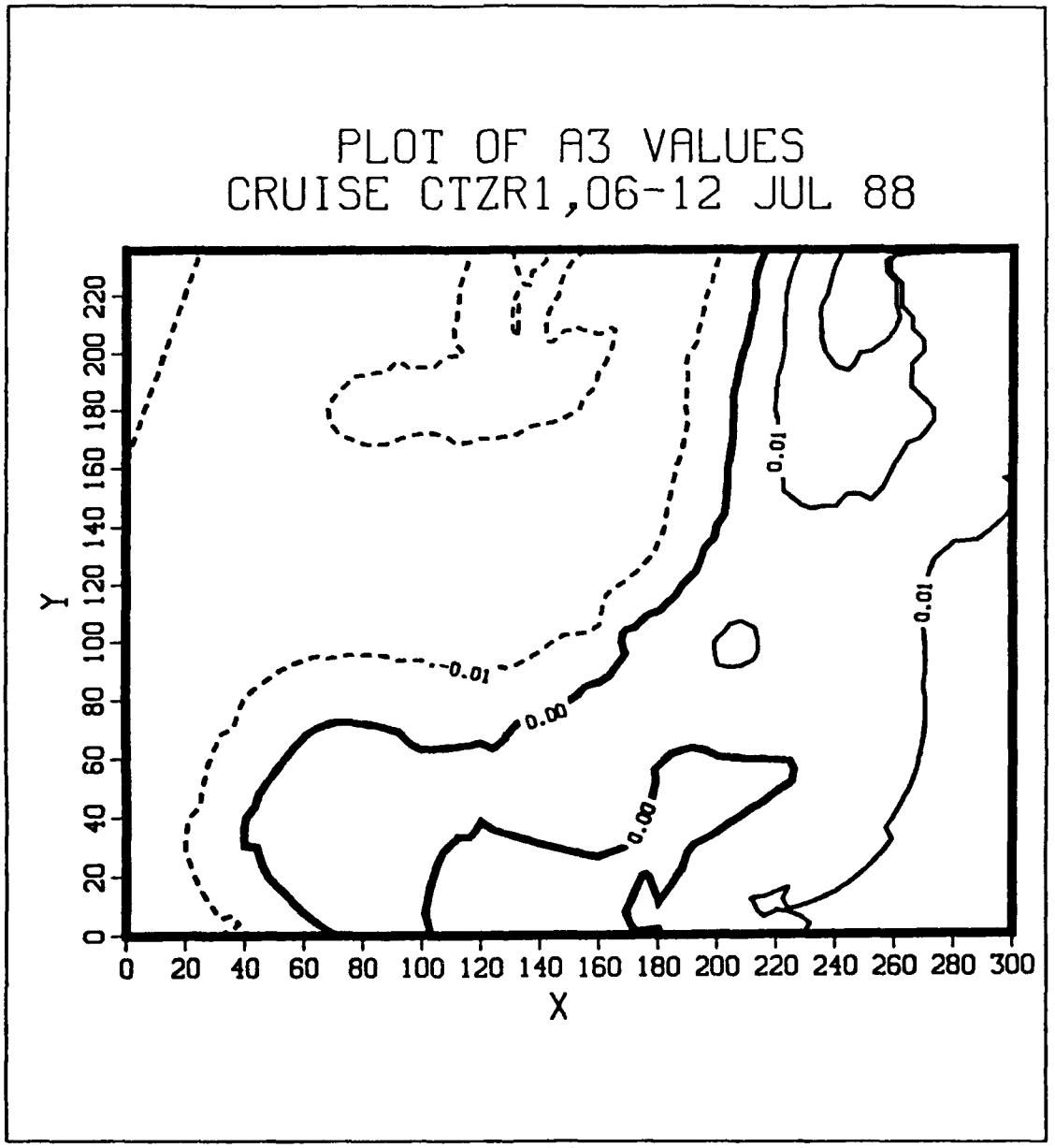

Figure 9. Plot of A_3 Values, Cruise CTZR1: Obtained from "interface matching" formulation described in text.

$$\sigma'_\theta(i,j,7) = a_1\sigma_{\theta 1}(7) + a_2\sigma_{\theta 2}(7) + a_3\sigma_{\theta 3}(7), \quad \{10\}$$

$$\langle\sigma_{\theta 1}(k)\sigma'_\theta(i,j,k)\rangle = a_1\langle\sigma_{\theta 1}(k)\sigma_{\theta 1}(k)\rangle + a_2\langle\sigma_{\theta 1}(k)\sigma_{\theta 2}(k)\rangle + a_3\langle\sigma_{\theta 1}(k)\sigma_{\theta 3}(k)\rangle - \frac{\lambda}{2}\sigma_{\theta 1}(7), \quad \{11\}$$

$$\langle\sigma_{\theta 2}(k)\sigma'_\theta(i,j,k)\rangle = a_1\langle\sigma_{\theta 2}(k)\sigma_{\theta 1}(k)\rangle + a_2\langle\sigma_{\theta 2}(k)\sigma_{\theta 2}(k)\rangle + a_3\langle\sigma_{\theta 2}(k)\sigma_{\theta 3}(k)\rangle - \frac{\lambda}{2}\sigma_{\theta 2}(7), \quad \{12\}$$

$$\langle\sigma_{\theta 3}(k)\sigma'_\theta(i,j,k)\rangle = a_1\langle\sigma_{\theta 3}(k)\sigma_{\theta 1}(k)\rangle + a_2\langle\sigma_{\theta 3}(k)\sigma_{\theta 2}(k)\rangle + a_3\langle\sigma_{\theta 3}(k)\sigma_{\theta 3}(k)\rangle - \frac{\lambda}{2}\sigma_{\theta 3}(7), \quad \{13\}$$

where λ is the (unknown) Lagrange multiplier. Equation {10} is the same as equation {9}. Equations {11}, {12}, and {13} are the same as equations {4}, {5}, and {6}, respectively, with the exception of the final term on the right hand side of the equations. This final term, the term which includes the Lagrange multiplier, is a residual term. Notice that this exact method allows the constraint, in this case {10}, to be satisfied exactly. All the residual error is put into the other 3 equations. As pointed out above, the least squares method distributes the error among all 4 equations, none of which are satisfied exactly. These residuals represent the extent to which σ_θ' as represented by the first three vertical dynamical modes does not match the actual σ_θ' in the region of the ocean where actual observations have been made, in this case the upper 500 m. The residual term, therefore, represents a measure of the high wave number variability above 500 m that simply cannot be represented by a sum of the first 3 vertical dynamical modes. Since σ_θ' may have high wave number variability at all levels at and above 500 m, it does not seem physically realistic to force an exact contraint at level 7 of the model as in equation {10}.

Thus, the least squares method, with 4 equations and 3 unknowns, was chosen for this study. In this least squares method, none of the equations was satisfied exactly, but the total residual, spread over all 4 equations, may be smaller than it would be using the exact method. This is also a subject worthy of much further study.

C. THE MODEL

The numerical model is a 20-level, primitive equation model of a baroclinic ocean on an f-plane, with hydrostatic, Boussinesq, and rigid lid approximations, and a flat bottom (Haney, 1985). The space-staggered B-scheme is used for horizontal finite differencing, and a sigma coordinate system defines the vertical dimension (Arakawa and Lamb, 1977). The boundary conditions at the sea surface consist of no wind stress and no buoyancy flux. The lateral boundaries of the model domain are treated as open boundaries. A sponge layer of 5 gridpoints based on the discussion of Lorenzetti and Wang (1986) is used at the lateral boundaries around the entire model domain to eliminate the effects of gravity wave noise there. The coefficients of the sponge at the gridpoints, starting from the boundary inward, are .20, .13, .07, .03, and .008, respectively. The sponge affects only the velocity fields in the model. The total depth of the ocean is 4000 meters. Model levels are listed in Table 1. The u and v components of velocity, and σ_θ are calculated at the model levels, but the w component of velocity is calculated at the midpoints between the model levels as a vertically staggered arrangement. The values of constants used in the model are listed in Table 2.

The CTZR1 cruise domain included 76 objectively analyzed gridpoints in the east-west direction by 60 gridpoints in the north-south direction. The model domain included only 64 of the gridpoints in the east-west direction by 60 gridpoints in the north-south direction, with the 12 eliminated gridpoints in the east-west direction being in the eastern part of the cruise domain along the California coast. This makes the model domain more uniform, and reduces any shallow water effects which may occur.

Since the model grid points are much closer together than the observed data points, the objectively analyzed σ_θ field was somewhat noisy on the fine 4 km model grid. Since this noise is not considered to be physical, the following horizontal smoother was used:

$$\sigma_\theta^s = \frac{1}{12}(4\sigma_{\theta 0} + \sigma_\theta^+ + \sigma_\theta^x), \qquad \{14\}$$

where $\sigma_{\theta 0} = \sigma_\theta'(i,j,k)$, the perturbation σ_θ at each domain gridpoint,

$\sigma_\theta^+ = \sigma_\theta'(i+1,j,k) + \sigma_\theta'(i-1,j,k) + \sigma_\theta'(i,j+1,k) + \sigma_\theta'(i,j-1,k)$, and

$\sigma_\theta^x = \sigma_\theta'(i+1,j+1,k) + \sigma_\theta'(i-1,j+1,k) + \sigma_\theta'(i-1,j-1,k) + \sigma_\theta'(i+1,j-1,k)$. This smoother was applied twice. Figure 3 is an example of a smoothed σ_θ field. The corresponding unsmoothed field is shown in Figure 10.

Two methods were used to diagnose the currents from a given σ_θ field. In both methods, the σ_θ field and the geostrophic currents (having zero vertical average over the full model depth) computed from the hydrostatic pressure field were used to initialize the 20 level model. The model was then integrated forward in time (for several days) until the currents and density (σ_θ) fields came into a new "balance." In one method, the density diagnostic method, the σ_θ field is held constant throughout the model run, thus

Table 1. K-LEVELS AND CORRESPONDING DEPTHS IN METERS USED IN MODEL.

k level	z(k) (meters)	k level	z(k) (meters)
1	5	11	1105
2	25	12	1325
3	65	13	1565
4	125	14	1825
5	205	15	2105
6	305	16	2405
7	425	17	2725
8	565	18	3065
9	725	19	3425
10	905	20	3805

requiring the velocity fields to adjust to it. In the second method, a robust diagnostic was added, in which the σ_θ field was allowed to adjust, but was damped back to the initial features on a time scale which was short compared to the advective time scale, but long compared to the geostrophic adjustment time scale (Sarmiento and Bryan, 1982). This was done to hold the larger scale features constant, therefore, maintaining the diagnostic feature of the model, but allowing the smaller scale features to adjust. Much of the small scale noise arises from the multi-level initialization from the objectively analyzed, sparse observations. The scaling arguments used to justify the choice of the damping time scale are presented in the results section below.

III. MODEL RESULTS AND DISCUSSION

The primitive equation model was initialized with the σ_θ fields at the levels described above, and with geostrophically balanced currents having a zero vertical average. The model was then integrated forward in time for 72 hours. In the density diagnostic version of the model, the σ_θ field was held fixed. During this integration, the currents underwent adjustments to a new state of balance in which non-linearity and eddy diffusion effects were not negligible because the currents were no longer in exact geostrophic balance. Time series of the velocity components are used to show the process by which this balance occurs. The resulting diagnostic currents are discussed below.

In addition, the robust diagnostic version of the model, as briefly described above, was integrated forward in time to 72 hours. The effects of the robust diagnostic version versus the density diagnostic version are discussed. Special attention is given to the vertical component of the velocity field and its relationship to vorticity advection for the robust diagnostic version of the model. Finally, a comparison is made between the currents as computed by the robust diagnostic version of the model and observed currents measured with an ADCP during CTZR1.

To simplify the presentation and discussion of the results, only horizontal maps and time series at 65 m depth are used, which is a model level representing surface currents in the thermocline. Discussion of change in the vertical is limited to the comparison between ADCP results and model results.

Table 2. CONSTANTS USED IN MODEL

Constant	Name	Value
Ω	earth rotation rate	$2\pi day^{-1}$
DTAU	timestep	450 s
dx	meridional grid spacing	4×10^5 cm
dy	zonal grid spacing	4×10^5 cm
D	total ocean depth	4×10^5 cm
LAT	reference latitude	38.25° N
f	Coriolis parameter	9.00×10^{-5} sec^{-1}
g	acceleration of gravity	980 cm sec^{-2}
A_M	biharmonic momentum diffusion coefficient	4×10^{17} cm^4 sec^{-1}
A_H	biharmonic heat diffusion coefficient	4×10^{17} cm^4 sec^{-1}
K_M	vertical eddy viscosity	0.5 cm^2 sec^{-1}
K_H	vertical eddy conductivity	0.5 cm^2 sec^{-1}
α	thermal expansion coefficient	2.877×10^{-4} C^{-1}

A. TIME SERIES OF VELOCITY FIELDS FOR DENSITY DIAGNOSTIC

Was a new state of balance achieved by integrating the density diagnostic version of the model ahead 72 hours? Time series of the u, v, and w-components of velocity at (i,j) gridpoint (44,25) (i.e. map coordinate point (172,96) in Figure 11) and at a depth of 65 meters (90 meters for w because of the vertically staggered grid described in Chapter II) show the adjustments in the velocity at these locations (Figures 12 and 13). Note the large oscillations which occur during the early integration times in the model. These

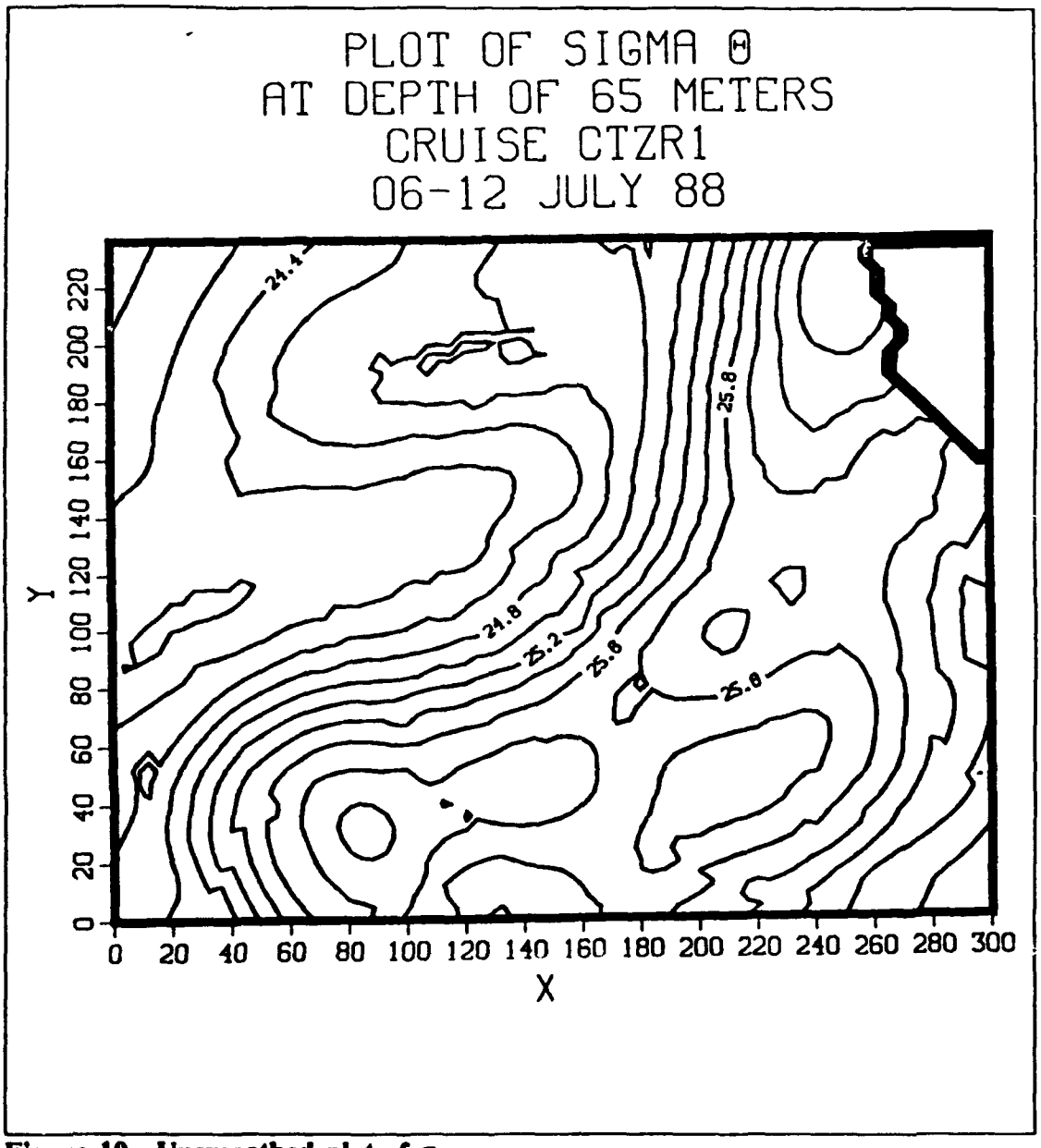

Figure 10. Unsmoothed plot of σ_θ.

oscillations are damped as the new state of balance is approached at around 48 hours. The small oscillations continue to occur at 72 hours, especially in the u and v component velocities (Figure 13). The oscillations are remnants of the initial adjustments in the velocities, and could possibly continue for several more days.

This process can also be seen in the time series of the u, v, and w-components of velocity at (i,j) gridpoint (41,24), or (x,y) map coordinate point (160,92) in Figure 11, also at a depth of 65 meters (90 meters for w)(Figures 14 and 15). At this point, the damped oscillations beyond 48 hours in the u and v velocity components are almost sinusoidal.

Examination of the time series of the component velocities at these two points show that an exact balance has not been reached in the density diagnostic version of the model at 72 hours. Small oscillations are still ocurring, although it appears that the currents are quite close to their final equilibrium values at 72 hours. The similar evolution of the velocity components with time at the two points indicates that the entire velocity field probably evolves in a similar way. Integrating the model beyond 72 hours to determine when the oscillations in the velocity components are fully damped was deemed unnecessary.

B. SIGMA-θ AND VELOCITY FIELDS FOR DENSITY DIAGNOSTIC

The σ_θ field at time 0 for a depth of 65 meters is shown in Figure 16, and the resulting hydrostsatic pressure field in Figure 11. By definition, these fields do not change with time in the density diagnostic model.

The initial (geostrophic) u and v components of the velocity field at 65 meters are shown in Figures 17 and 18. The resulting vector velocity field is shown in Figure 19. Note the strong south to southwestward jet flowing from the northeastern corner to the southwestern corner of the model domain. Velocities in this jet reach as high as 80

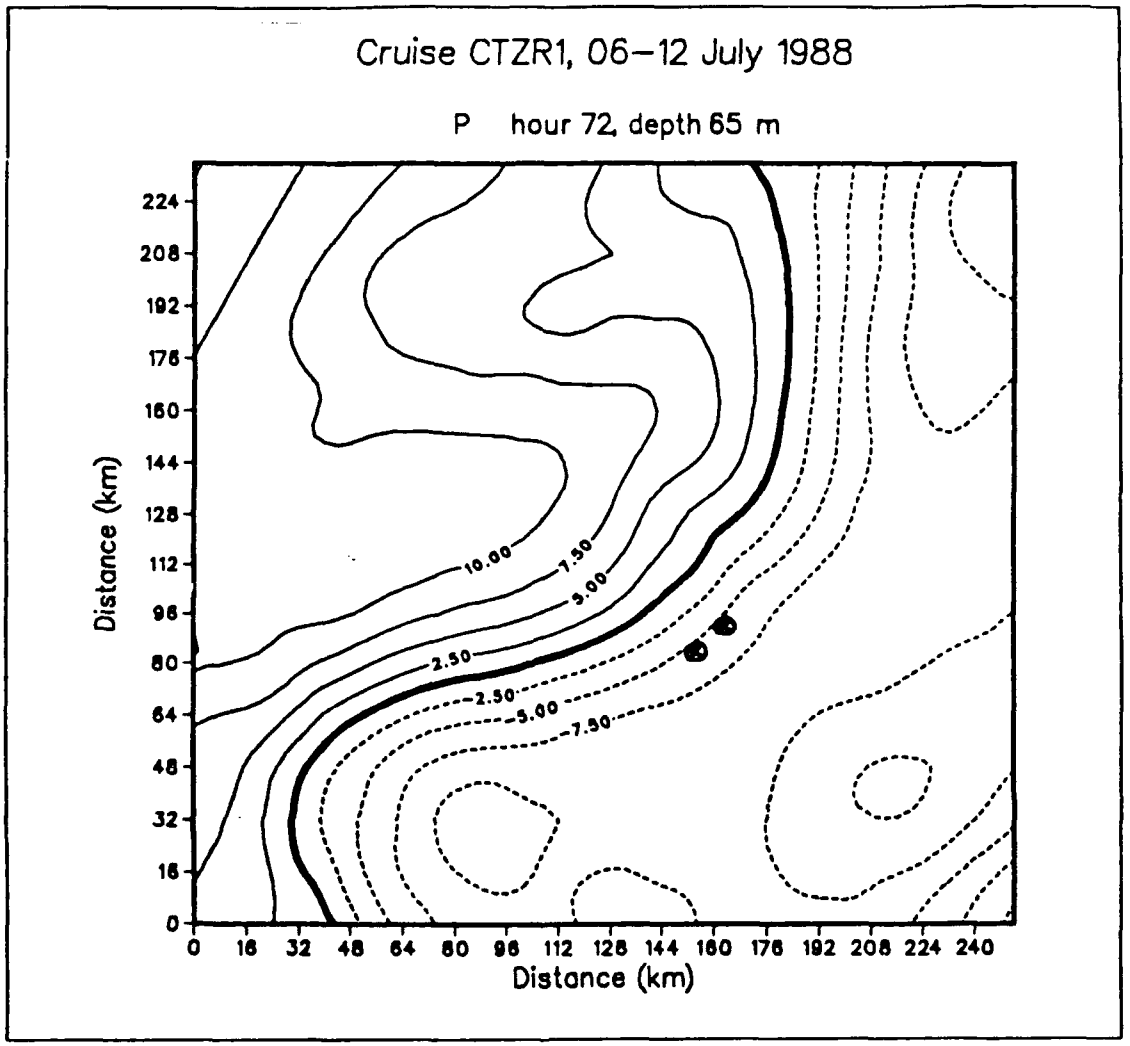

Figure 11. Pressure Field of the Density Diagnostic at 65 Meters and 72 Hours: Points referred to are marked. Contour interval 2.5 cm. Dashed lines are negative values.

cm/sec. Velocities as high as 75 cm/sec were observed at 50 meters by Huyer et al. (1990) during CTZR1. The velocities shown in the model domain at time 0 are simply the geostrophic velocities with which the model is initialized. The initial w velocity component is zero by definition.

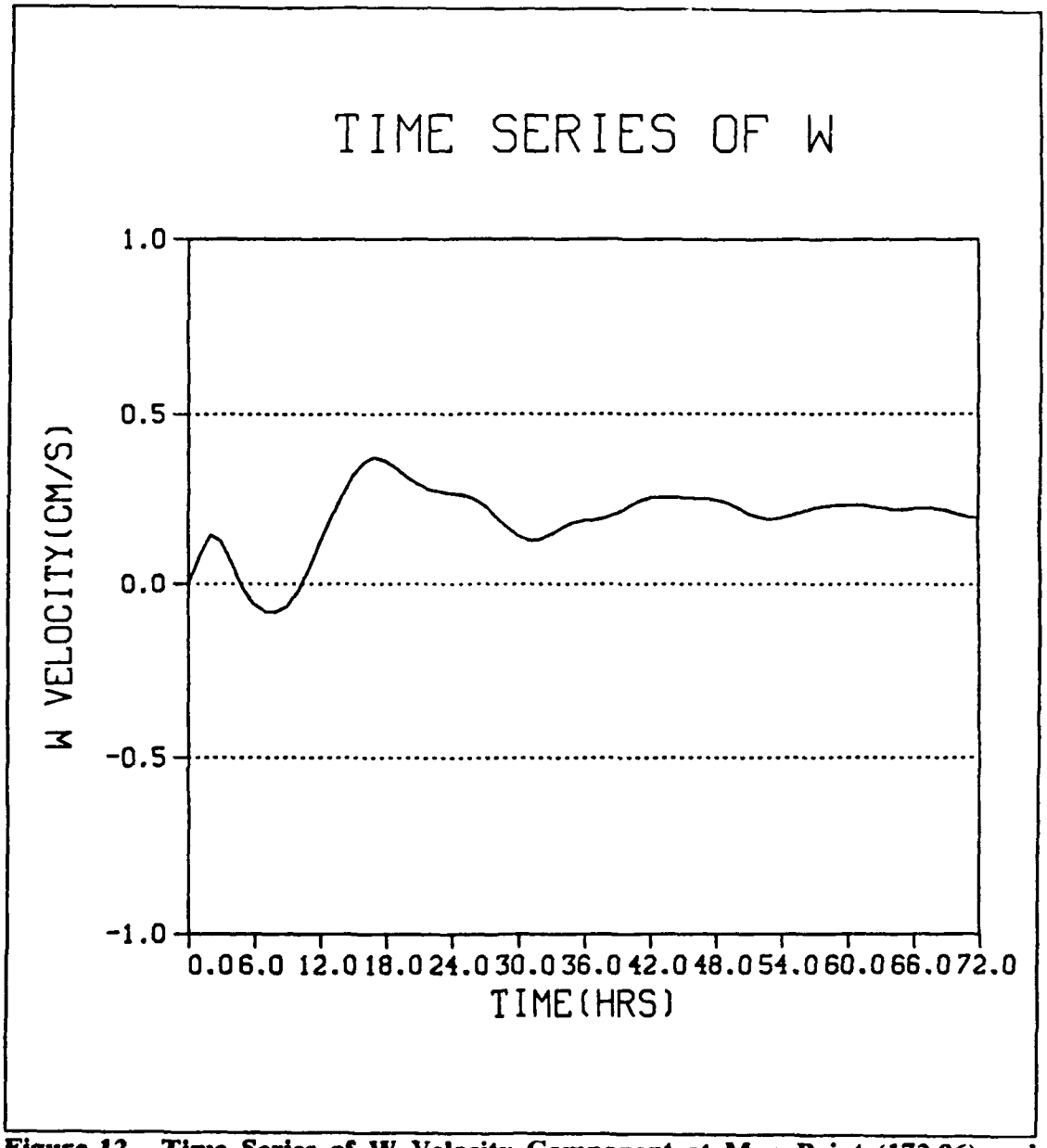

Figure 12. Time Series of W Velocity Component at Map Point (172,96) and Depth of 90 Meters for Density Diagnostic.

After integrating the model ahead 72 hours, the velocities are no longer geostrophic. The u component velocity field has intensified, especially in the south central part of the model domain where the jet turns westward(Figure 20). The v component velocity field

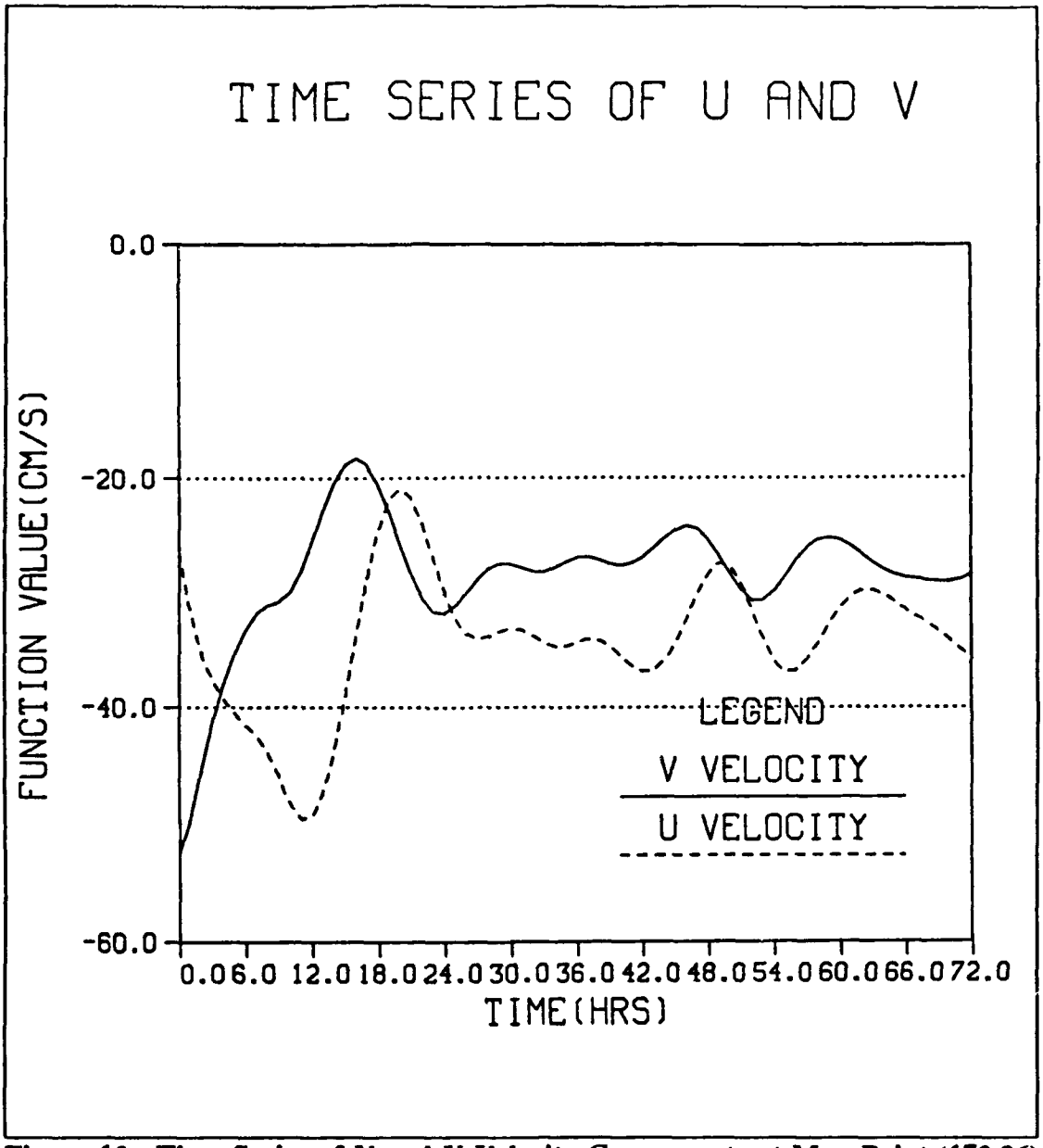

Figure 13. Time Series of U and V Velocity Components at Map Point (172,96) and Depth of 65 Meters for Density Diagnostic.

has also adjusted(Figure 21). This intensification and adjustment can also be seen in the time series shown in Figure 13. Note the increased u velocity shown at 72 hours as compared to 0 hours. Also note how the v velocity has changed.

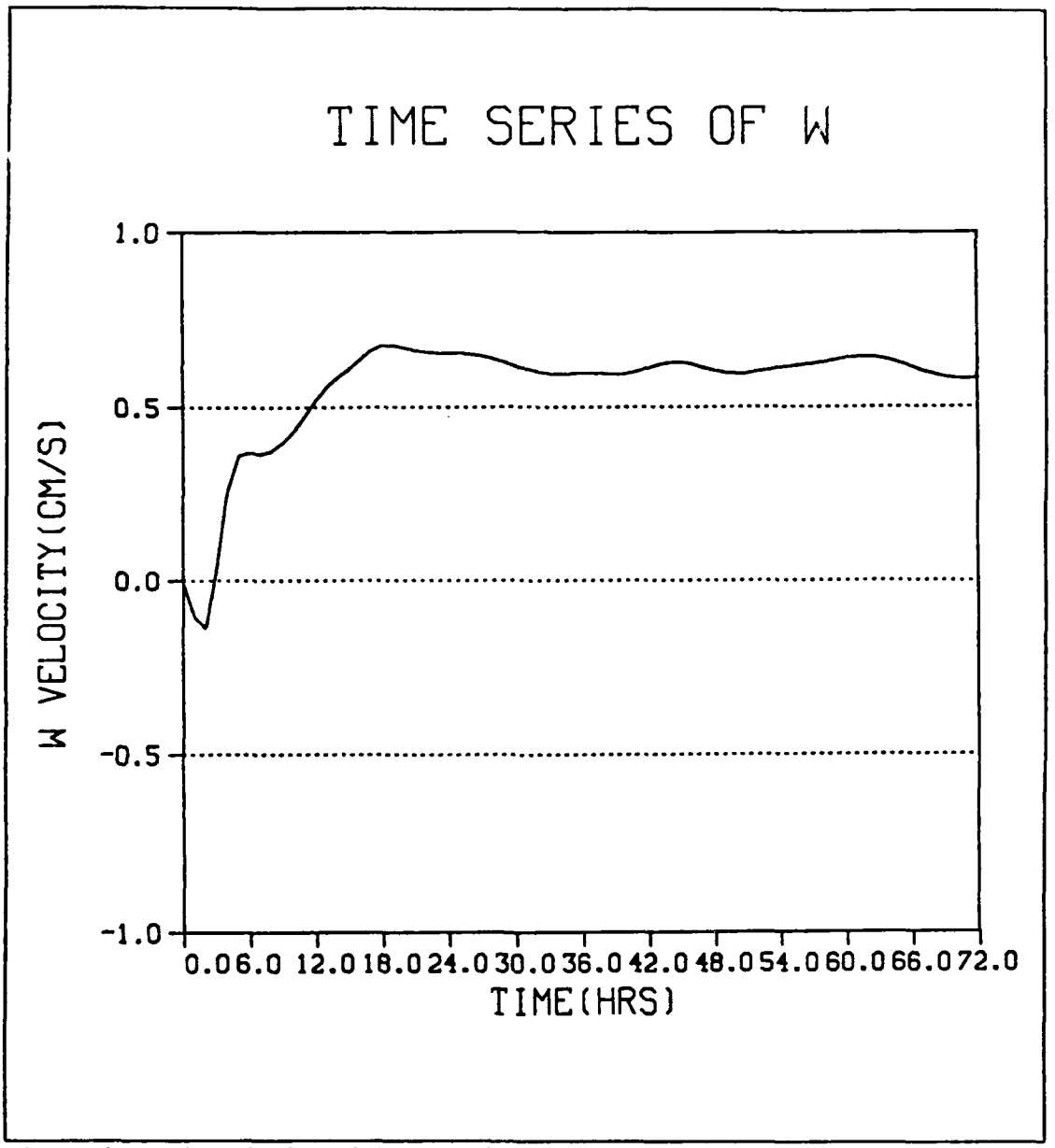

Figure 14. Time Series of W Velocity Component at Map Point (160,92) and Depth of 90 Meters for Density Diagnostic.

The resultant horizontal velocity vectors for 72 hours are shown in Figure 22. A comparison of a few of the vectors shown here with the corresponding initial geostrophic velocities in Figure 19 reveals significant direction shifts as well as speed changes. The

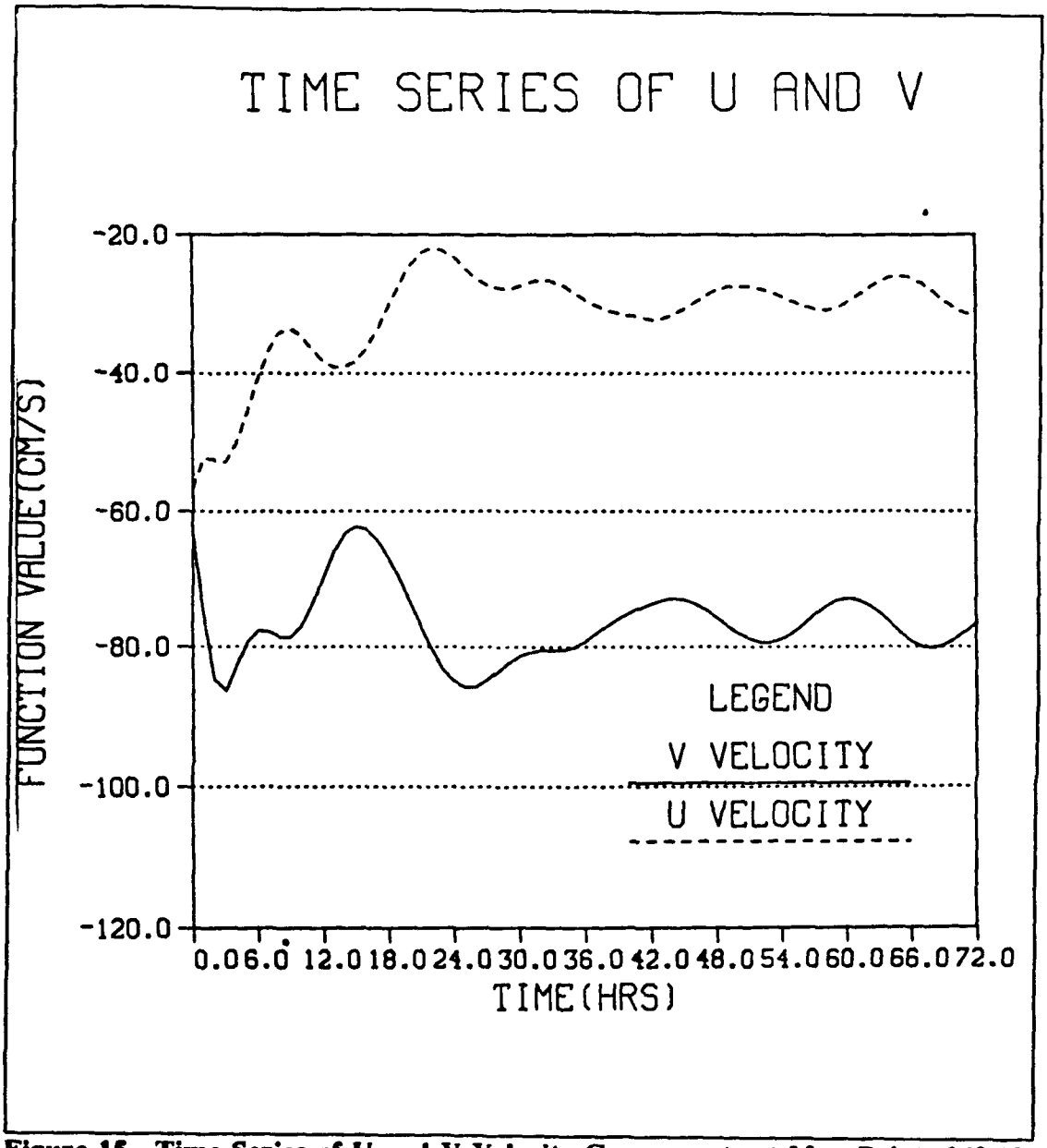

Figure 15. Time Series of U and V Velocity Components at Map Point (160,92) and Depth of 65 Meters for Density Diagnostic.

direction shift varies from point to point as illustrated by the time series in Figures 13 and 15. From the u and v components of velocity in Figure 13, it can be inferred that the current has shifted westward by 72 hours. The direction of the current at the point in

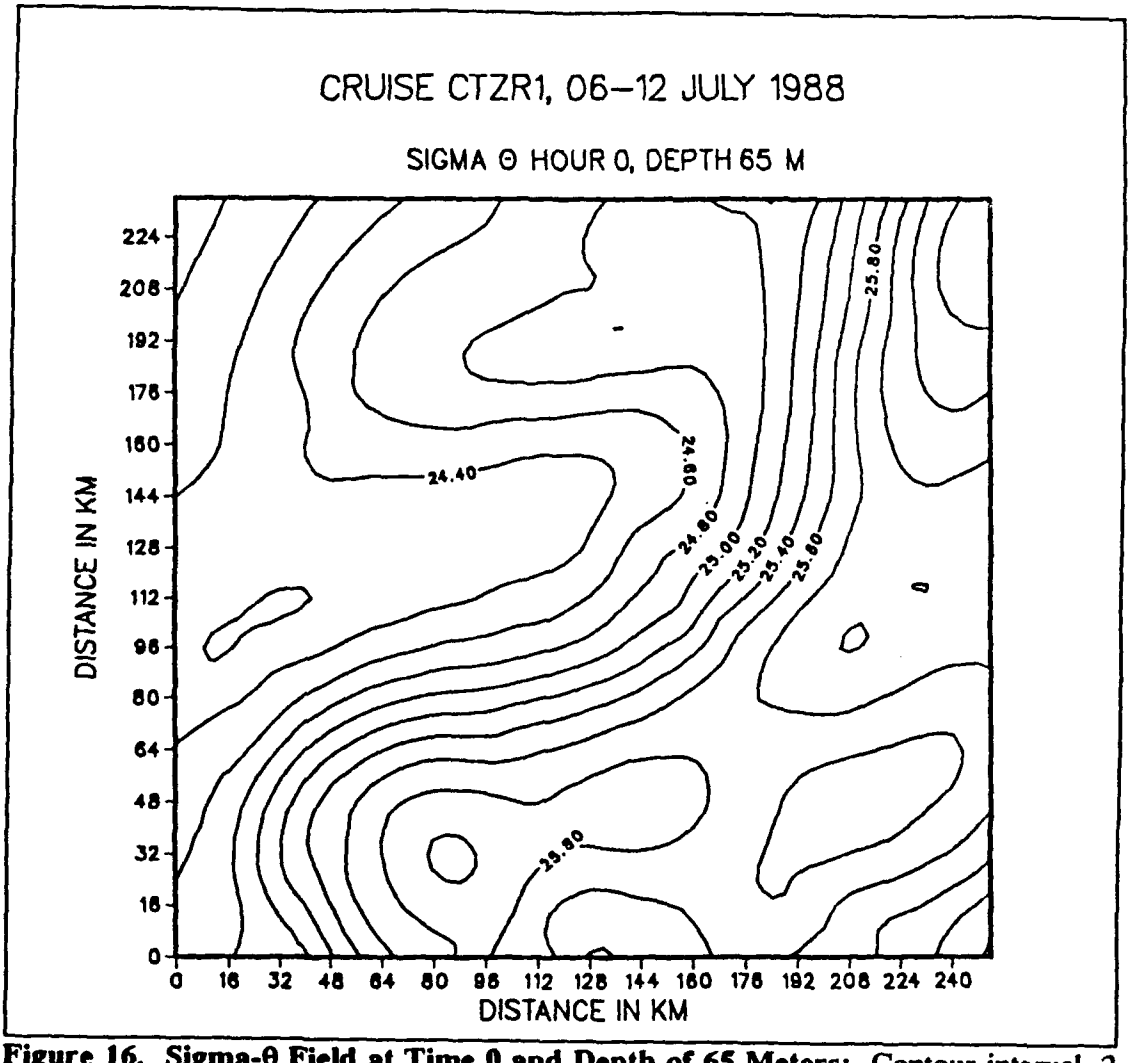

Figure 16. Sigma-θ Field at Time 0 and Depth of 65 Meters: Contour interval .2 kg/m^3

Figure 15 seems to have shifted to the east.

The maximum velocities shown in the jet at 72 hours are over 100 cm/sec. This is higher than the maximum observed values noted above.

The w component of velocity at 72 hours and 90 meters is shown in Figure 23. Maximum upwelling is around .8 cm/sec, and maximum downwelling is around 1.0 cm/sec. At the points shown in the above time series, upwelling is occurring (Figures 12

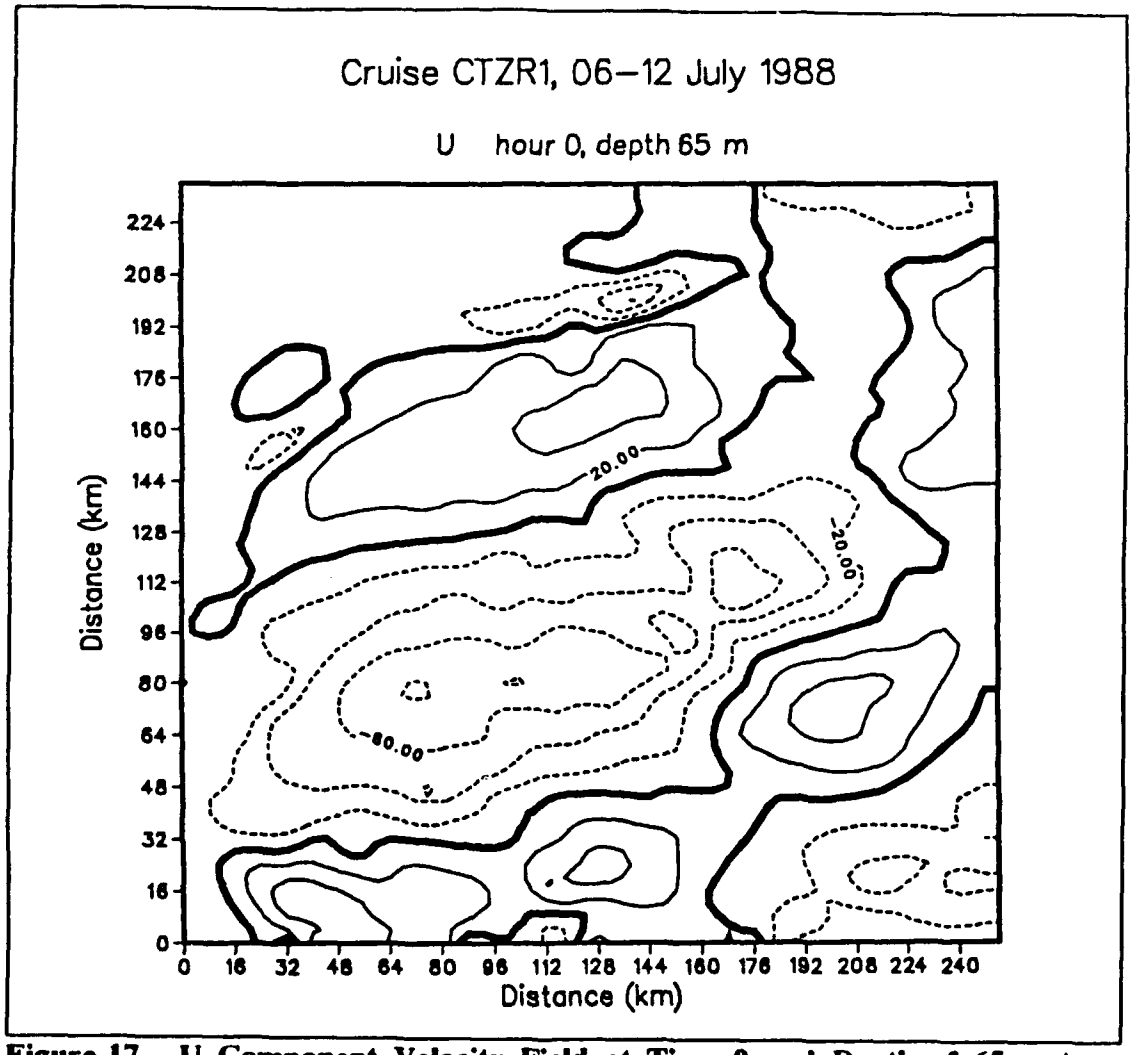

Figure 17. U Component Velocity Field at Time 0 and Depth of 65 meters: Contour interval 20 cm/s. Dashed lines are negative values.

and 14). At map point (172,96) upwelling velocity is around .25 cm/sec (Figure 12), and at map point (160,92) upwelling velocity is around .6 cm/sec (Figure 14), at 72 hours. These velocities convert to 200 to 700 meters per day which are much higher than the 6 to 25 meters per day observed by Washburn et al. (1990) and Kadko et al. (1990) in the CTZ region.

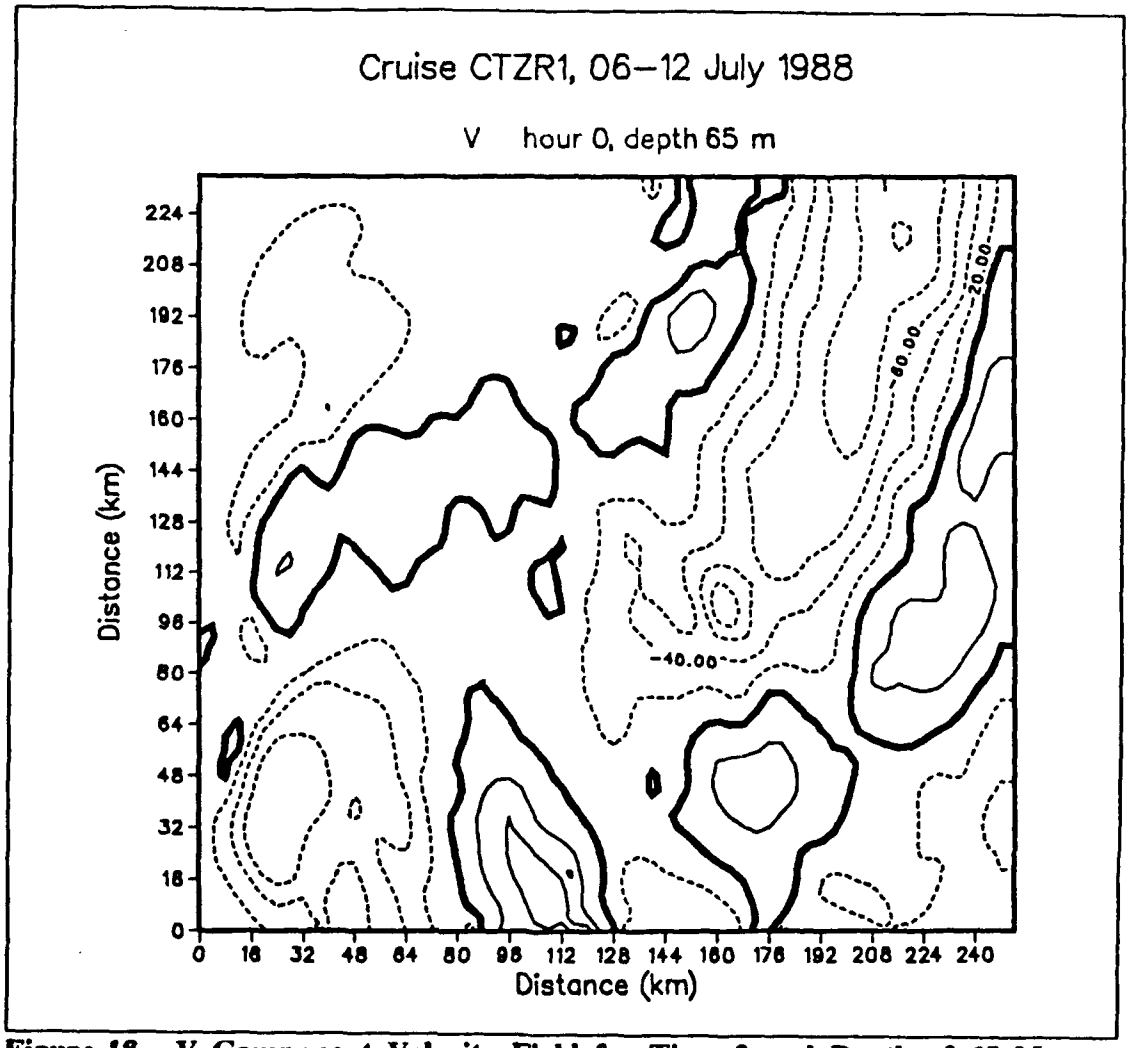

Figure 18. V Component Velocity Field for Time 0 and Depth of 65 Meters: Contour interval 20 cm/s. Dashed lines are negative values.

Therefore, the density diagnostic version of the model does not give horizontal or vertical velocities which agree closely with those observed. One possible reason for the rather poor results for the density diagnostic method is that the currents must adjust entirely to the given density field. However, in the real ocean there is a continual mutual adjustment between the currents and the density. Futhermore, on scales of motion that are smaller than the internal Rossby radius (about 30 km in the CTZ region) the density

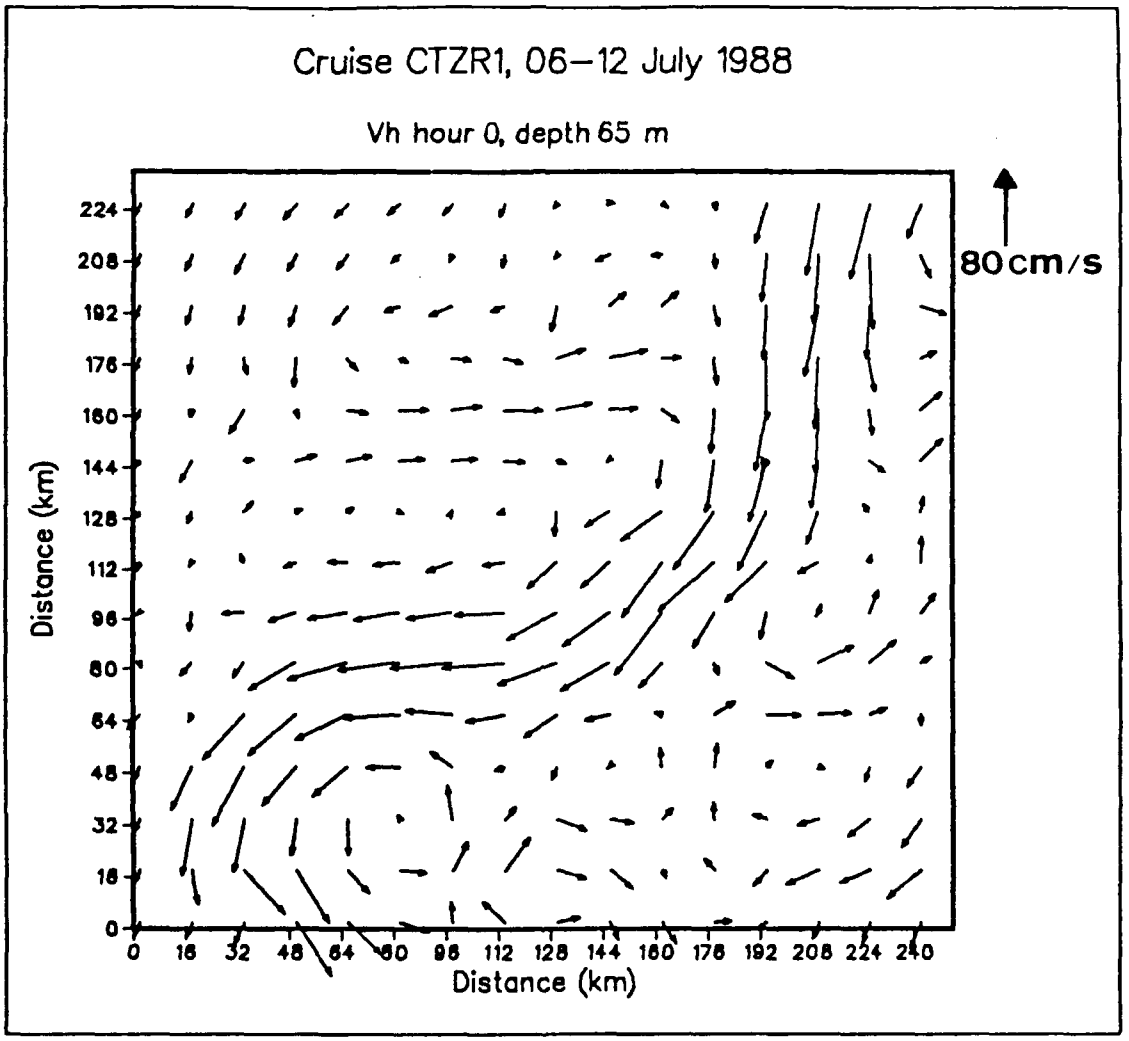

Figure 19. Resultant Horizontal Velocity Vectors at Time 0 and Depth of 65 Meters: Vectors are plotted at every 4th gridpoint.

field would actually adjust to the currents. Thus, the density diagnostic method is not really valid for scales of motion of the order of, or smaller than, about 30 km. In order to facilitate a mutual geostrophic adjustment between the currents and the density field, the robust diagnostic method is introduced in the next section.

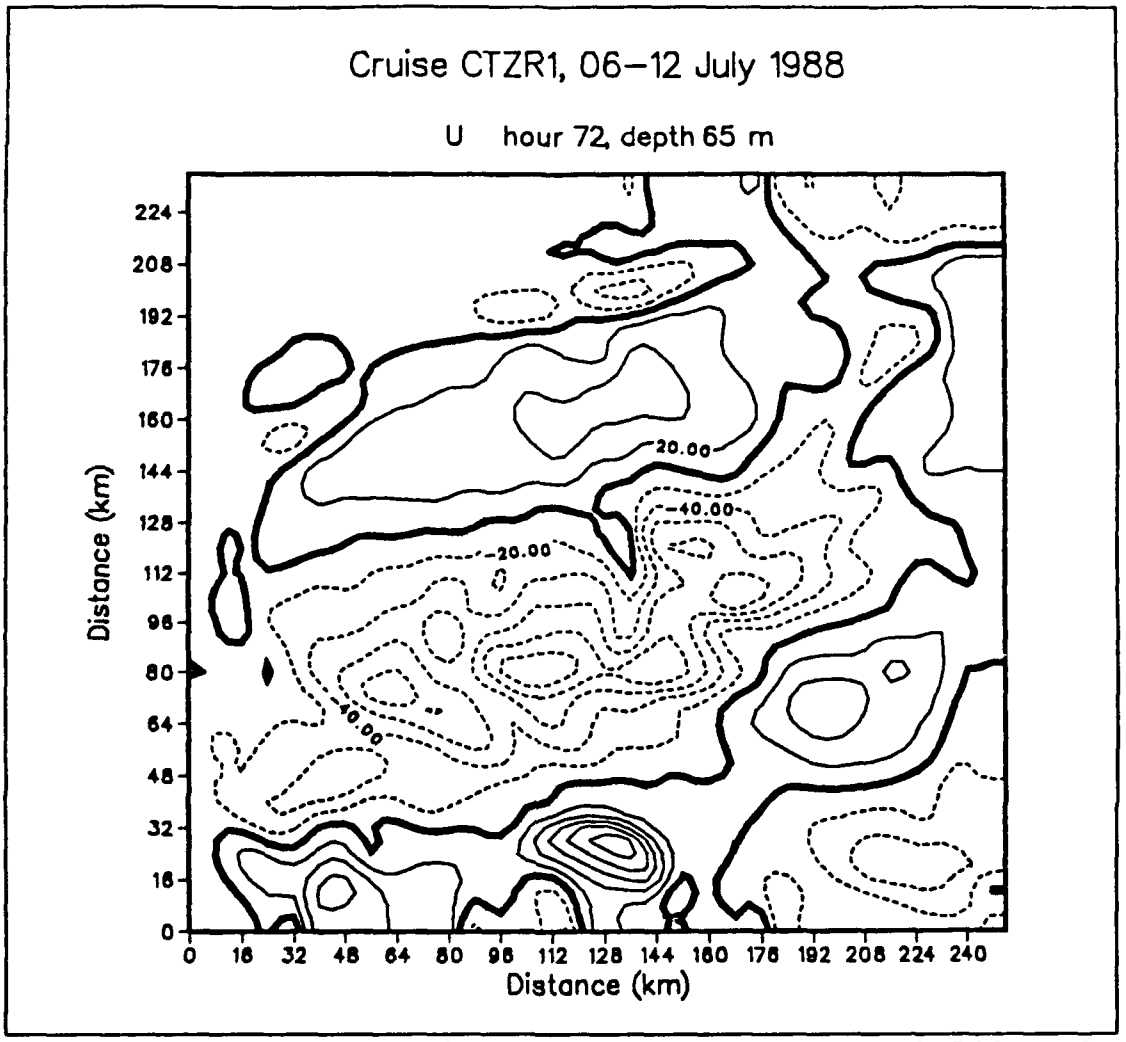

Figure 20. U Component Velocity at Time 72 Hours and Depth of 65 Meters for Density Diagnostic: Contour interval 20 cm/s. Dashed lines are negative values.

C. THE ROBUST DIAGNOSTIC AND ITS EFFECTS

The robust diagnostic method, as described in Chapter II, allows the currents and the σ_θ field to mutually adjust to each other. The σ_θ field is damped back to its initial value on a time scale that is fast compared to advection but slow compared to the time needed for geostrophic adjustment. As stated above, this type of damping allows the smaller scale features that have short time scales to mutually adjust, but it holds the larger

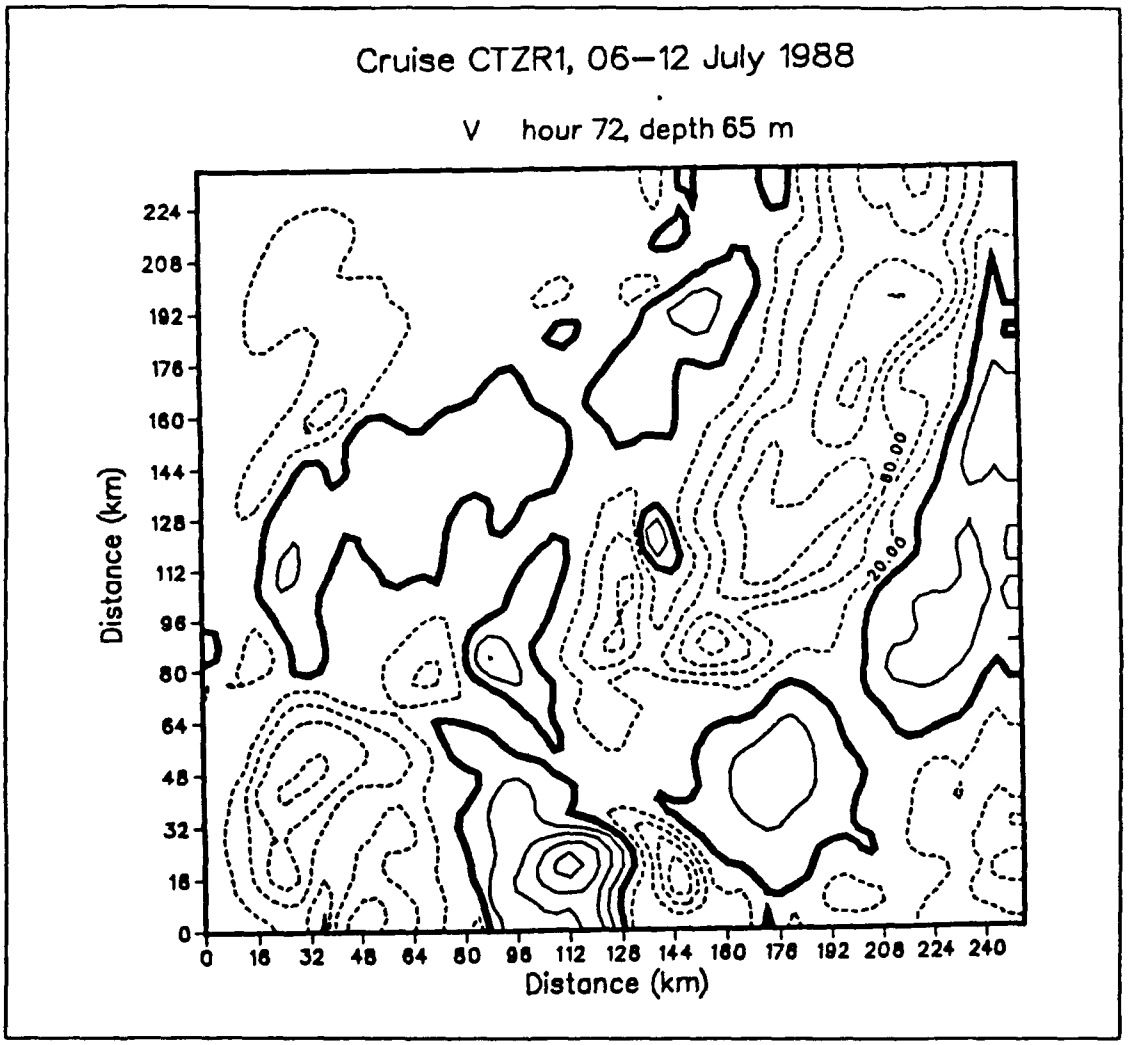

Figure 21. V Component Velocity at Time 72 Hours and Depth of 65 Meters for Density Diagnostic: Contour interval 20 cm/s. Dashed lines are negative values.

scale features, that might otherwise advect through a sizeable part of the domain in 3 days, constant.

The advective time scale is:

$$t_a \approx \frac{L}{U} \tag{15}$$

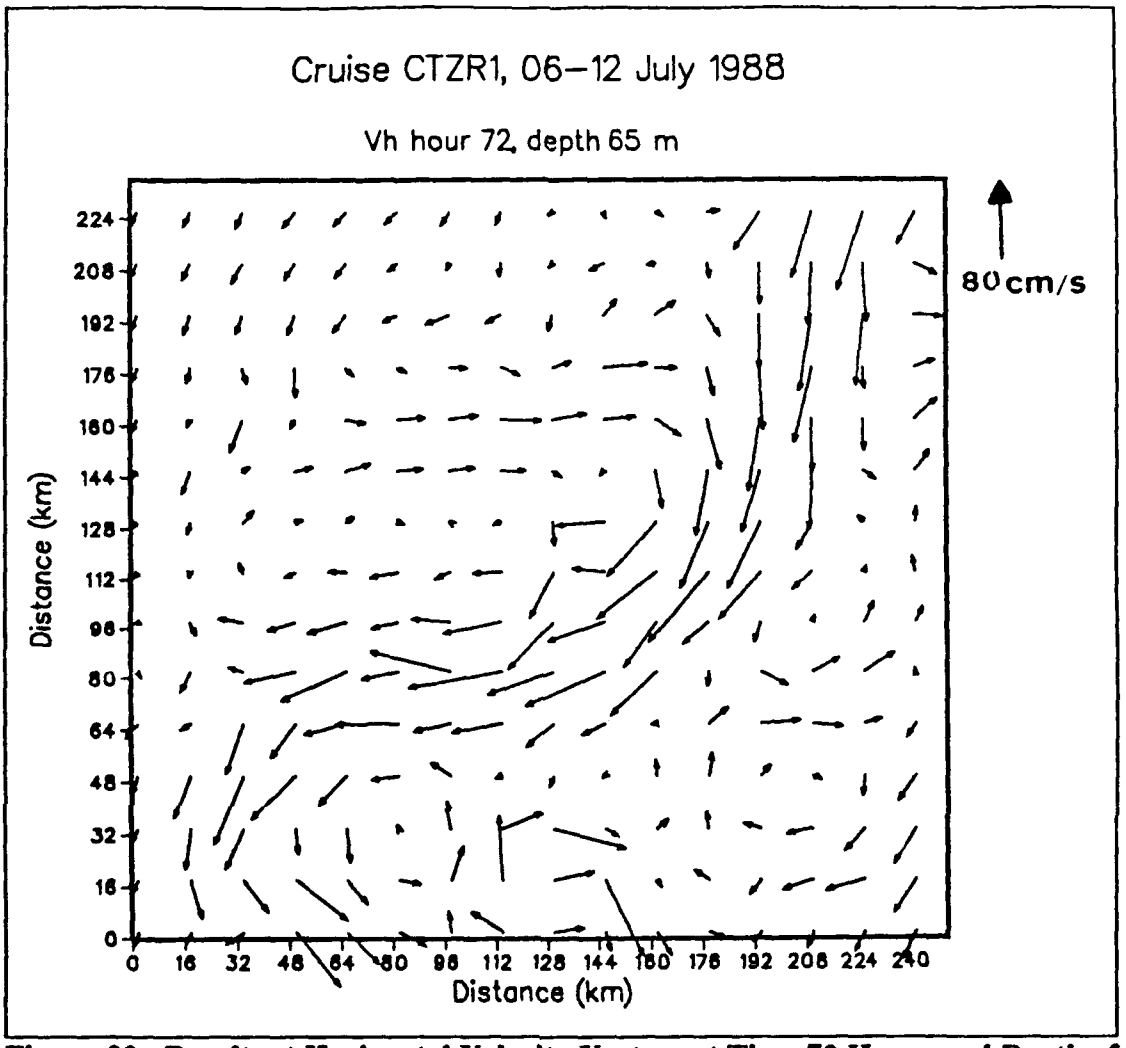

Figure 22. Resultant Horizontal Velocity Vectors at Time 72 Hours and Depth of 65 Meters for Density Diagnostic: Vectors are plotted at every 4th gridpoint.

where L and U are the length scale and the velocity scale, respectively. In this case, L was chosen as 50 km and U was chosen as 50 cm/s which yields a t_a of approximately 10^5 seconds or 1 day.

The geostrophic adjustment time scale is:

$$t_f = f^{-1} \tag{16}$$

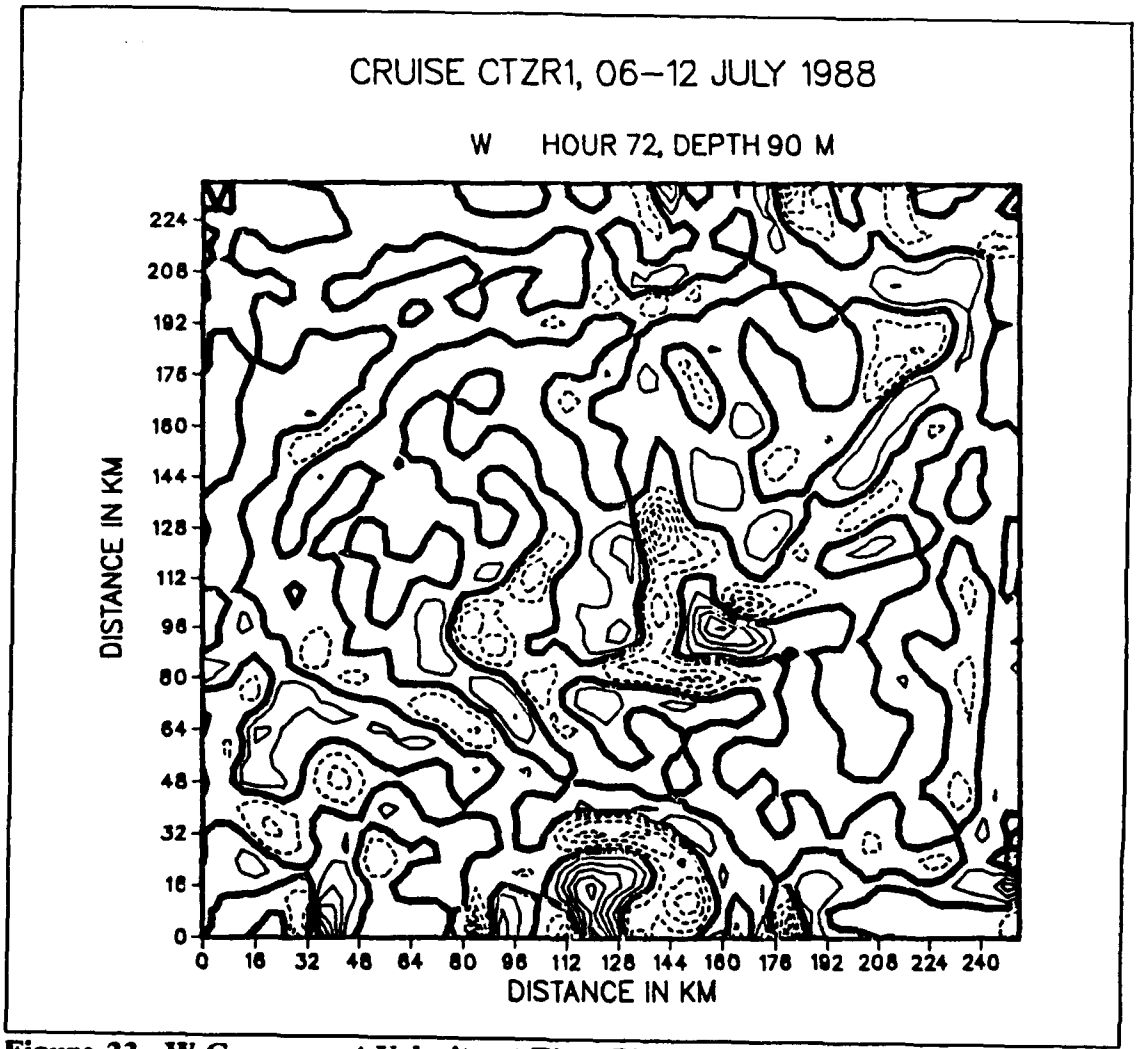

Figure 23. W Component Velocity at Time 72 Hours and Depth of 90 Meters for Density Diagnostic: Contour interval .2 cm/s. Dashed lines are negative values.

where f is the coriolis parameter. For this case, t_f is approximately 10^4 seconds or 1/10 of a day.

The damping time scale, therefore, should be much longer than 1/10 of a day and much shorter than 1 day to produce the desired effect. Clearly, it is not possible to satisfy both of these constraints. For this study, 1 day (t_s) was chosen as the damping

time scale to maximize the time over which geostrophic adjustment can occur. Since the damping time is the same as the advective time, and not smaller, some advective effects will be unavoidable.

Time series of σ_θ, and the u, v, and w components of velocity are used to illustrate the adjustment process with the robust diagnostic (Figures 24, 25, 26, 27, 28, and 29). The time series of σ_θ for map points (172,96) and (160,92) and a depth of 65 meters shown in Figures 24 and 27 indicate a downward trend with time of σ_θ occurring at both points for the robust diagnostic method.

The time series of the component velocities show an initial adjustment as in the density diagnostic case followed by a series of long oscillations (Figures 25, 26, 28, and 29). These long oscillations seem to begin at about 30 hours for the u and v component velocities, and somewhat later for the w velocity component. The oscillation is particularly flat for the v velocity component at map point (160,92). The long oscillations at both points are probably caused by advective effects at the longer integration times, due to using 1 day (t_a) as the damping time scale. In other words, the longer scale synoptic features are not being held perfectly constant. At the model grid point shown, there is sinking motion ($w < 0$ in Figure 25) on the longer time scale. The resulting vertical advection of the mean stratification causes the density (σ_θ) to decrease with time at 65 m (Figure 24). The model is losing its strictly diagnostic character. This trade-off is, however, desirable in terms of other features of the robust diagnostic as discussed below.

Comparisons between the u and v velocity component time series for the density diagnostic (Figures 13 and 15) and those of the robust diagnostic (Figures 26 and 29)

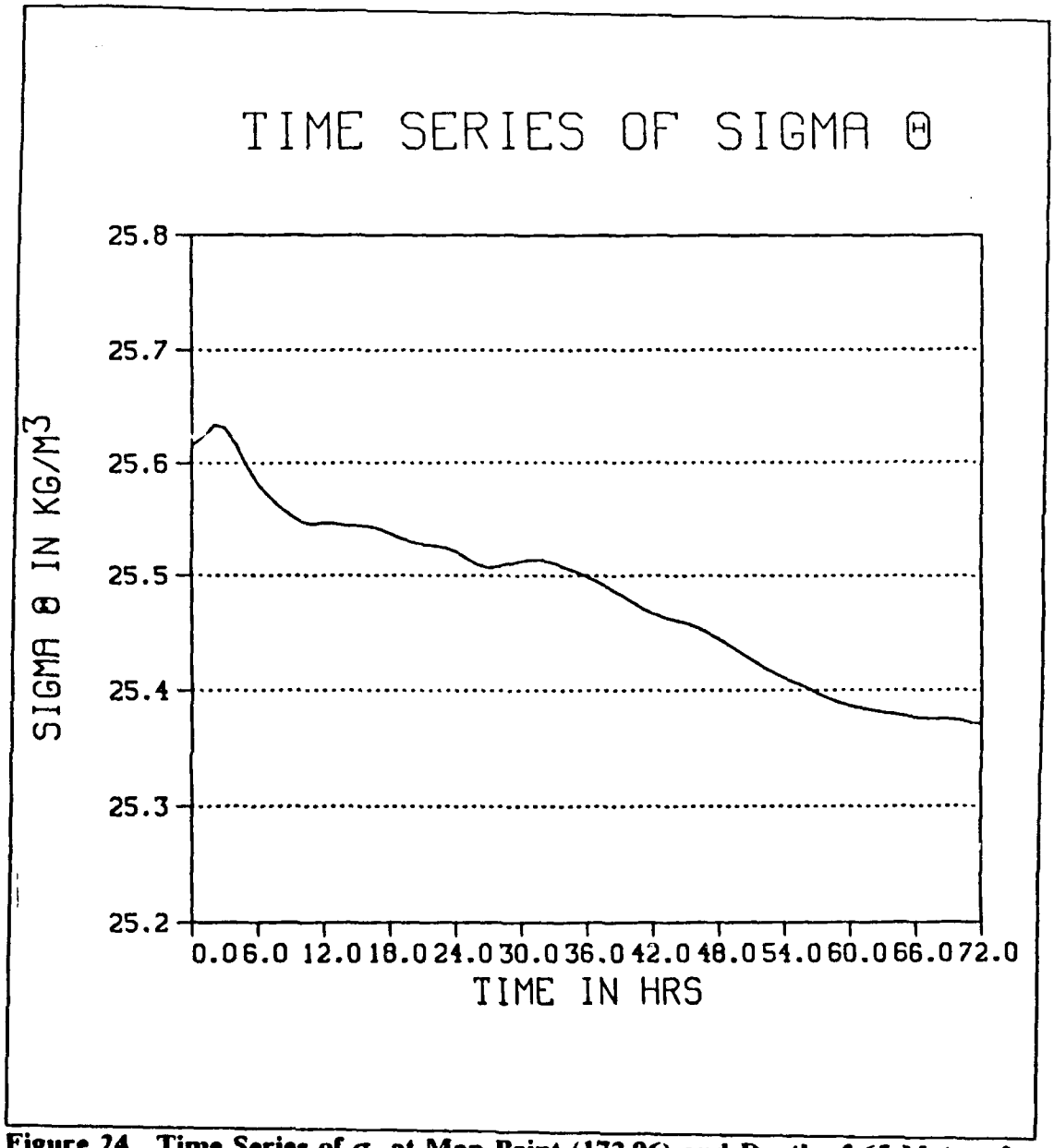

Figure 24. Time Series of σ_θ at Map Point (172,96) and Depth of 65 Meters for Robust Diagnostic.

indicate that the adjustment in horizontal velocity occurs faster for the robust diagnostic case. The short oscillations which are characteristic of the density diagnostic method are not present in the robust diagnostic case. Whereas the density diagnostic has not

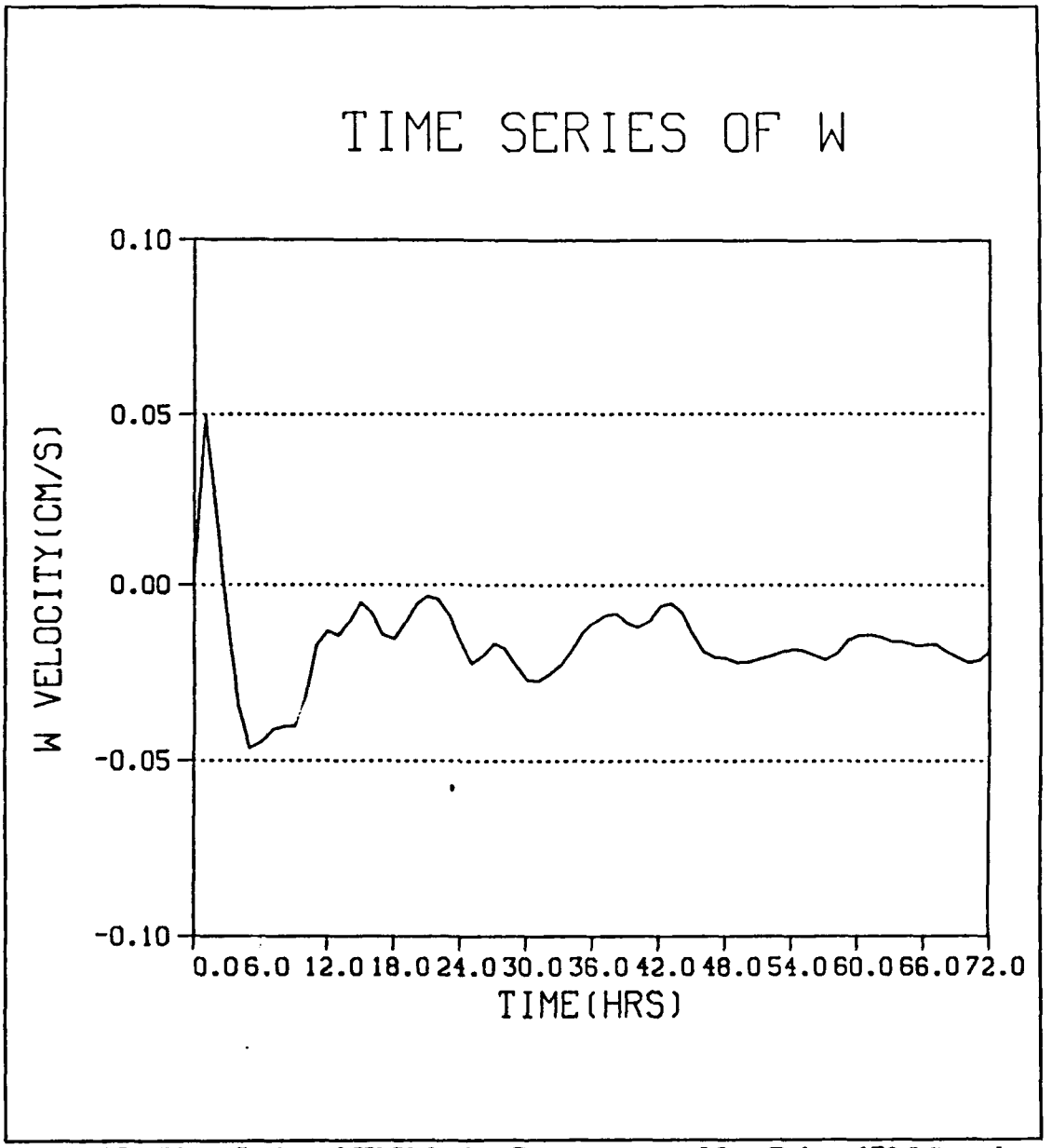

Figure 25. Time Series of W Velocity Component at Map Point (172,96) and Depth of 90 Meters for Robust Diagnostic.

completely adjusted by 72 hours, the robust diagnostic has, discounting the long wave oscillations which are believed to be advective rather than an initial adjustment.

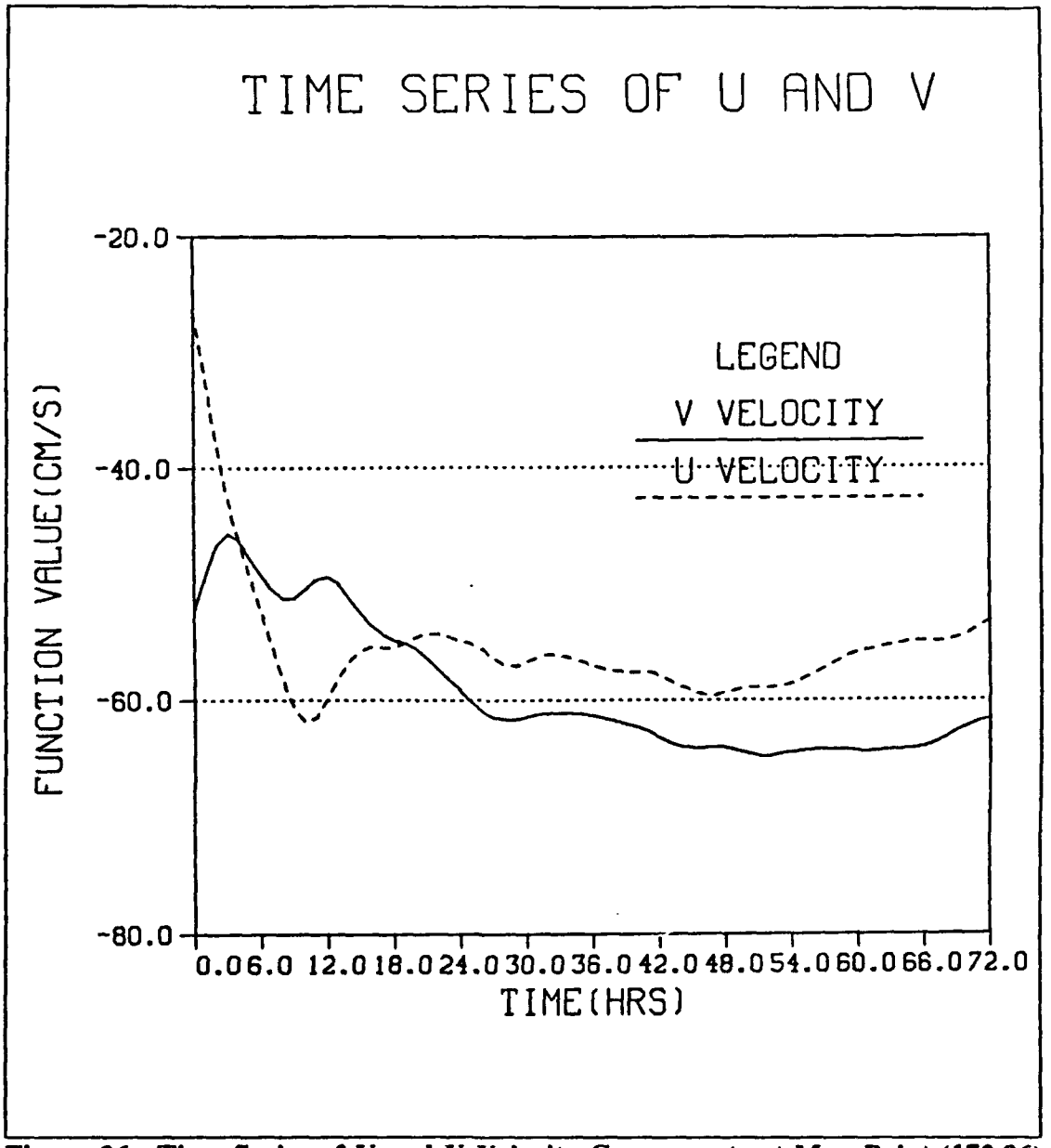

Figure 26. Time Series of U and V Velocity Components at Map Point (172,96) and Depth of 65 Meters for Robust Diagnostic.

Comparisons between the density diagnostic and robust diagnostic time series of the w component velocity may be misleading (Figures 12, 14, 25, and 28). The robust diagnostic w component velocity time series seem to be oscillating much more than their

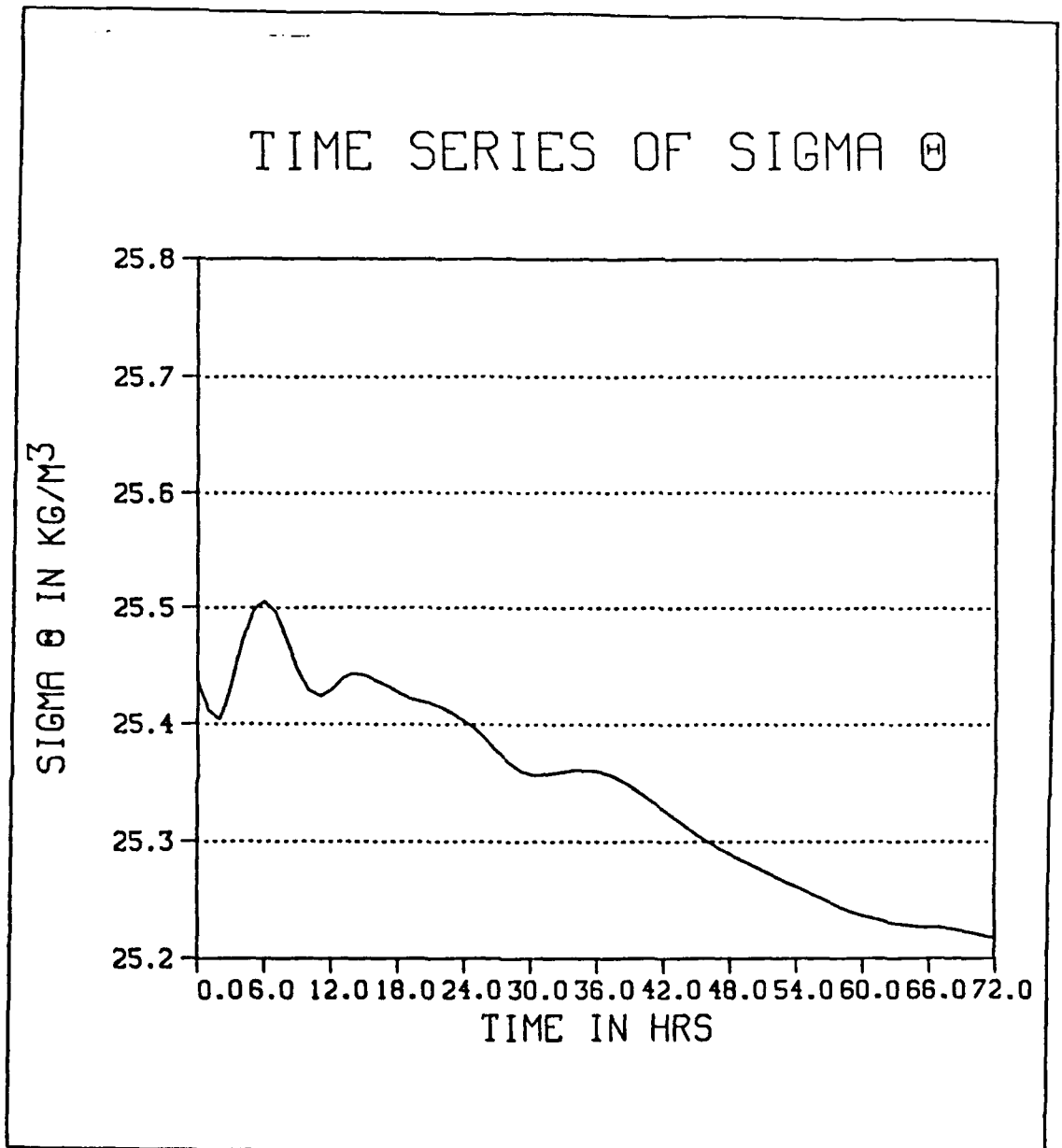

Figure 27. Time Series of σ_θ at Map Point (160,92) and Depth of 65 Meters for Robust Diagnostic.

density diagnostic counterparts. The robust diagnostic w component velocities are, however, an order of magnitude smaller than those of the density diagnostic. Therefore, what may seem like larger oscillations are not. The order of magnitude difference

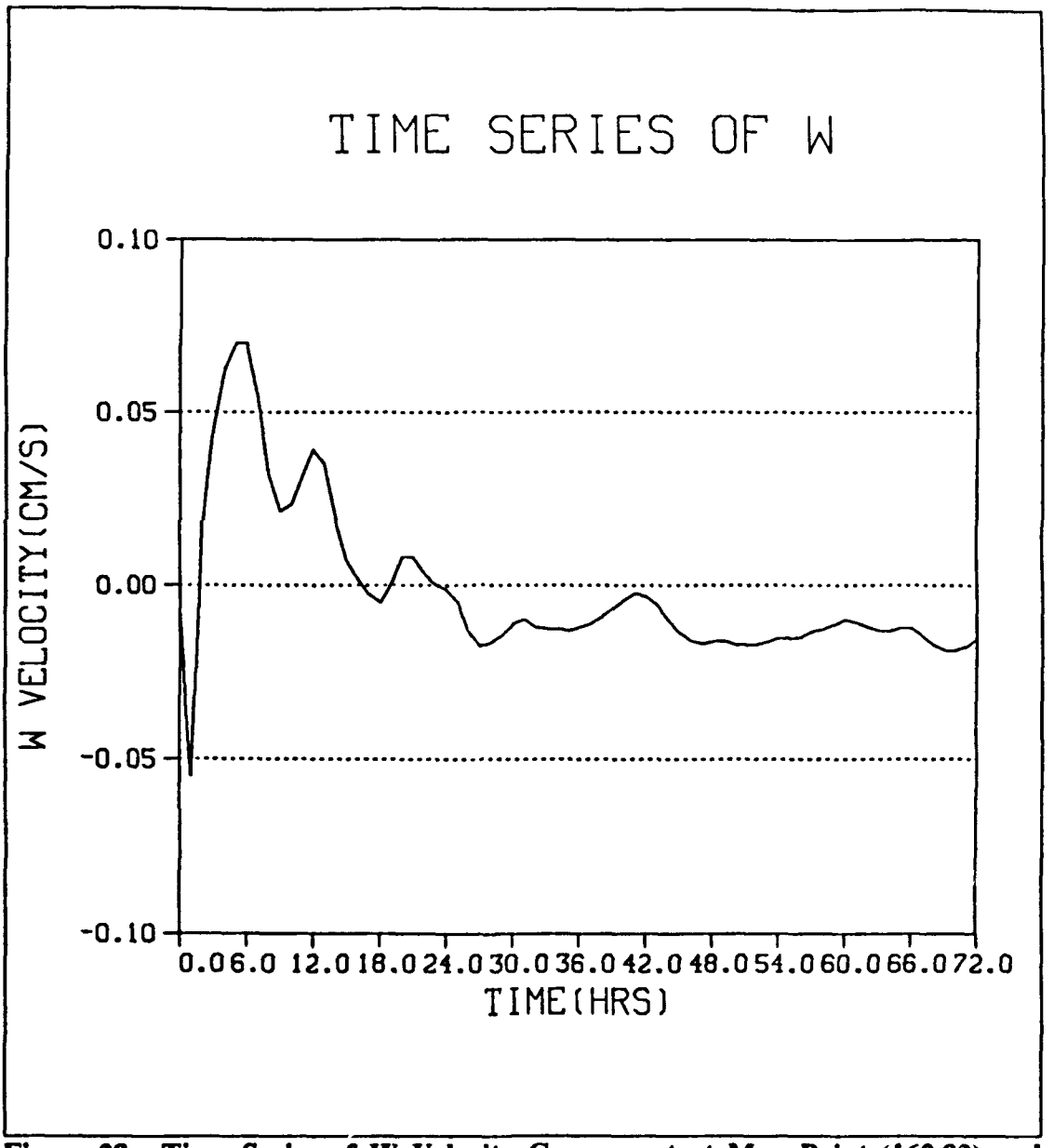

Figure 28. Time Series of W Velocity Component at Map Point (160,92) and Depth of 90 Meters for Robust Diagnostic

between the robust diagnostic and the density diagnostic w component velocities is discussed further below.

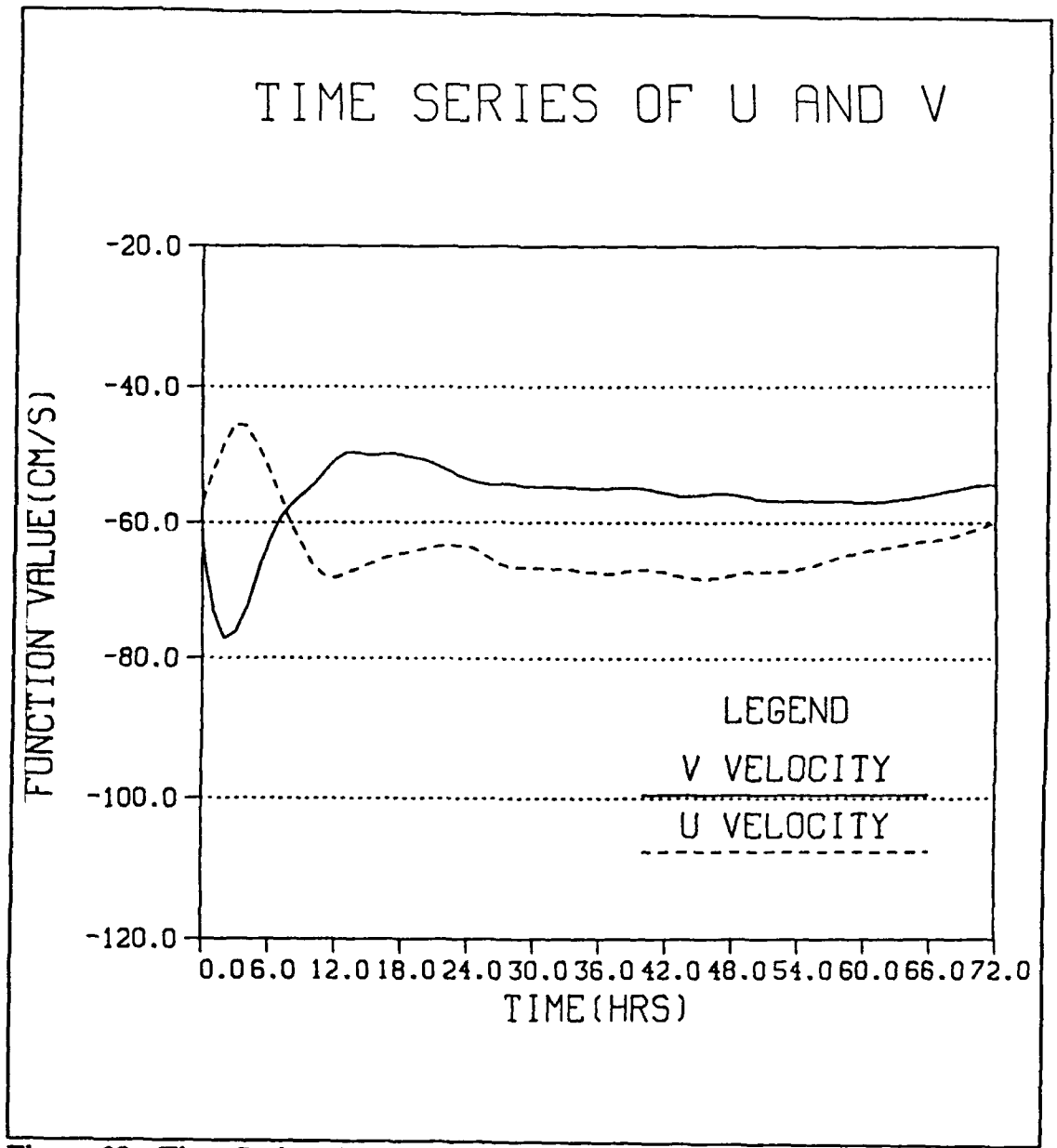

Figure 29. Time Series of U and V Velocity Components at Map Point (160,92) and Depth of 65 Meters for Robust Diagnostic.

The σ_θ field is allowed to change over time in the robust diagnostic. The time series in Figures 24 and 27 show this change for two points in the model domain. The initial σ_θ field at 65 meters depth for the robust diagnostic case is the same as that for the

density diagnostic (Figure 16). The corresponding field at 72 hours is shown in Figure 30. The decrease in σ_θ with time shown at the two points in the time series (Figures 24 and 26) is not uniform throughout the model domain. In general, areas of downwelling coincide with areas where σ_θ decreases between 0 and 72 hours, and areas of upwelling coincide with areas where σ_θ increases between 0 and 72 hours (Figures 31 and 35). Downwelling brings warmer, less dense water to the 65 meter level and upwelling carries colder, denser water to that level.

In addition to the larger scale changes in σ_θ due to vertical advection, there has also been a tendency for adjustment on the smaller space scales to produce a smoother σ_θ field at 72 hours. Some of the smoothing effect is accomplished by the biharmonic eddy diffusion and some by means of the dynamic adjustment. A scale analysis of the thermodynamic equation in the model indicates that the parameter r,

$$r = \frac{A}{f}\left(\frac{2\pi}{L}\right)^4, \qquad \{17\}$$

where A = biharmonic diffusion coefficient, gives the ratio of the two effects (i.e. the ratio of the biharmonic diffusion term to the change of σ_θ on the time scale of adjustment (f^{-1})). Using the value of A from Table 2, we find that r = 5 for L (wavelength) = 10 km, while r = .3 for L = 20 km and r = .06 for L = 30 km. Thus, the smoothing effect is primarily accomplished by the dynamic adjustment for disturbance wavelengths equal to or greater than about 20 km. Biharmonic eddy diffusion dominates for wavelengths of 10 km or smaller.

The initial u and v component velocity fields, and the resultant velocity vectors at 65 meters depth for the robust diagnostic, are the same as those for the density diagnostic (Figures 17, 18 and 19). The corresponding fields at 72 hours are shown in Figures 32, 33, and 34. Comparisons between the u and v velocity component fields at 72 hours for the density diagnostic and the robust diagnostic show that the robust diagnostic fields are smoother (Figures 20, 21, 32 and 33). The smoothness of the u and v component velocity fields for the robust diagnostic at 72 hours is consistent with the relative smoothness of the σ_θ field for the robust diagnostic at 72 hours as compared to the initial σ_θ field. If the noise in the 72 hour u and v component velocity fields in the density diagnostic case is caused by the effects of small scale noise present in the initial objectively analyzed fields, the robust diagnostic adjustment eliminates these effects. Also, note that the strongest u and v component velocities at 72 hours for the density diagnostic are considerably stronger than those for the robust diagnostic (Figures 20, 21, 32, and 33). The resultant vector fields at 65 meters depth shown in Figures 22 and 34 reflect this difference. The density diagnostic vector field has a maximum velocity over 100 cm/s (Figure 22). The robust diagnostic vector field, on the other hand, has a maximum velocity of around 75 cm/s, which is closer to the maximum velocities stated above observed by Huyer et al. (1990) at 50 meters depth during CTZR1 (Figure 34).

Comparing the w component velocity field for the robust diagnostic solution at 72 hours (the initial w is zero by definition for the robust diagnostic as well as the density diagnostic) with the corresponding field from the density diagnostic solution shows a dramatic difference. As noted in connection with Figure 28, the maximum upwelling and

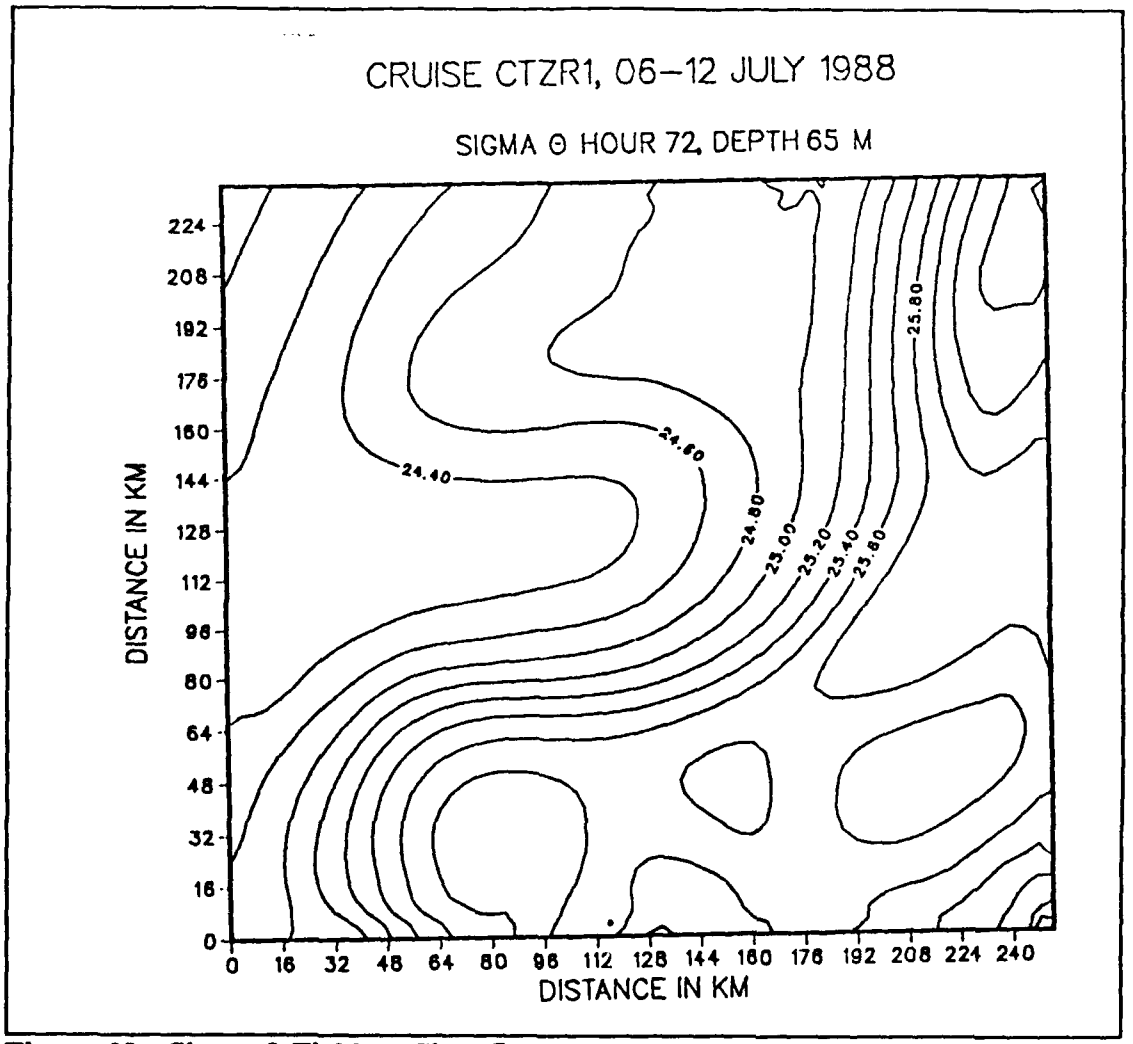

Figure 30. Sigma-θ Field at Time 72 Hours and Depth of 65 Meters for Robust Diagnostic: Contour interval .2 kg/m^3.

downwelling velocities for the robust diagnostic are an order of magnitude smaller than those for the density diagnostic (Figures 23 and 35). For the robust diagnostic, the time series of w component velocity at the two points (Figures 25 and 28) indicate that downwelling is occurring at both points at 72 hours at the rate of approximately .02 cm/s (17 m/d). For the density diagnostic, on the other hand, the time series of the w component velocity (Figures 12 and 14) indicate that upwelling is occuring at both points

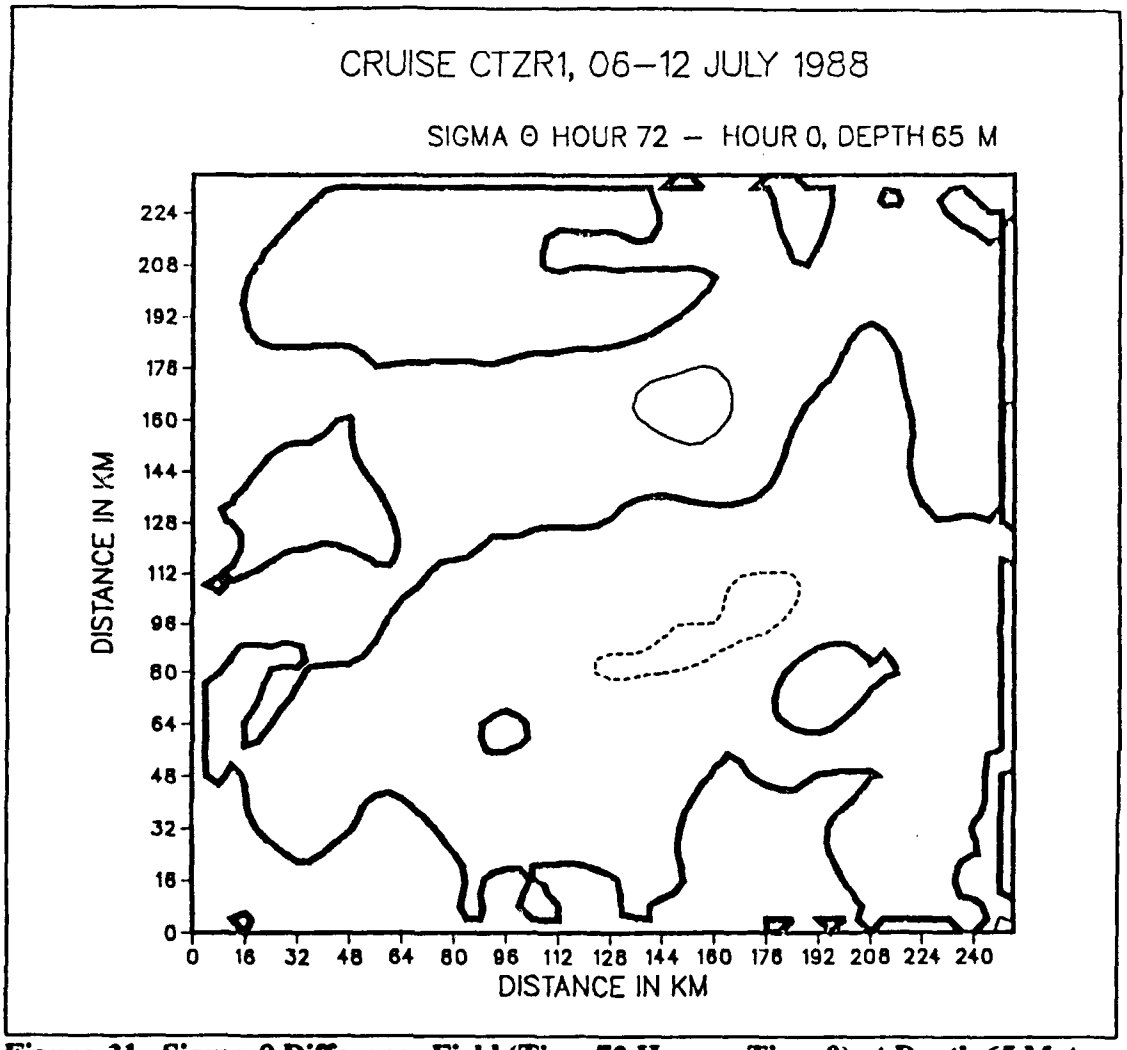

Figure 31. Sigma-θ Difference Field (Time 72 Hours - Time 0) at Depth 65 Meters for Robust Diagnostic: Contour interval .2 kg/m^3. Dashed lines are negative values.

at 72 hours at the rate of 200 to 700 m/d.

As indicated above, these vertical velocities for the density diagnostic were much higher than the values observed by Washburn et al. (1990) and Kadko et al. (1990). The robust diagnostic vertical velocities as represented by the time series at the two points and the w field at 90 meters depth at 72 hours (Figures 25, 28, and 35), on the other hand,

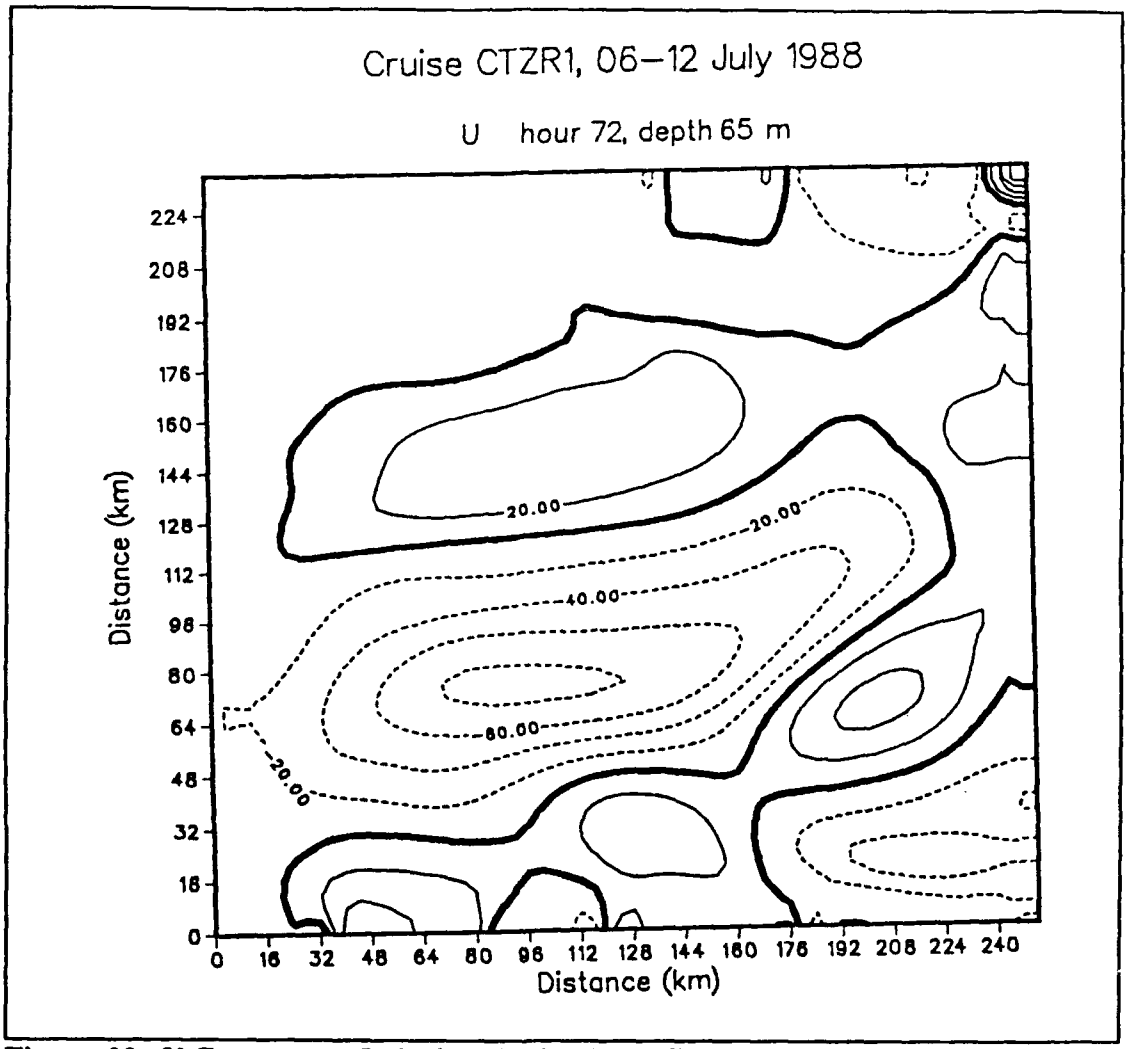

Figure 32. U Component Velocity Field at Time 72 Hours and Depth of 65 Meters for Robust Diagnostic: Contour interval 20 cm/s. Dashed lines are negative values.

are of the order of 20 meters per day, which are similar to the above stated observed values of 6 to 25 meters per day.

The advantages of the robust diagnostic as compared to the density diagnostic are now clear. The robust diagnostic solution comes to a new balance much faster than does the density diagnostic solution. In addition, at this new state of balance the robust

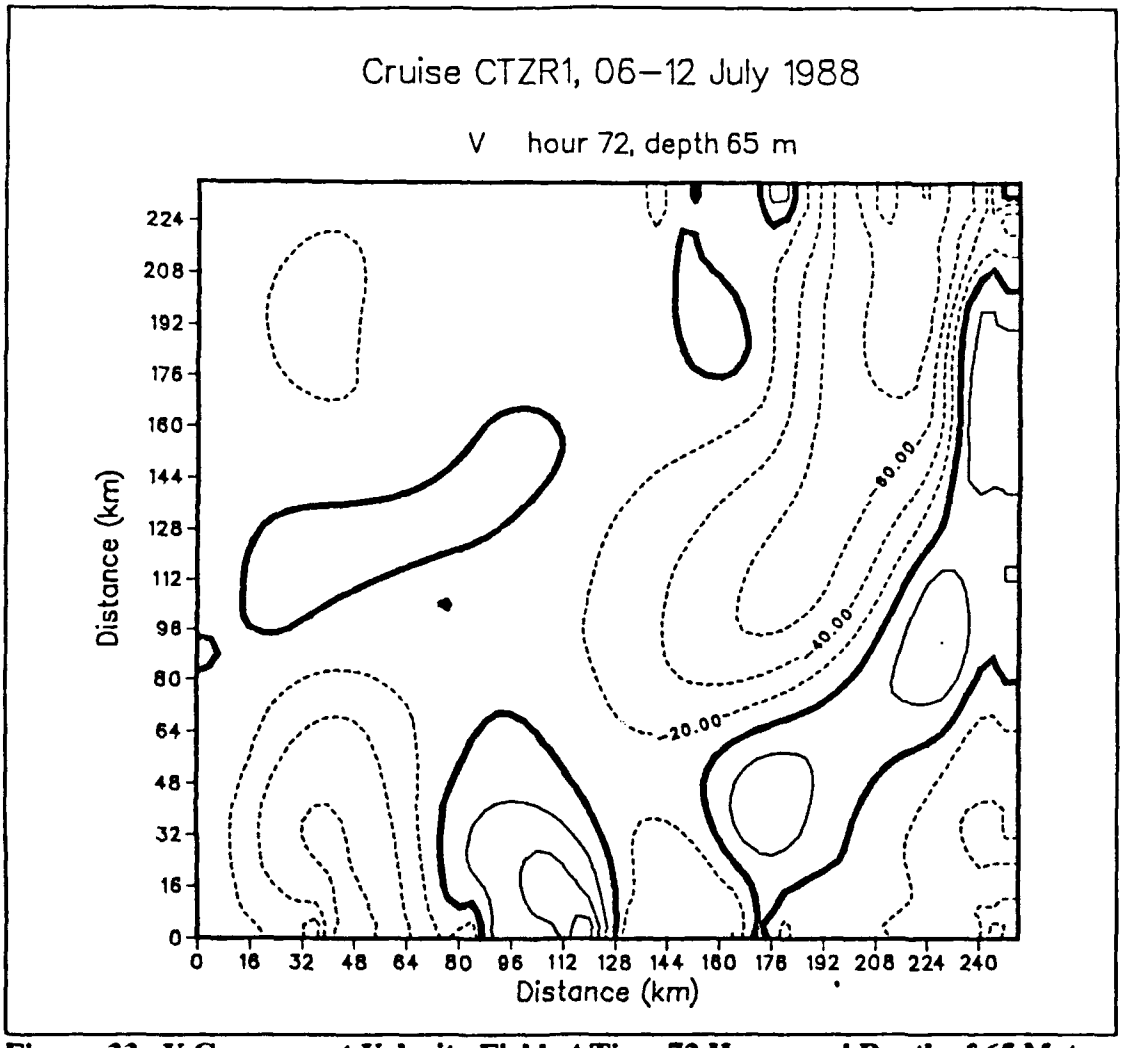

Figure 33. V Component Velocity Field at Time 72 Hours and Depth of 65 Meters for Robust Diagnostic: Contour interval 20 cm/s. Dashed lines are negative values.

diagnostic velocity fields, horizontal and vertical, are much closer to the observed values than the density diagnostic fields. For this reason, the balance of the discussion focuses on the robust diagnostic version of the model.

Two minor drawbacks of the robust diagnostic require further investigation. The first, as mentioned above, is the long oscillations which occur at the longer integration

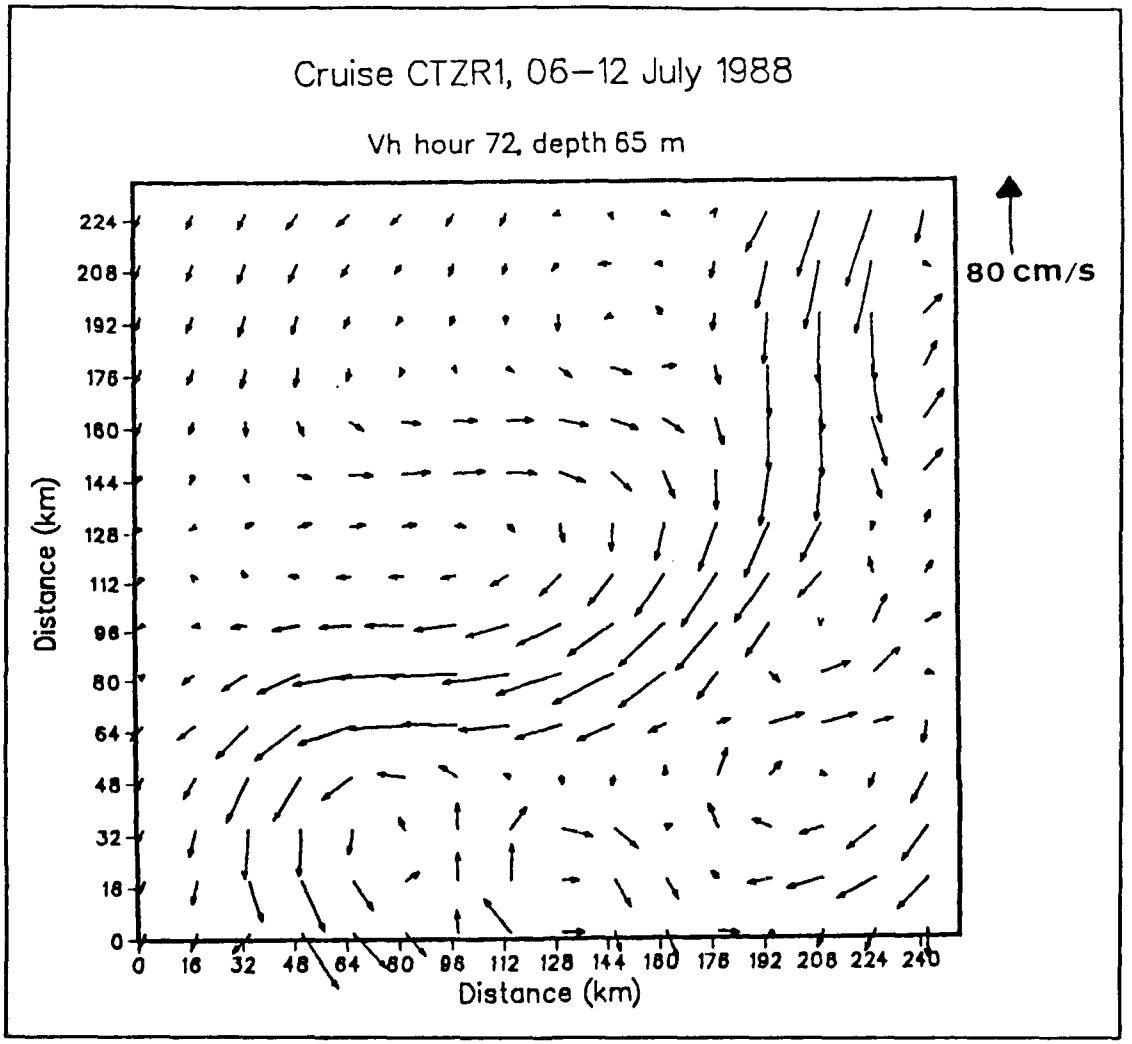

Figure 34. Resultant Horizontal Velocity Vectors at Time 72 Hours and Depth of 65 Meters for Robust Diagnostic: Vectors are plotted at every 4th gridpoint.

times of the model. These oscillations could be damped by shortening the damping time scale; thus, reducing the likelihood of the long wave synoptic features adjusting with time. This shortening of the damping time scale could, however, reduce some of the desirable geostrophic adjustment. Sensitivity studies, therefore, are needed to determine the optimum damping time scale.

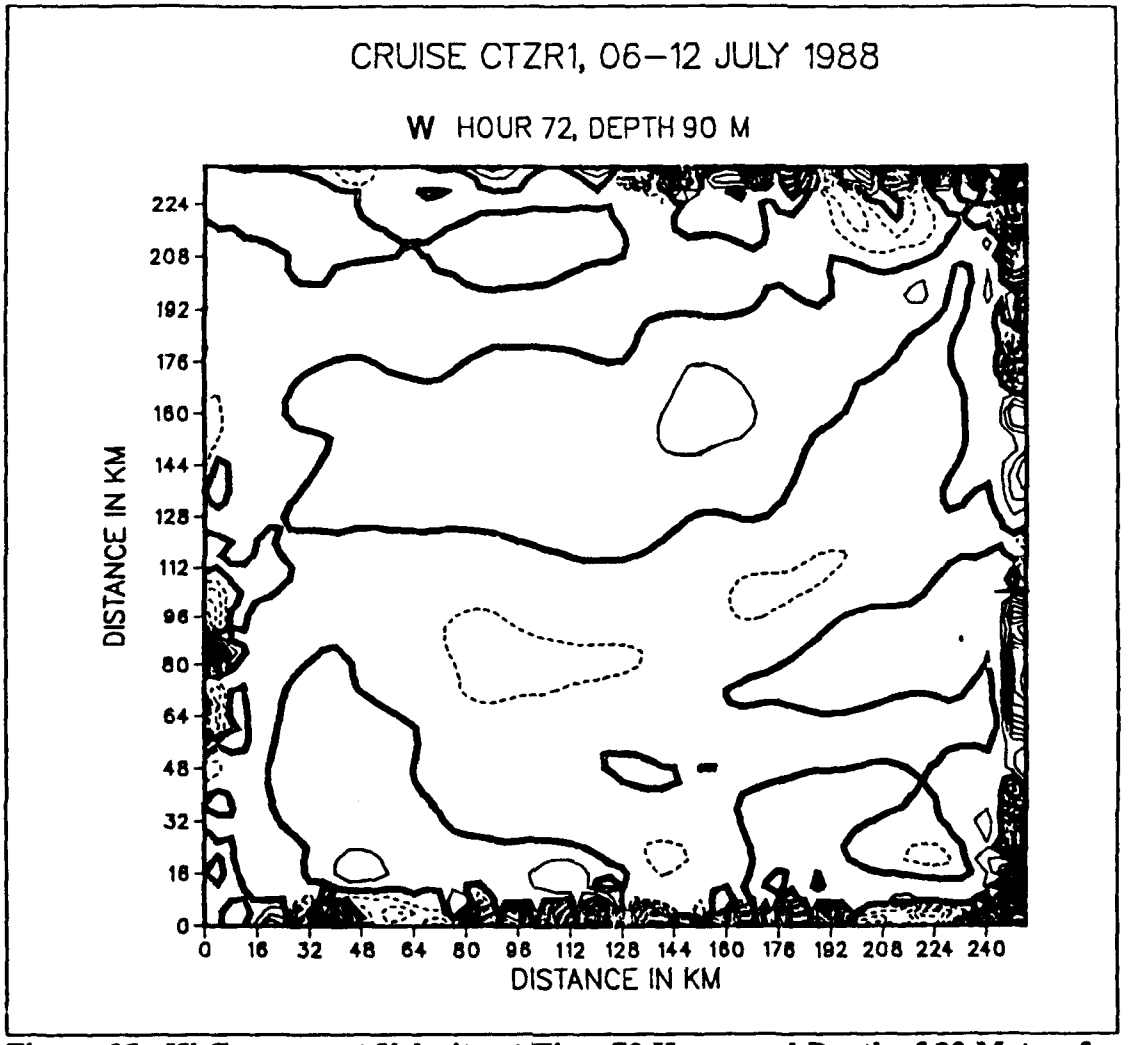

Figure 35. W Component Velocity at Time 72 Hours and Depth of 90 Meters for the Robust Diagnostic: Contour interval .02 cm/s. Dashed lines are negative values.

The second drawback is the boundary noise seen in the w component velocity field at 72 hours (Figure 35). The noise is due to the convergence at the boundaries of inertia-gravity wave energy that has rapidly dispersed away from the interior of the domain during the geostrophic adjustment process. This noise is not as noticeable in the horizontal velocity fields because it is primarily confined to the (smaller) divergent part

of the currents. The most effective method of reducing the boundary noise would be to increase the strength of the sponge, as described above, or to introduce a divergence damper in the (u,v) equations at the boundaries. These drawbacks, however, do not hamper the results of the interior solution as presented here.

D. INTERPRETATION OF THE VERTICAL VELOCITY FIELD IN THE ROBUST DIAGNOSTIC SOLUTION

One of the most significant results of the model generated currents is the predicted field of vertical velocity. The vertical velocity is important in determining the fate of heat, salt and biological material that is advected offshore in squirts and jets in the coastal region. Comparing the w field in Figure 35 with the current field in Figure 34 indicates that the offshore jet is associated with sinking motion, while the onshore part of the jet is associated with rising motion. In this section an attempt is made to understand this result in terms of a quasi-geostrophic vorticity budget.

A simplified form of the vorticity equation is

$$\frac{d\zeta}{dt} = -(\zeta + f)\nabla\cdot\vec{V}, \qquad \{18\}$$

where $\frac{d\zeta}{dt}$ is the total derivative of the relative vorticity and $-(\zeta + f)\nabla\cdot\vec{V}$ is the divergence term (Holton, 1979; Pond and Pickard, 1983). The variation of the coriolis parameter has been neglected for this scale of motion.

Arnone et al. (1990) and Bower (1991) describe the divergence/upwelling and convergence/downwelling phenomena as observed in the Gulf Stream system. The

schematic shown in Figure 36 briefly summarizes the interpretation by these authors. The above equation aids in analyzing the schematic.

As seen from equation {18}, if divergence ($\nabla \cdot \vec{v} > 0$) is present, then the vorticity tendency of the fluid particle is negative, implying a tendency for anticyclonic motion. If convergence ($\nabla \cdot \vec{v} < 0$) is present, then the vorticity tendency is positive, implying a tendency for cyclonic motion (Figure 36). Conversely, if a fluid particle flows from a region of negative vorticity (a ridge) into a region of positive vorticity (a trough), experiencing a positive vorticity tendency, then, according to equation {18}, it must flow through a region of horizontal convergence.

From continuity and equation {18}, the following relationship is true

$$\frac{d\zeta}{dt} = f\frac{\partial w}{\partial z}. \qquad \{19\}$$

From equation {19} with w = 0 at z = 0, a negative vorticity tendency implies upwelling ($\frac{\partial w}{\partial z} < 0$), and a positive vorticity tendency implies downwelling ($\frac{\partial w}{\partial z} > 0$) (Pond and Pickard, 1983). In Figure 36, the vertical upwelling centers are shown upstream of a crest in an area of divergence and downwelling centers are shown downstream of a crest in an area of convergence.

The resulting vertical velocity in the robust diagnostic model (Figures 35 and 37) agree closely with the patterns of Arnone et al. (1990) shown in Figure 36. At 72 hours, areas of downwelling are located downstream of a ridge in the offshore jet in the south central section of the model domain at 65 meters depth. The main area of upwelling is

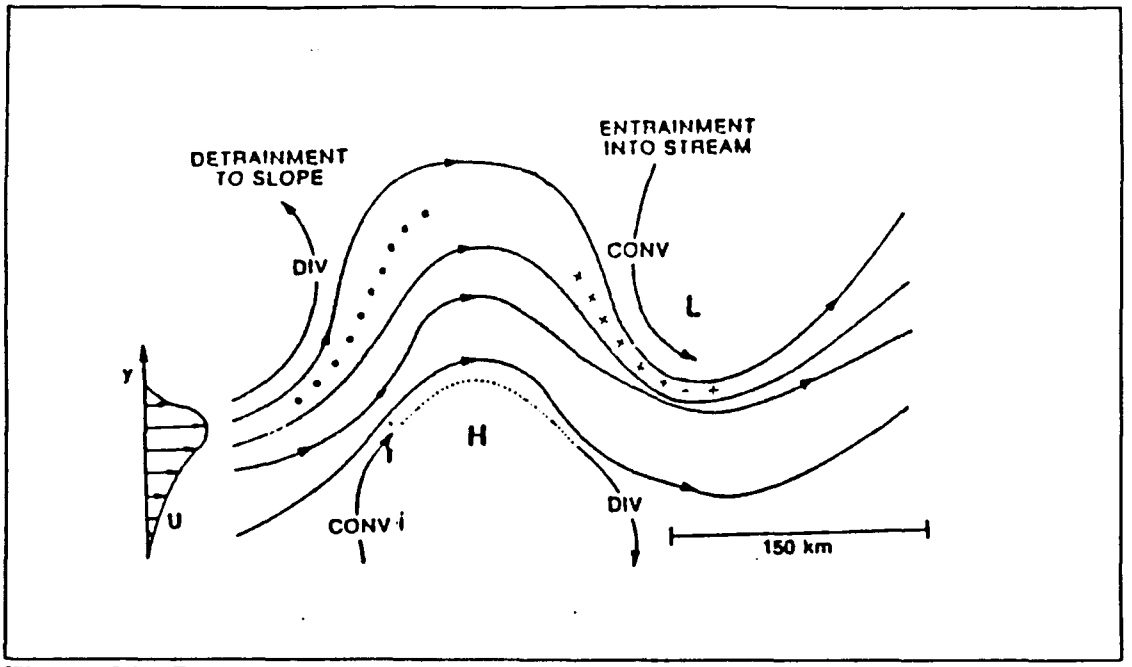

Figure 36. Convergence and Divergence Patterns in a Typical Meander: Vertical upwelling centers are the dots, and downwelling centers are the crosses(from Arnone et al, 1990).

located upstream of the ridge where the flow in the jet is directed onshore (Figure 37). The vorticity field at the same time and depth (Figure 38) supports the above interpretation. The strongest sinking motion in Figure 35 occurs in the region of largest vorticity tendency. This is where fluid particles are flowing across the vorticity "front" south of the offshore jet.

The initial pressure and vorticity fields are shown to illustrate the evolution of these fields with time (Figures 39 and 40). Note the smoothing which occurs in the vorticity field, in particular, between the initial and 72 hour times (Figures 38 and 40). This smoothing is the result of the geostrophic adjustments caused by the robust diagnostic as discussed above. However, the basic pattern of positive vorticity to the left of the jet

(looking downstream) and negative vorticity to the right of the jet is similar to the vorticity pattern of 72 hours.

Equation {19} can be used to estimate the magnitude of upwelling and downwelling expected in the CTZ through scale analysis. These arguments also were used by De Jesus (1990). The right hand side of equation {19} can be scale analyzed as

$$f\frac{\partial w}{\partial z} \sim f\frac{w_{-H}}{H} \qquad \{20\}$$

where w_{-H} is the vertical velocity at depth H, and H is the depth of interest (65 meters). The left hand side of equation {19} becomes

$$\frac{d\zeta}{dt} \sim \frac{U^2}{L^2} \qquad \{21\}$$

when scale analyzed, where U and L are the velocity scale and length scale, respectively.

Equating the right hand and left hand sides, and solving for w gives

$$w \sim R_o \frac{HU}{L} \qquad \{22\}$$

where $R_o = \frac{U}{fL}$ is the Rossby number.

Using the scaling estimates from the advective and geostrophic time scale arguments described above

$$U \sim 50\ cm\ sec^{-1}$$

$$L \sim 50\ km$$

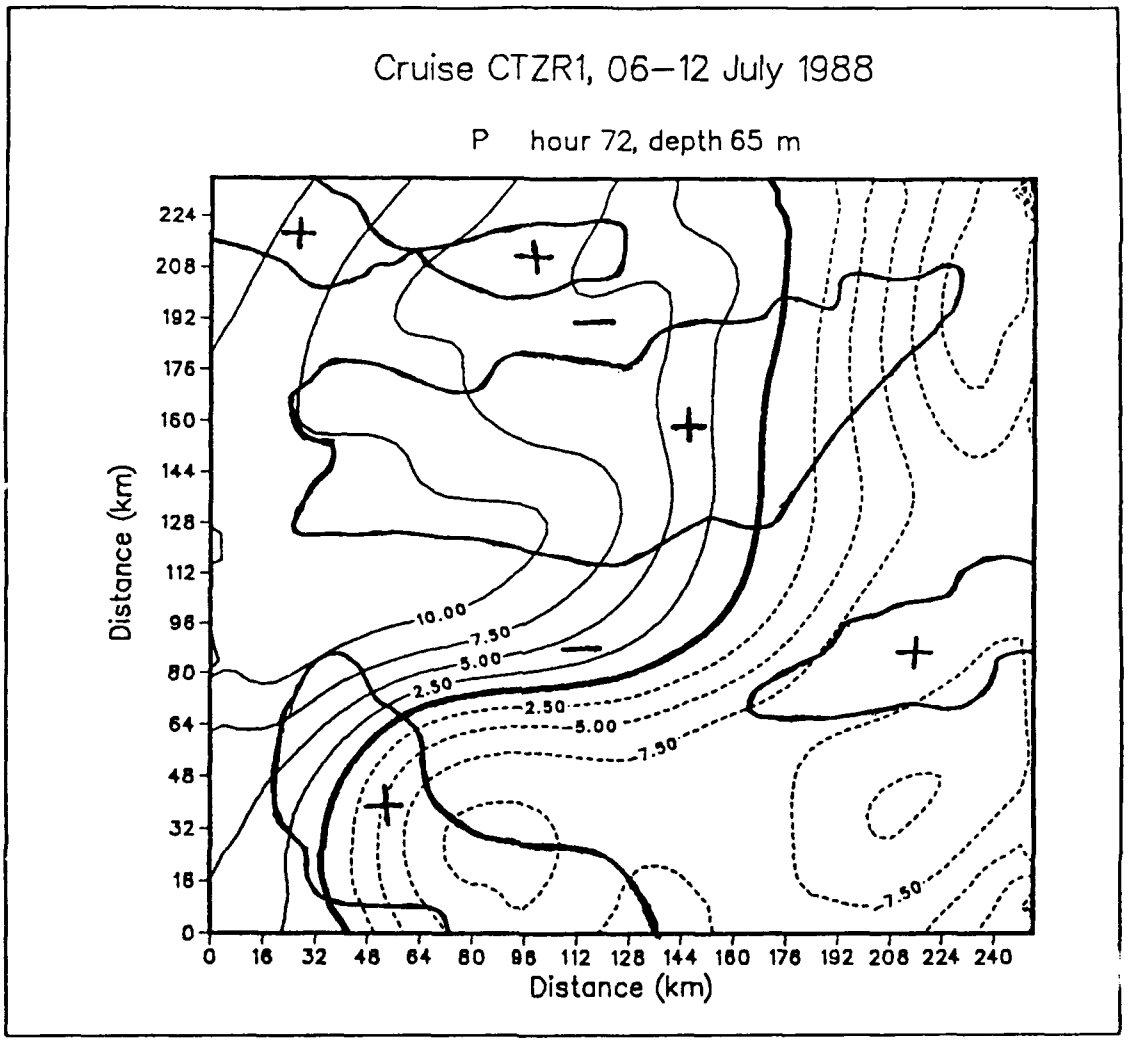

Figure 37. Pressure Field at Time 72 Hours and Depth of 65 Meters for Robust Diagnostic: Vertical velocity pattern from Figure 35 shown with, + = upwelling, - = downwelling.

and

$$f \sim 10^{-4} \text{ sec}^{-1}.$$

Therefore,

$$R_o \sim 0.1$$

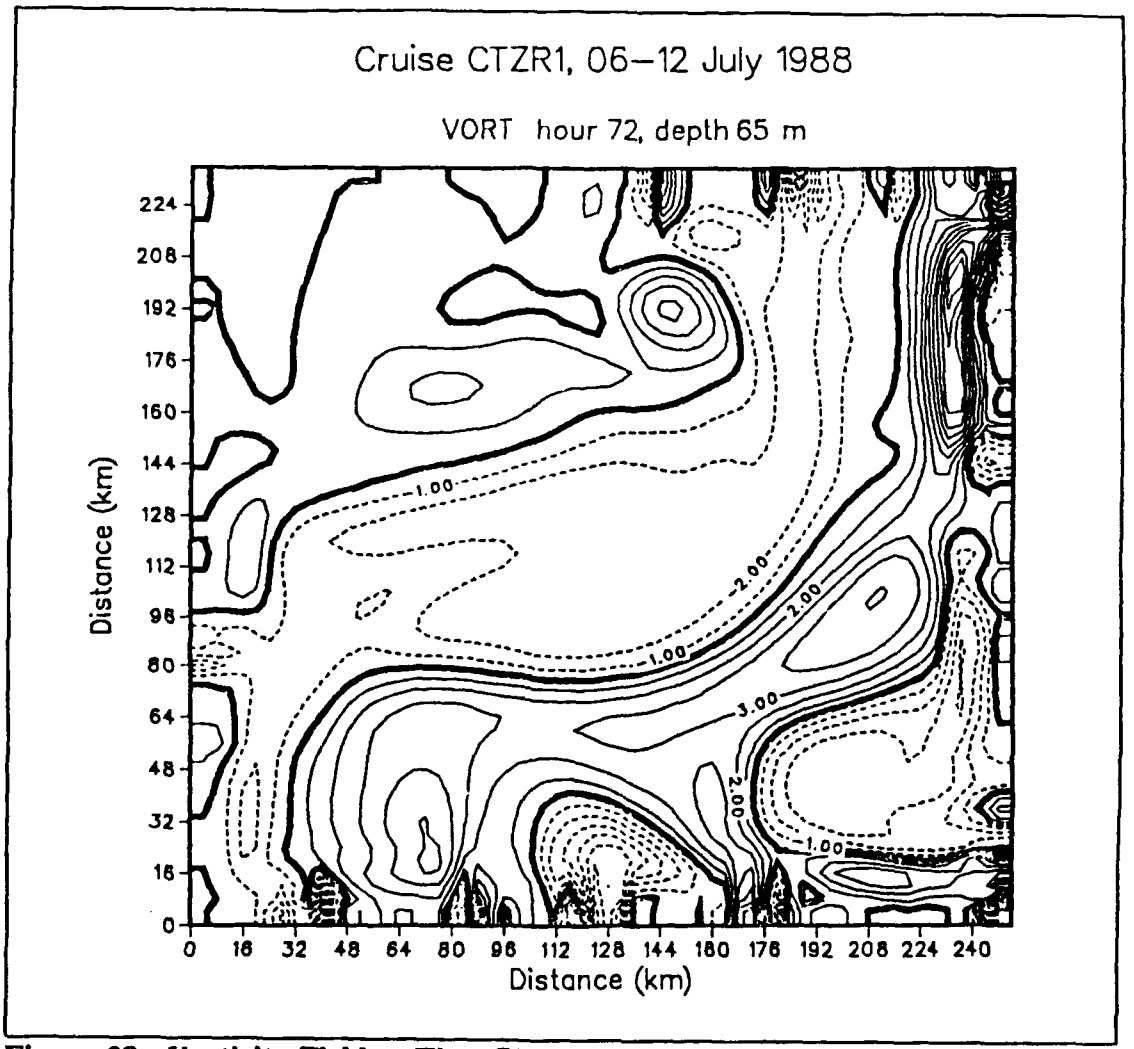

Figure 38. Vorticity Field at Time 72 Hours and Depth of 65 Meters for Robust Diagnostic: Contour interval 1 X 10^{-5} sec^{-1}. Dashed lines are negative values.

and

$$w \sim .01 \ cm \ sec^{-1}$$

or about 6 m day^{-1}, which is similar to the lower observed value of Washburn et al (1990) and Kadko et al. (1990) and similar to the result shown in Figure 35. These scaling

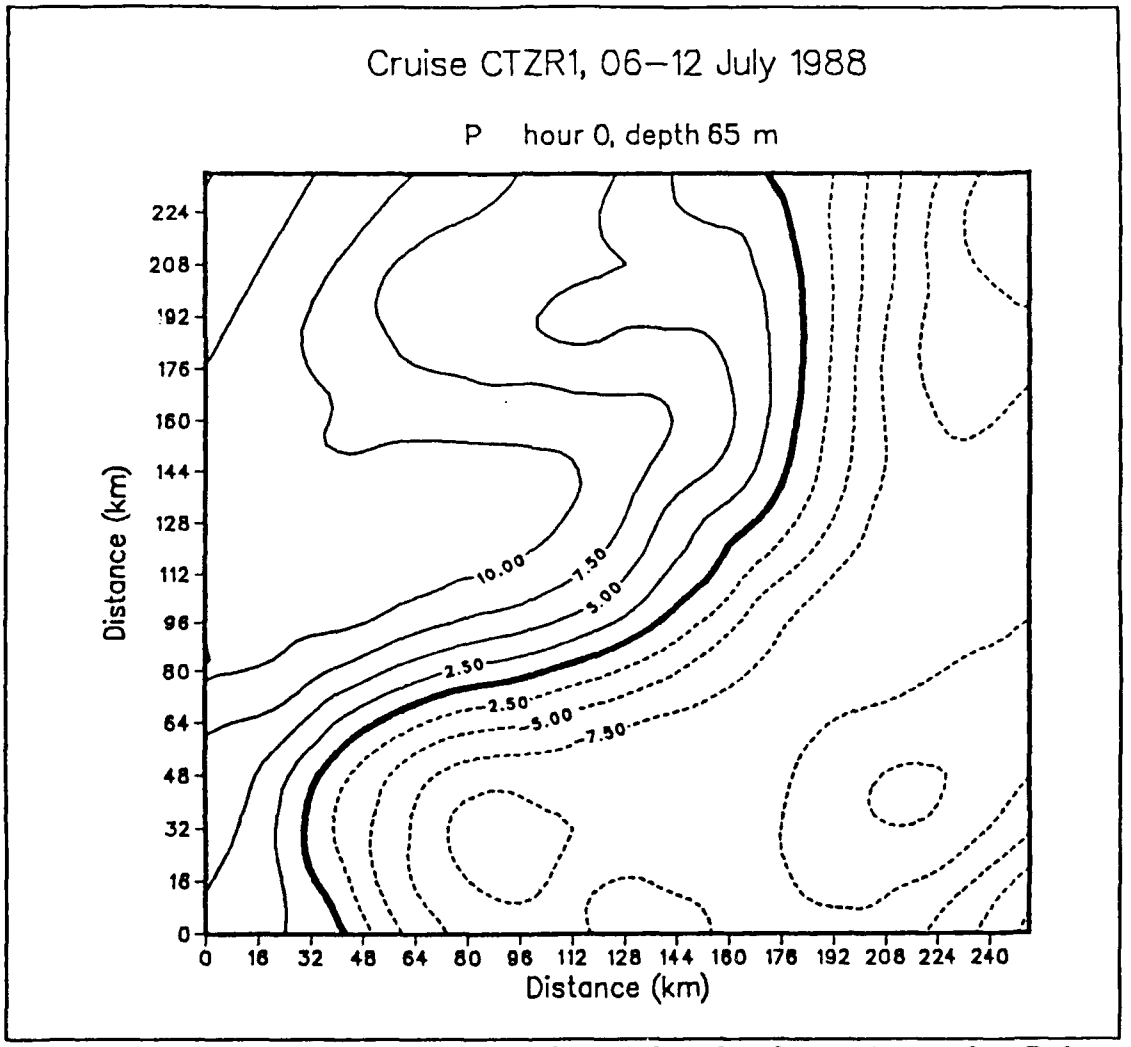

Figure 39. Pressure Field at Time 0 and Depth of 65 Meters for Robust Diagnostic: Contour interval 2.5 cm dynamic height. Dashed lines are negative values.

arguments indicate that the observed values and the robust diagnostic model values are probably characteristic vertical velocity values for the CTZ region. The interpretaion of the w field, as that due to the convergence/divergence pattern that changes the vorticity of fluid particles as they move through a meandering jet with alternating regions of positive and negative vorticity, is probably also characteristic of the CTZ region as it is

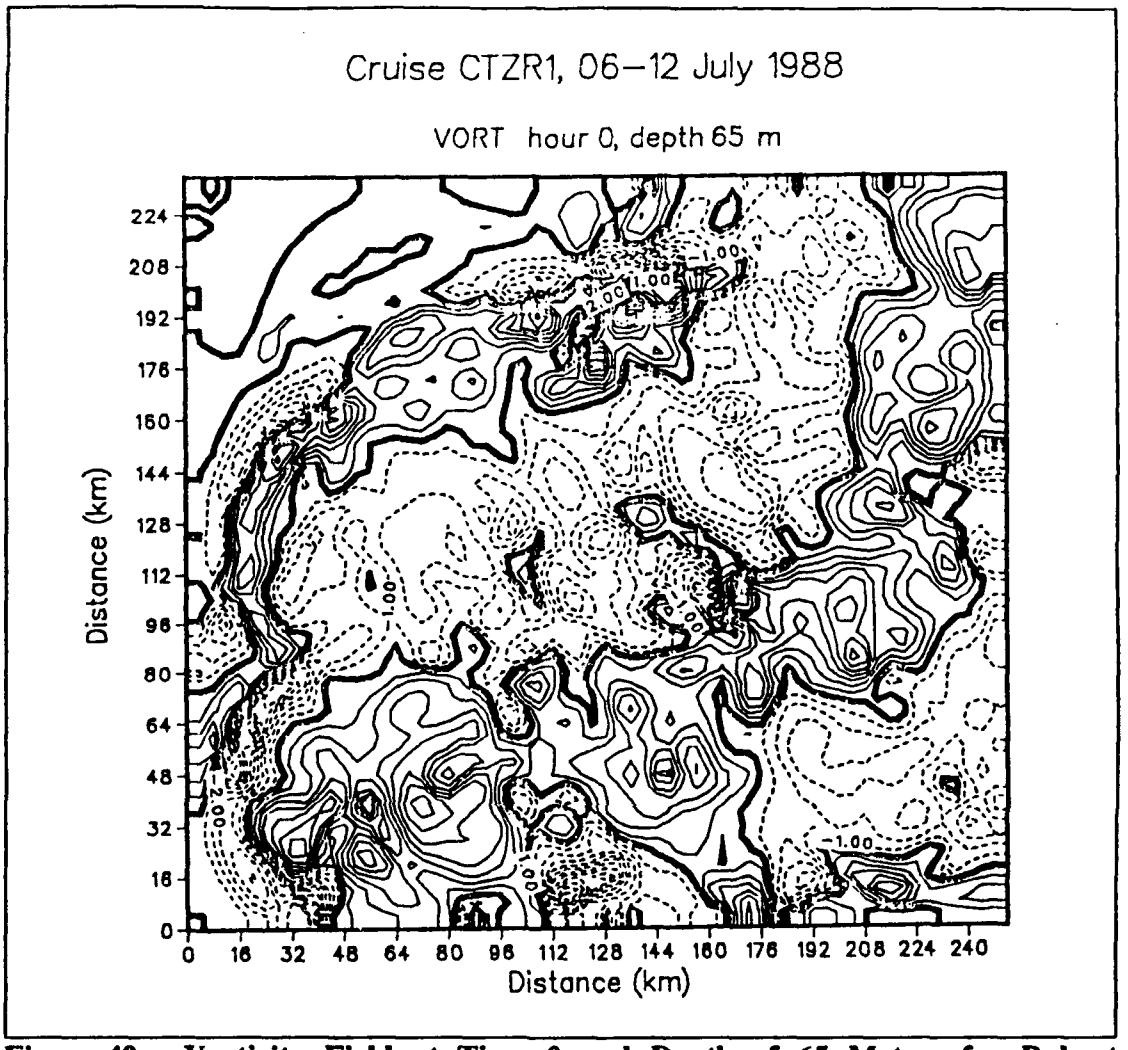

Figure 40. Vorticity Field at Time 0 and Depth of 65 Meters for Robust Diagnostic: Contour interval 1 X 10^{-5} sec^{-1}. Dashed lines are negative values.

of the Gulf Stream (Bower, 1991).

E. ADCP COMPARISONS

The resultant velocity field for the robust diagnostic at time 72 hours and 65 meters depth shows a relatively smooth southward to southwestward flowing jet through the center of the model domain (Figure 34). The magnitude of the velocity following the jet

is fairly steady, and it's direction changes smoothly. The ADCP velocity vectors for CTZR1 at 50 meters depth (Figure 41), on the other hand, indicate the instantaneous observed velocity field is not quite so smooth as indicated in the model. The general shape of the jet in the observed field is reflected in the model field. The magnitude of the velocities in the observed field, however, change spatially to a much greater degree and with more irregularity than in the model. This is probably to be expected since the ADCP data represent instantaneous currents, while the model currents represent geostrophically balanced currents estimated from a fairly coarse sample grid. Also, the maximum observed velocities are in the southwestern corner of the cruise domain where the jet is farthest offshore. In the model, maximum velocities for the jet are indicated in the northeastern part of the domain, closer to the shore.

The smoothing which occurs because of the robust diagnostic seems to eliminate some of the physical small scale disturbances in the velocity field as well as those introduced by the objective analysis as discussed above. Vertical cross-sections of the velocity field (below) also indicate that the model does not represent well the smaller scale characteristics of the observed velocity field. This is to be expected, to some extent, because the model currents represent a balanced state, while the ADCP data are instantaneous currents.

Vertical cross-sections of normal velocity from the model domain are compared to the corresponding ADCP normal velocity cross-sections from the cruise (Figure 42). The cross-sections corresponding to cruise leg B in the northeastern corner of domain show that the observed jet (Figure 43) is smaller in vertical and horizontal extent, and has a

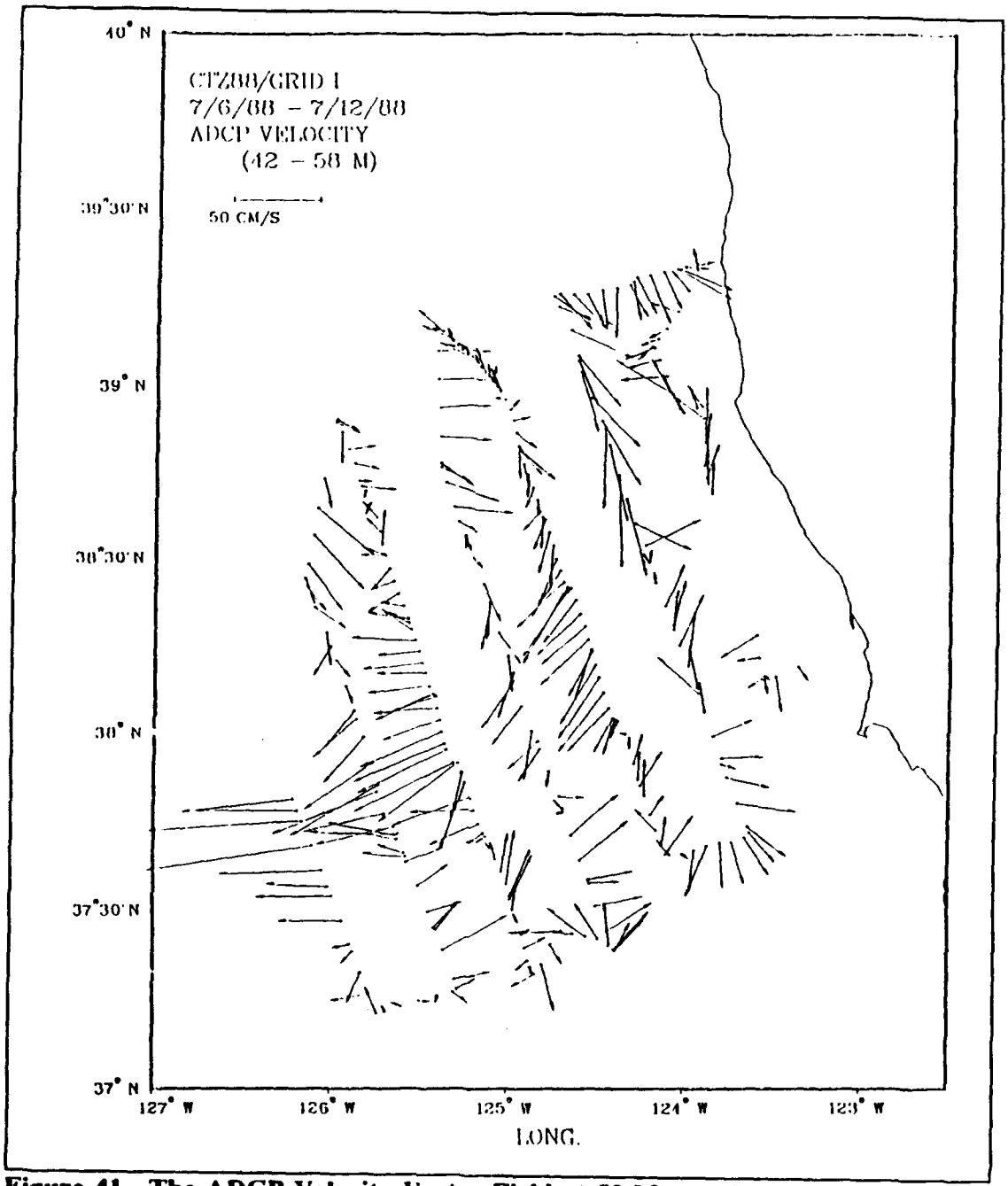

Figure 41. The ADCP Velocity Vector Field at 50 Meters for CTZR1.

lower velocity than the jet developed by the model (Figure 44). The position of the jet in the model is also shifted to the southeast. The observed position of the jet in cruise

leg C (Figure 45) corresponds closely with that developed by the model (Figure 46), but the observed intensity of the jet is not as great as that developed by the model. The cross-sections for cruise leg D have similar characteristics to those of cruise leg C(Figures 47 and 48). Cruise legs E, F and G cross-sections, however, show an increasing agreement in the magnitude as well as the position of the observed jet and the modeled jet (Figures 49, 50, 51, 52, 53 and 54). In general, note that the model velocity cross-sections for all legs are much smoother than those for the ADCP velocities. Smaller scale disturbances do not appear in the model cross-sections because of the balanced nature of the currents that are represented, and the lower resolution of CTD stations used to initialize the model. The discrepancy between model and ADCP data below the surface jet (i.e. below 200 m), however, cannot be attributed to smaller scale imbalanced flows in ADCP data because the currents at that depth should be in dynamic balance.

There are several possible reasons why the ADCP and model currents are in closer agreement farther offshore. Topographic effects, which are neglected in the model, could produce the increasing agreement between observed velocities and modeled velocities with progression from northeast to southwest through the model. Boundary effects in the model could also play a part, especially in the northeast corner of the model domain where inflow of the jet is occurring. In addition, the boundary probably affects the model cross-section corresponding to cruise leg G (Figure 54). Note the reverse flow which occurs in the extreme southeastern part of this leg which does not occur in the observed velocity field (Figure 53). More rigorous statistical studies, and robust diagnostic studies with topography, wind and heat flux forcing, and barotropic currents included, are

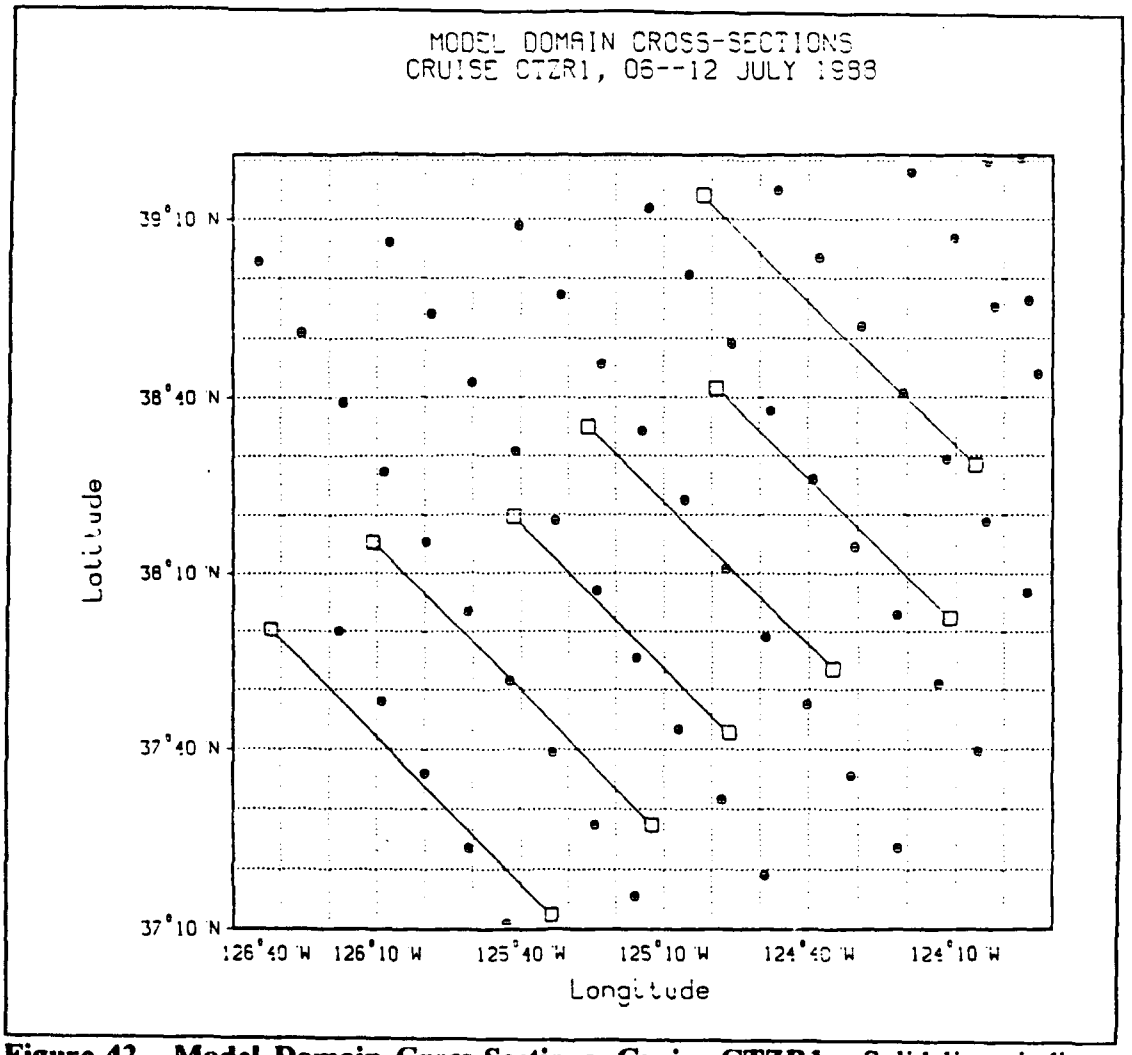

Figure 42. Model Domain Cross-Sections, Cruise CTZR1: Solid lines indicate model cross-sections. Diagonal rows of dots are cruise legs A through G from northeast to southwest.

required before a better interpretation of the comparison between ADCP data and model currents can be made.

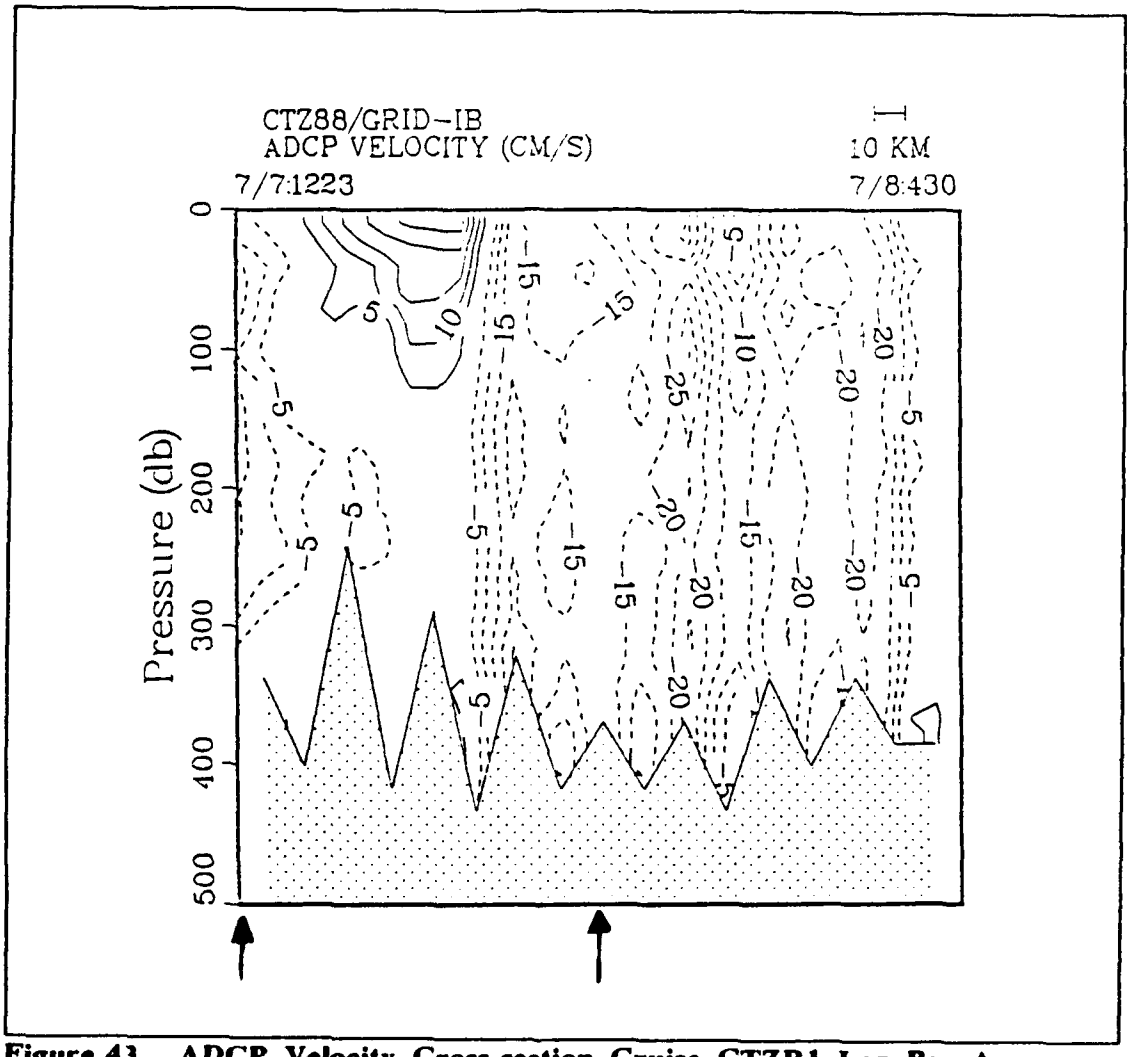

Figure 43. ADCP Velocity Cross-section Cruise CTZR1 Leg B: Arrows are boundaries of corresponding model cross-section. Dashed lines indicate northeastward flow. Northwest is to left. Contour interval 5 cm/s

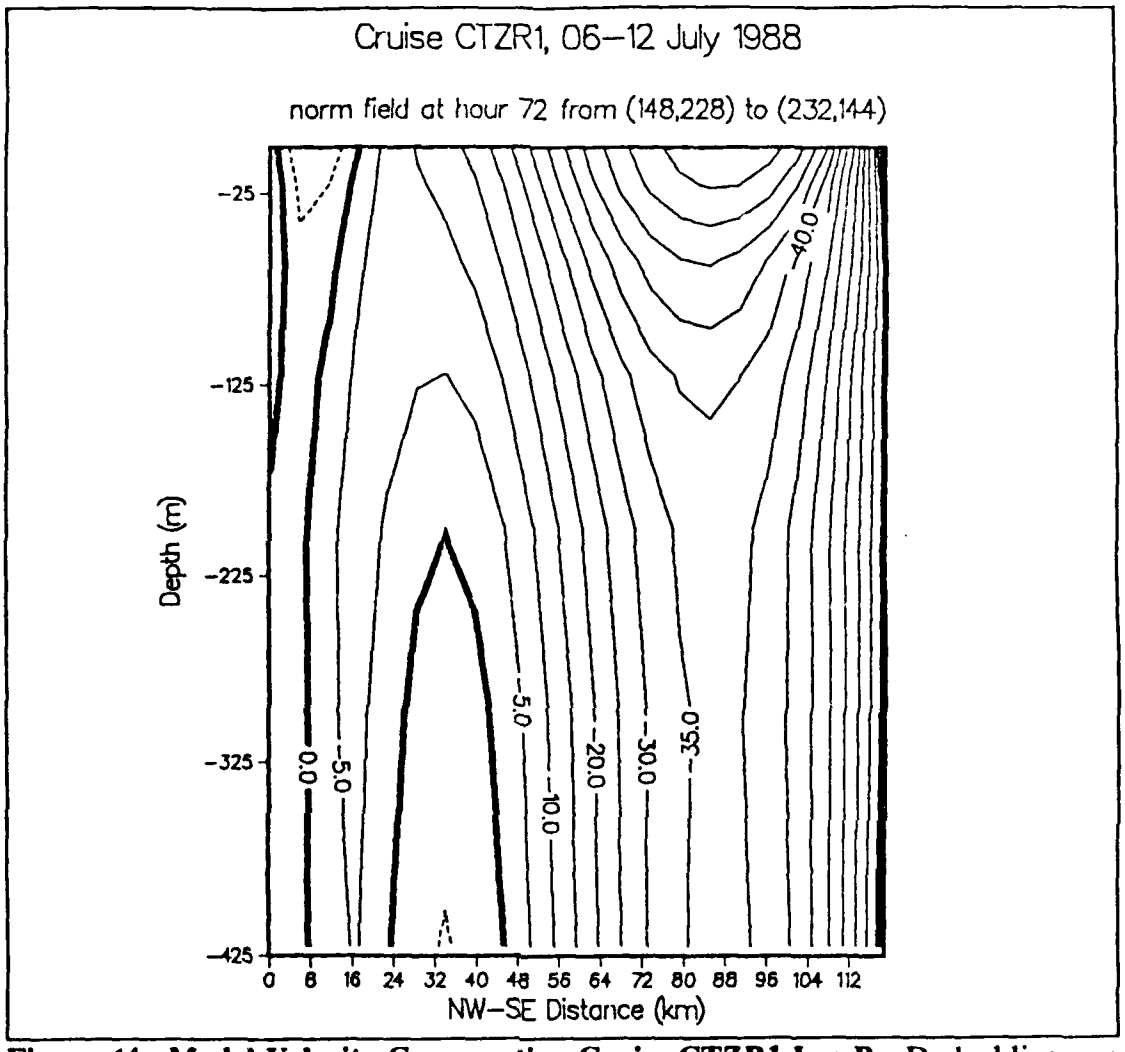

Figure 44. Model Velocity Cross-section Cruise CTZR1 Leg B: Dashed lines are northeastward flow. Northwest is to left. Contour interval 5 cm/s.

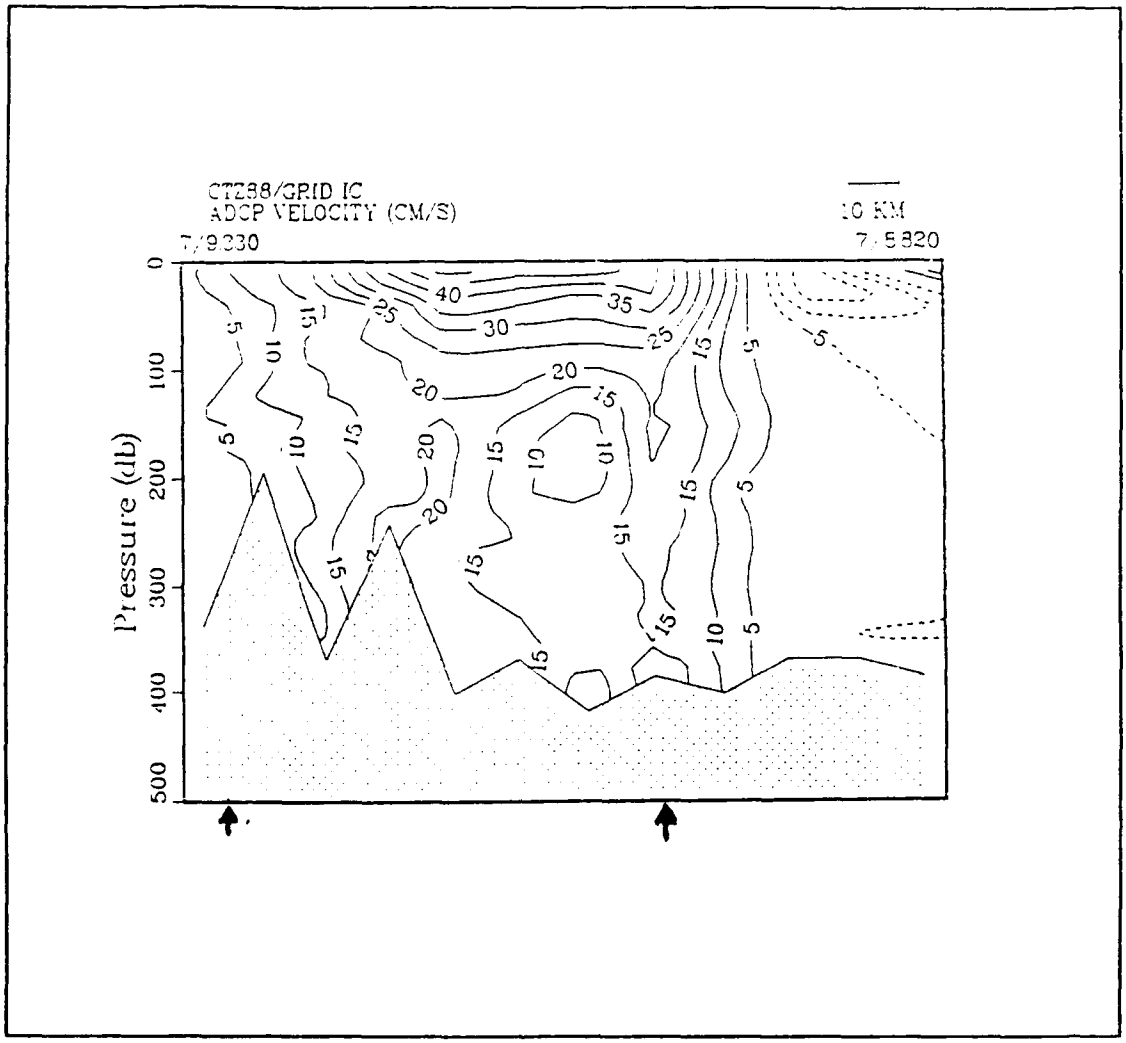

Figure 45. ADCP Velocity Cross-section Cruise CTZR1 Leg C: Conventions and contour interval are same as in Figure 43.

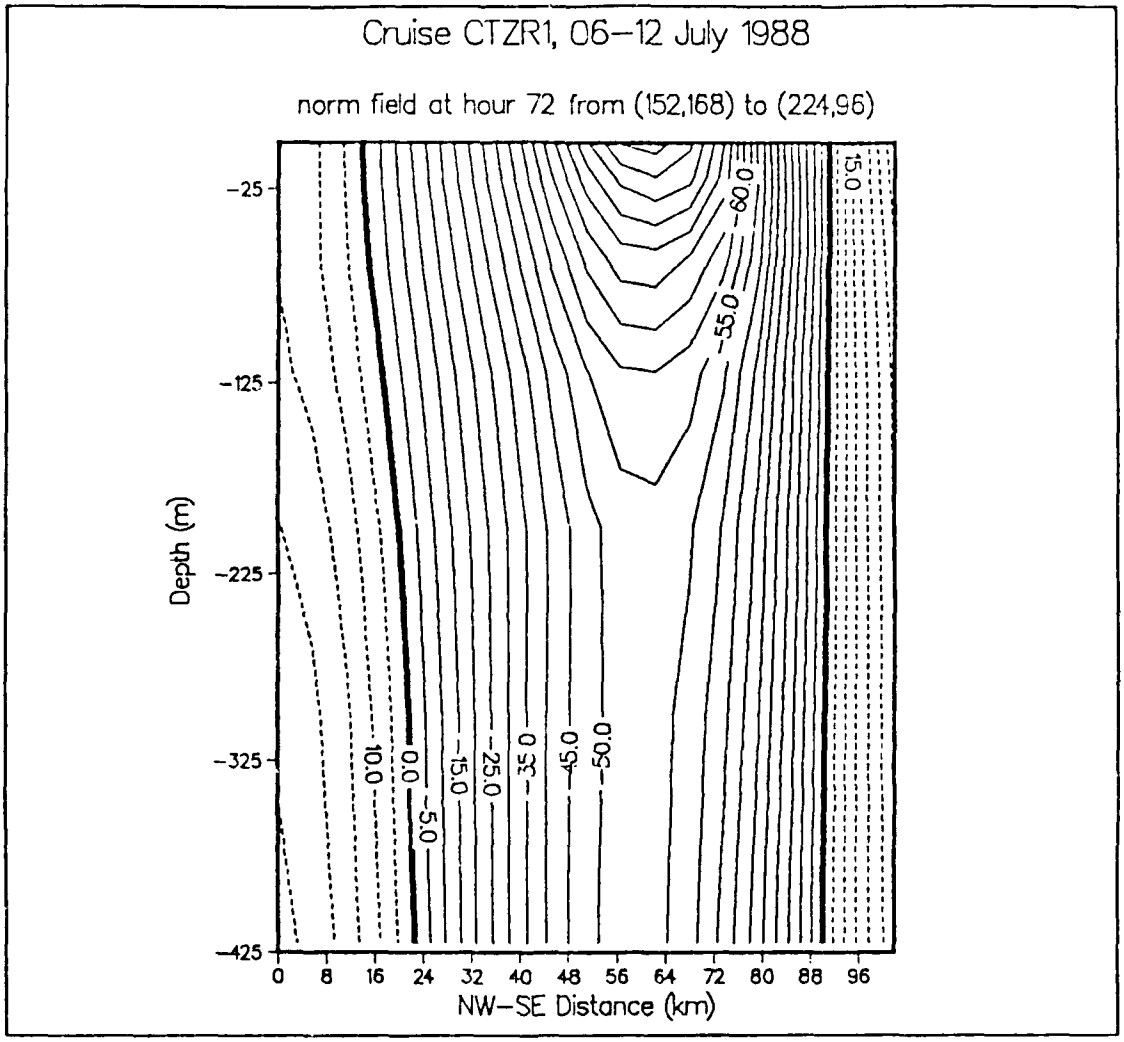

Figure 46. Model Velocity Cross-section Cruise CTZR1 Leg C: Dashed lines are northeastward flow. Northwest is to left. Contour interval 5 cm/s.

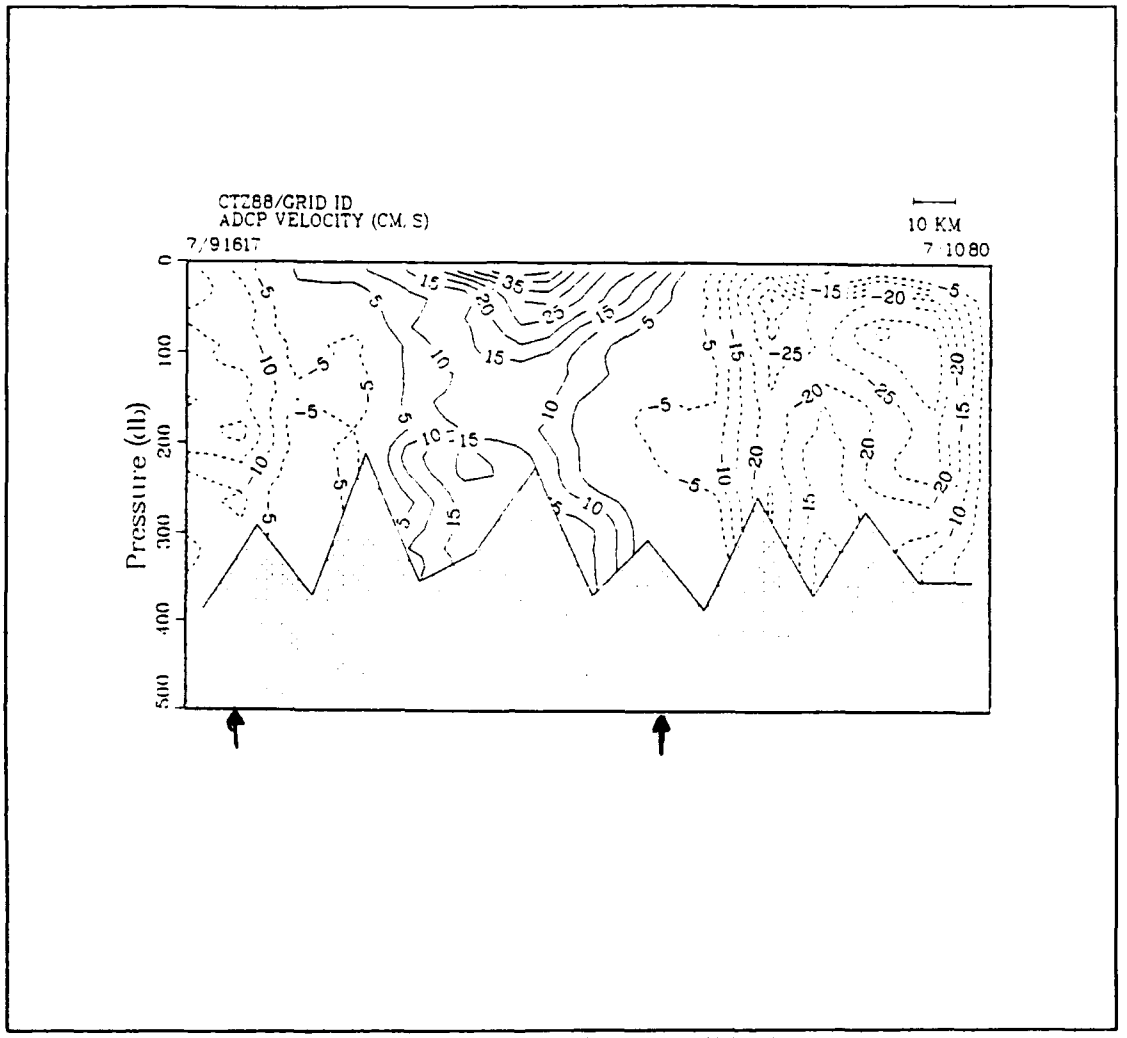

Figure 47. ADCP Velocity Cross-section Cruise CTZR1 Leg D: Conventions and contour interval are the same as in Figure 43.

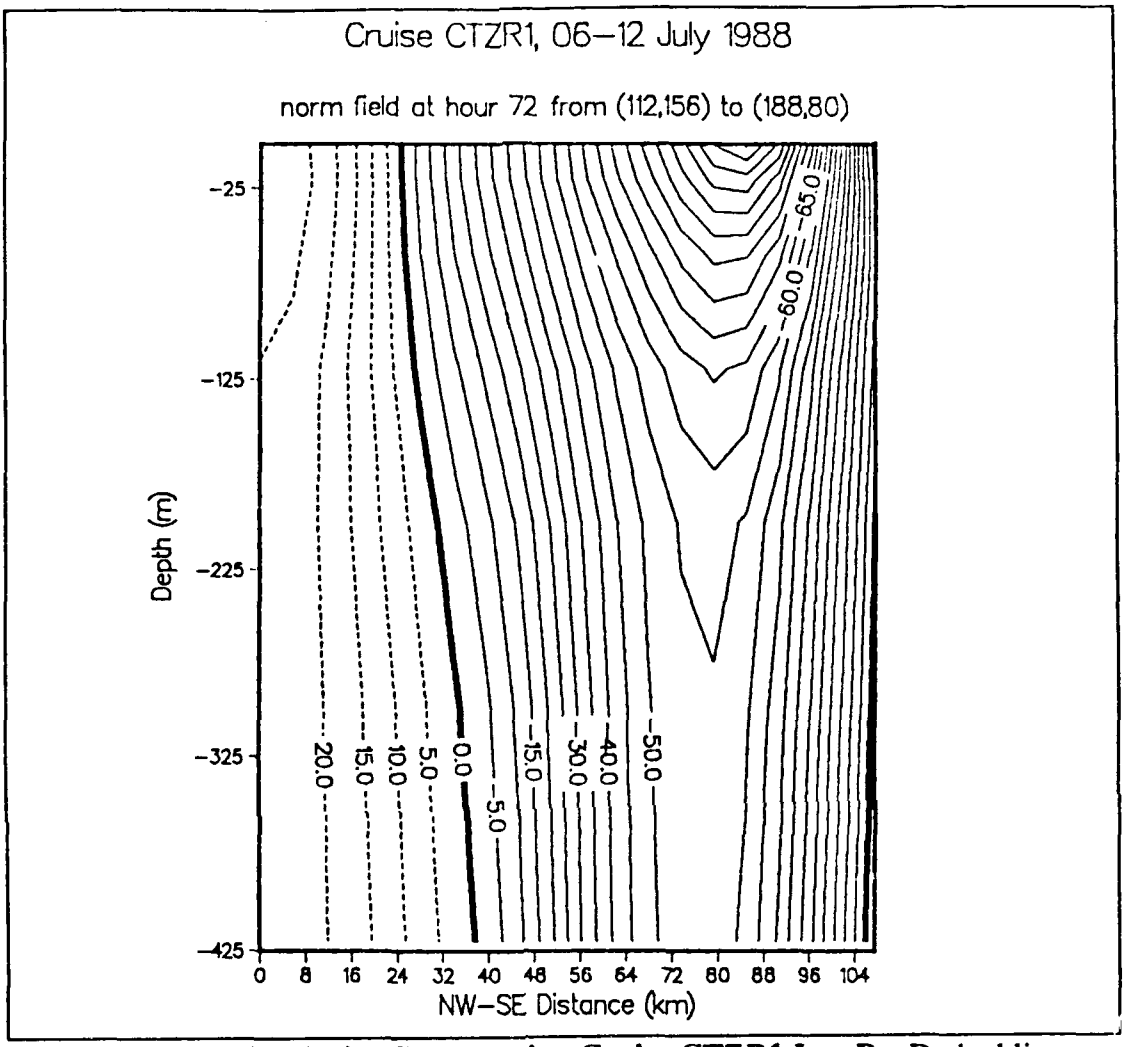

Figure 48. Model Velocity Cross-section Cruise CTZR1 Leg D: Dashed lines are northeastward flow. Northwest is to left. Contour interval 5 cm/s.

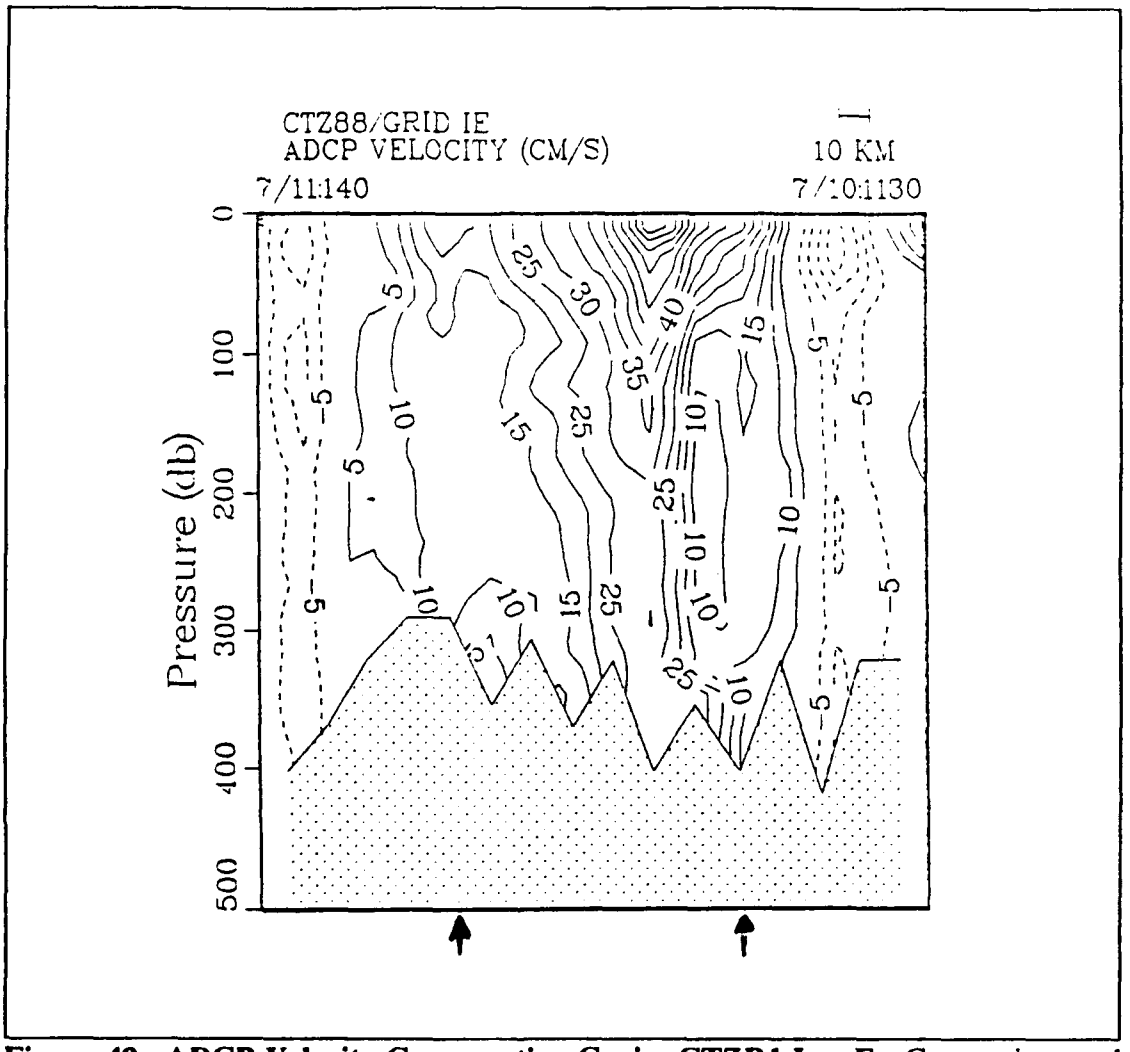

Figure 49. ADCP Velocity Cross-section Cruise CTZR1 Leg E: Conventions and are contour interval are the same as in Figure 43.

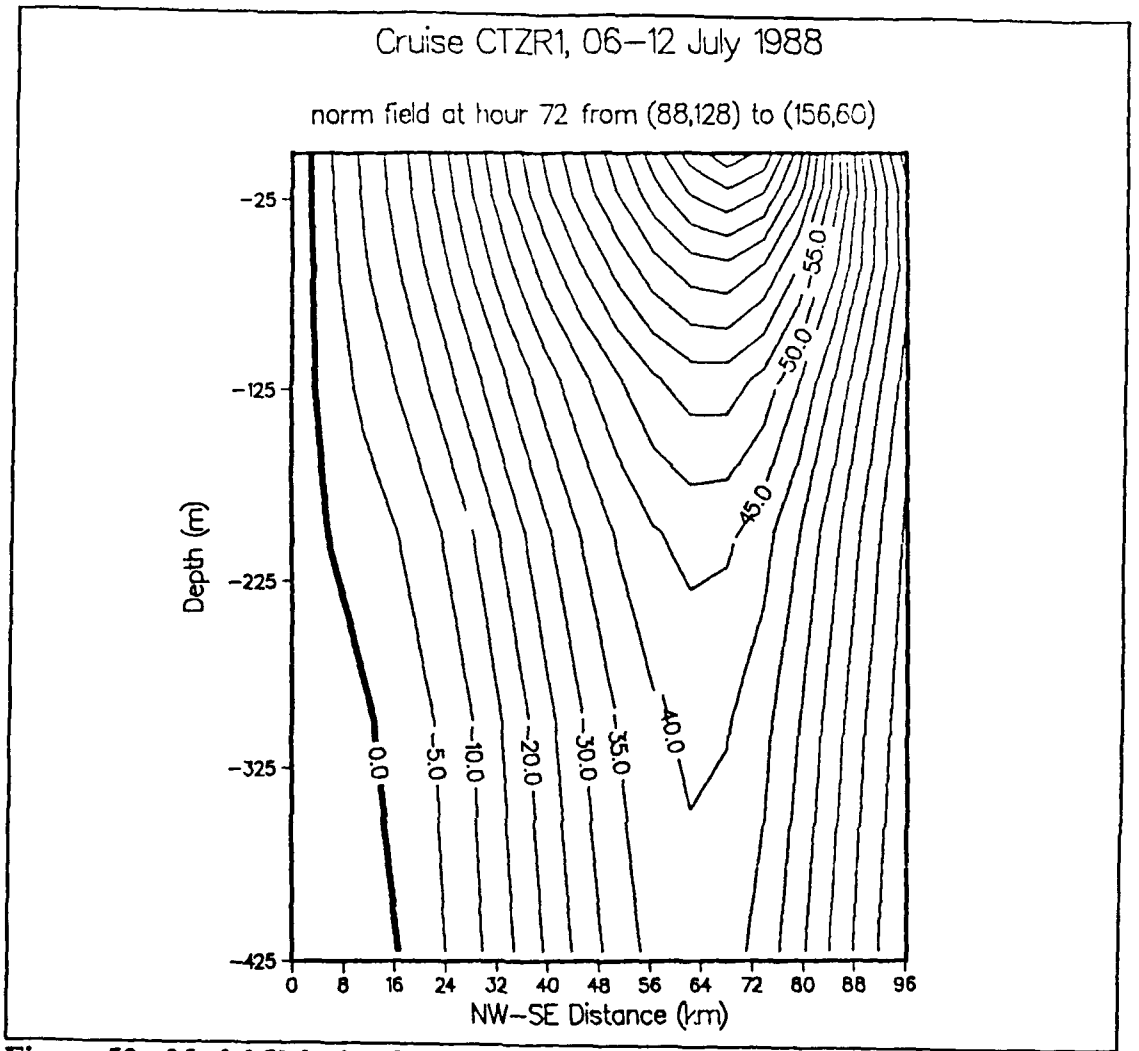

Figure 50. Model Velocity Cross-section Cruise CTZR1 Leg E: Dashed lines are northeastward flow. Northwest is to left. Contour interval 5 cm/s

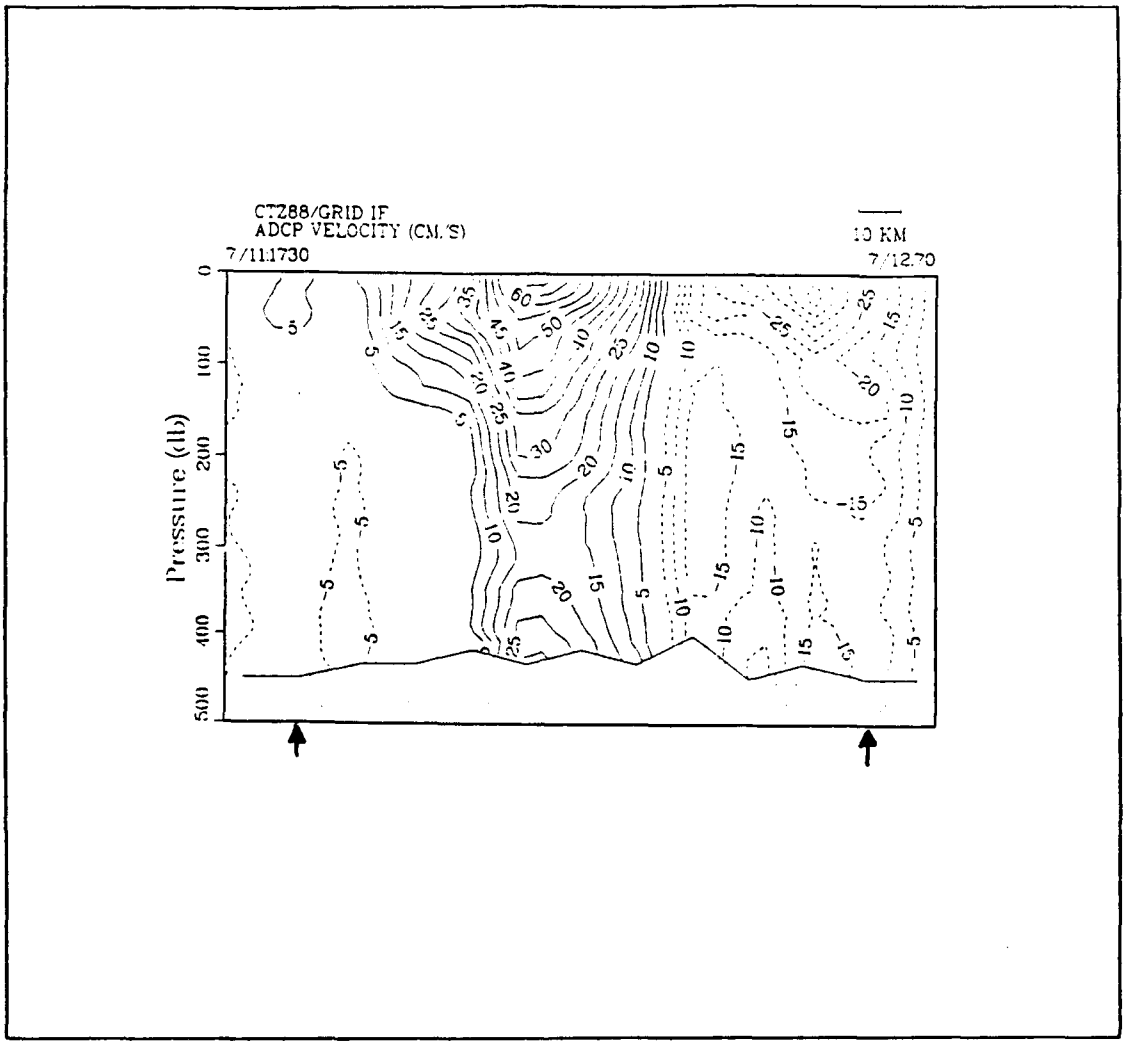

Figure 51. ADCP Velocity Cross-section Cruise CTZR1 Leg F: Conventions and contour interval are the same as in Figure 43.

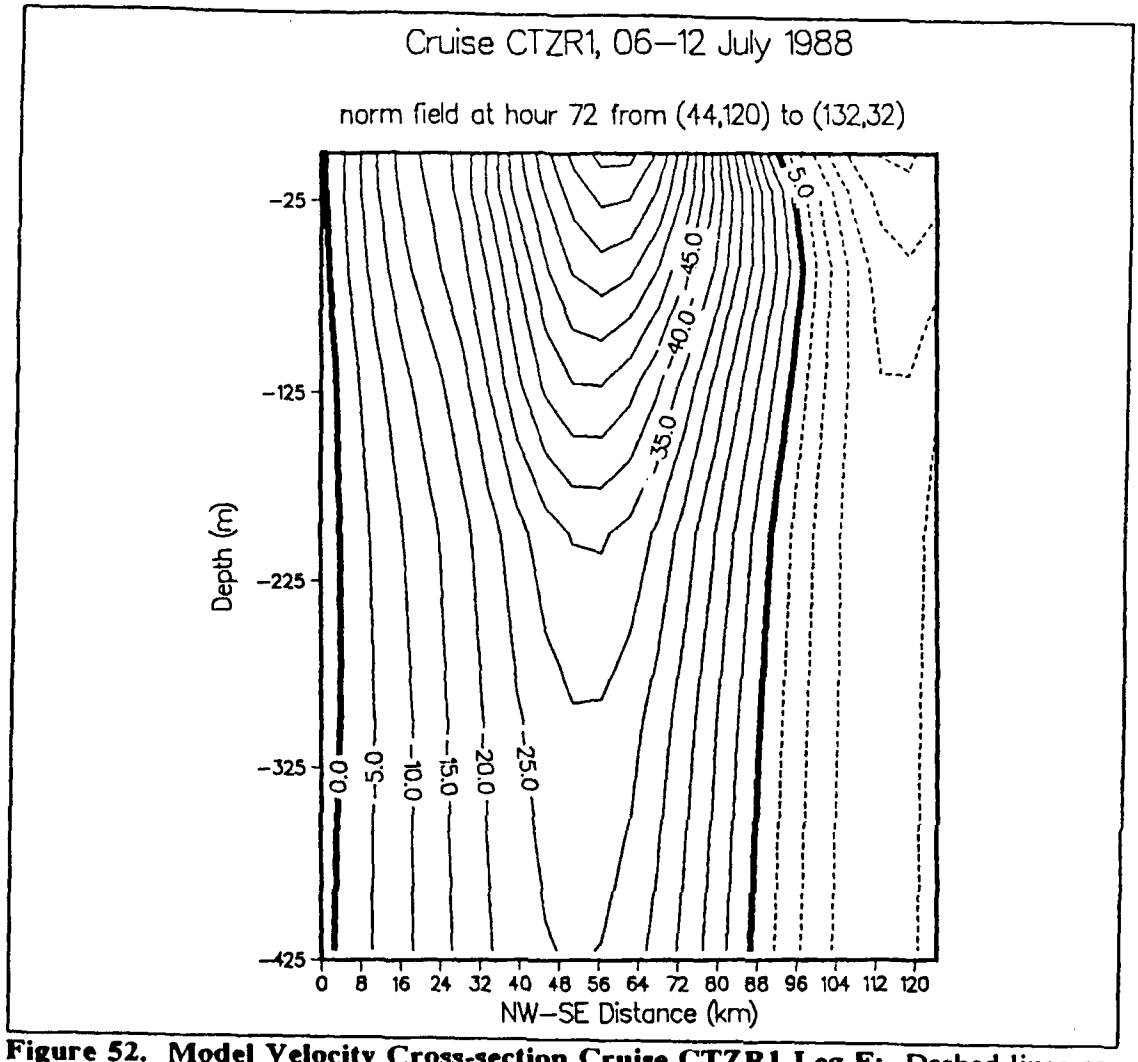

Figure 52. Model Velocity Cross-section Cruise CTZR1 Leg F: Dashed lines are northeastward flow. Northwest is to left. Contour interval 5 cm/s.

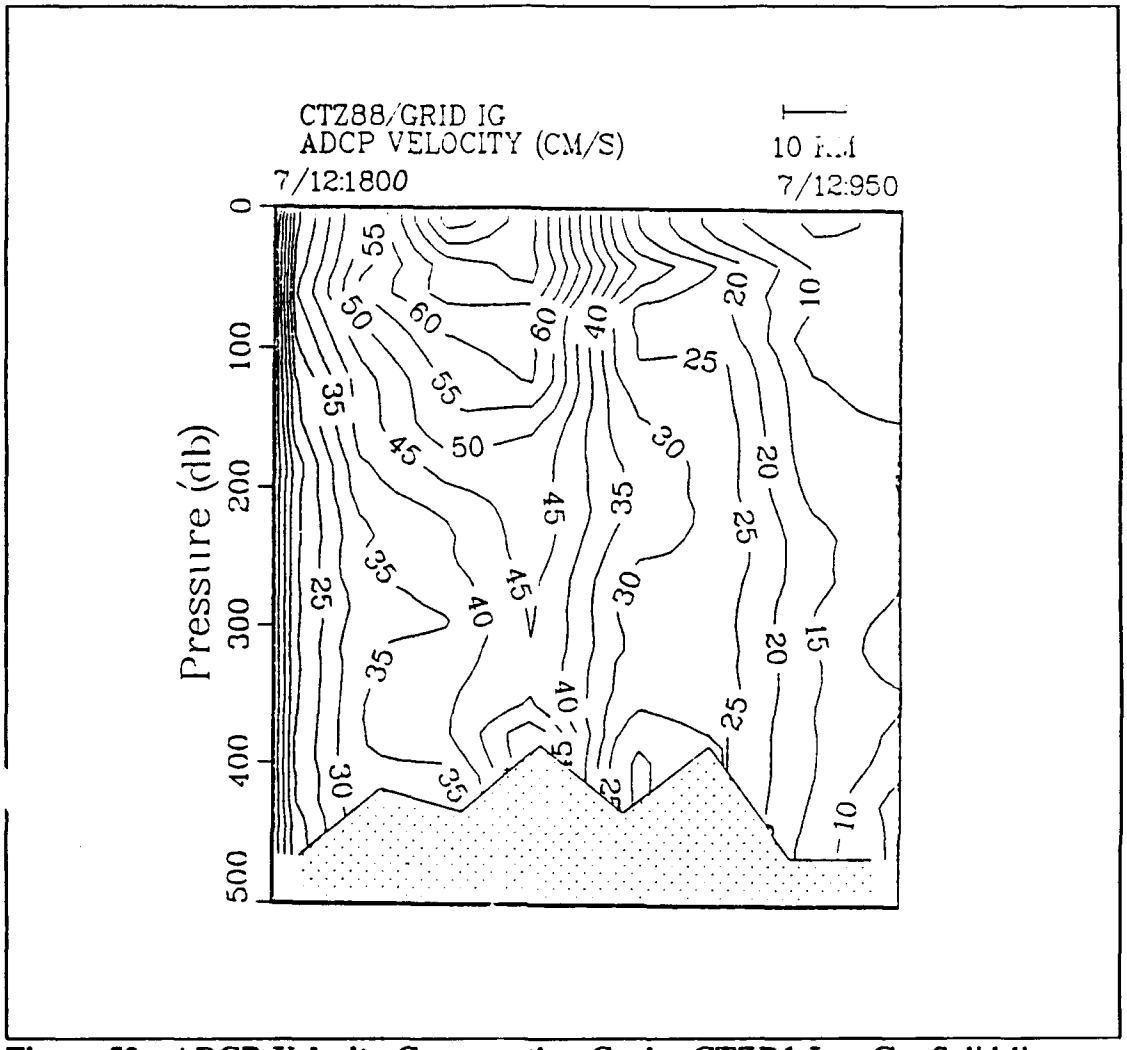

Figure 53. ADCP Velocity Cross-section Cruise CTZR1 Leg G: Solid lines are southwestward flow. Northwest is to left. Contour interval 5 cm/s.

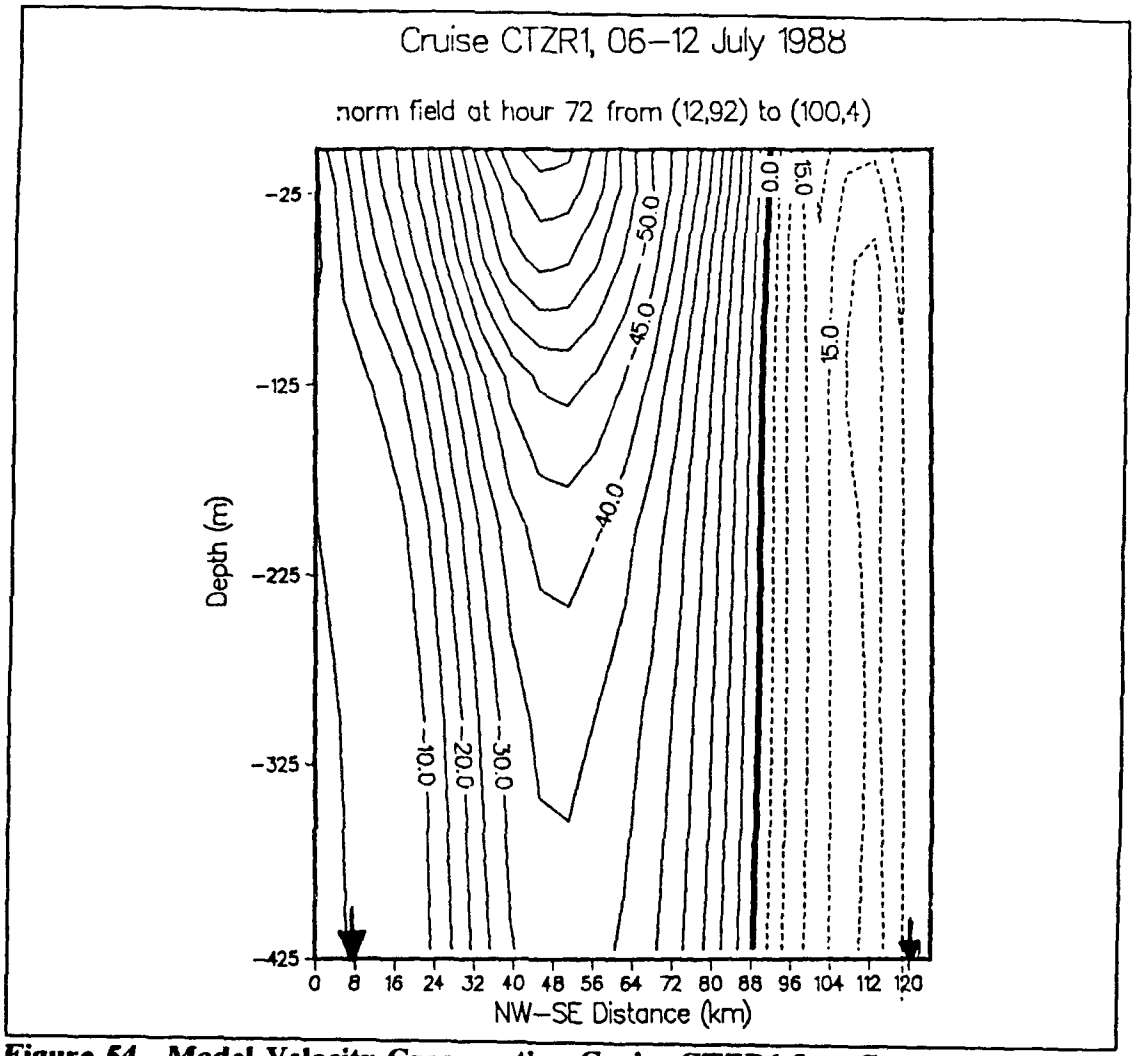

Figure 54. Model Velocity Cross-section Cruise CTZR1 Leg G: Arrows are boundaries of corresponding ADCP cross-section. Dashed lines are northeastward flow. Northwest is to left. Contour interval 5 cm/s.

IV. SUMMARY AND CONCLUSIONS

The "interface matching" formulation of determining the deep solution for the disturbance σ_θ gives reasonable results when input into the primitive equation model used in this study. No comparisons, however, were made between these results and those which would be obtained using the "mean conserving" or the "energy conserving" formulations. A deep profile comparison of the "interface matching", the "mean conserving", and the "energy conserving" formulations with observed data is needed to determine which method gives results which most closely resemble the observed vertical ocean structure. In addition, a comparison is needed between the results obtained by the exact method and those obtained by the linear least squares method of solving the minimization problem set up between equations (1) and (2) as described in Chapter II.

The robust diagnostic version of the model gives better results than the density diagnostic version of the model for this case. The robust diagnostic version of the model allows a mutual dynamic adjustment to occur between the σ_θ and velocity fields. Consistent with the theory of geostrophic adjustment, the smaller scale features in the σ_θ field are altered the most by this adjustment process. The improvement of the robust diagnostic over the density diagnostic versions, therefore, will probably hold true for the other CTZ cases as well. The accuracy with which the robust diagnostic version of the model diagnoses the magnitude and pattern of the observed vertical velocity associated with jets in the CTZ has not been accurately determined. However, the model results that

indicate horizontal convergence and sinking motion of the order of 5-20 m/day all along the offshore directed part of the jet are certainly consistent with the few observed estimates that are presently available. A sensitivity study to determine the optimum damping time scale for the robust diagnostic for reducing advective effects is desirable, but, as stated in Chapter III, the fact that advective effects were apparent in this particular robust diagnostic version did not adversely affect the results.

Comparisons of ADCP with robust diagnostic model velocity vertical cross-sections indicated that small-scale features of the observed velocity field were not reflected in the model velocity field. This smoothing of small-scale features by the robust diagnostic was seen in all fields, horizontal as well as vertical. The smoothing eliminated some undesirable noise resulting from the multi-layer objective analysis scheme, but also eliminated some physical features.

The vertical cross-section comparison between ADCP velocities and robust diagnostic model velocities also showed that agreement between the two increased from northeast to southwest in the model domain. In addition, ADCP velocities were higher in the jet when it was farthest offshore in the southwest corner of the model domain while model velocities were higher in the jet where it was closer to shore in the northeast corner. A hypothesis for this difference is the model's neglect of topographic effects, wind and heat flux forcing. An interpretation of robust diagnostic model results with these effects added is required to test this hypothesis.

REFERENCES

Abbott, M. R., and P. M. Zion, 1985: Satellite observations of phytoplankton variability during an upwelling event. *Cont. Shelf Res.*, **4**, 661-680.

Arakawa, A., and V. R. Lamb, 1977: Computational design of the basic dynamical processes of the UCLA general circulation model. *Methods in Computational Physics*, J. Chang, ed., Academic Press, **17**, 173-265.

Amone, R. A., R. W. Nero, J. M. Jech, and I. De Palma, 1990: Acoustic imaging and biological and physical processes within Gulf Stream meanders. *EOS*, **71**, 982.

Bower, A. S., 1991: A simple kinematic mechanism for mixing fluid parcels across a meandering jet. *J. Phys. Oceanogr.*, **21**, 173-180.

Brink, K. H., 1983: The near-surface dynamics of coastal upwelling. *Prog. Oceanog.*, **12**, 223-257.

Carter, E. F., and A. R. Robinson, 1987: Analysis models for the estimation of oceanic fields. *J. Atmos. Ocean. Tech.*, **4**, 49-74.

Coastal Transition Zone Group, 1988: The coastal transition zone program. *EOS*, **69**, 698, 699, 704, 707.

de Jesus, R. E., 1990: A diagnostic study of the velocity structure of a meandering jet using a primitive equation model with dynamic mode initialization. Master's Thesis, Naval Postgraduate School, Monterey, CA, 68 pp.

Flament, P., L. Armi, and L. Washburn, 1985: The evolving structure of an upwelling element. *J. Geophys. Res.*, **90**, 11765-11778.

Foster, K. W., 1989: *Local Area Forecaster's Handbook.* Naval Oceanography Command Facility, San Diego, 116 pp.

Haney, R. L., 1985: Midlatitude sea surface temperature anomalies: a numerical hindcast. *J. Phys. Oceanogr.*, **15**, 787-799.

Hickey, B. M., 1979: The California current system: hypothesis and facts. *Prog. in Oceanogr.*, **8**, 191-279.

Hildebrand, F. B., 1965: *Methods of Applied Mathematics, 2nd ed.*. Prentice Hall, Inc., 362 pp.

Holton, J. R., 1979: *An Introduction to Dynamic Meteorology, Vol. 23: International Geophysics Series, 2nd ed.*. Academic Press, Inc., 391 pp.

Huyer, A., 1983: Coastal upwelling in the California current system. *Prog. Oceanog.*, **12**, 259-284.

_____, P. M. Kosro, J. Fleischbein, S. R. Ramp, T. P. Stanton, L. Washburn, F. Chavez, and T. Cowles, 1990: Currents and water masses of the coastal transition zone off northern California, June to August 1988. *J. Geo. Res.*, submitted.

Kadko, D. C., L. Washburn, and B. Jones, 1991: Evidence of subduction within cold filaments of the N. California coastal transition zone. *J. Geo. Res.*, submitted.

Kelly, K. A., 1985: The influence of winds and topography on the sea surface temperature patterns over the northern California slope. *J. Geo. Res.*, **90**, 11783-11798.

Lorenzetti, J. A., and J. D. Wang, 1986: On the use of wave-absorbing layers in the treatment of open boundaries in numerical coastal circulation models. *Appl. Math. Mod.*, **10**, 339-345.

Pond, S., and G. L. Pickard, 1983: *Introductory Dynamic Oceanography, 2nd ed.*. Pergamon Press, Ltd., 241 pp.

Rienecker, M. M., C. N. K. Mooers, and A. R. Robinson, 1987: Dynamical interpolation and forecast of the evolution of mesoscale features off northern California. *J. Phys. Oceanogr.*, **17**, 1189-1213.

Sarmiento, J. L., and K. Bryan, 1982: An ocean transport model for the north Atlantic. *J. Geo. Res.*, **87**, 394-408.

Stanton, T. P., J. A. Stockel, M. L. Batteen, and S. R. Ramp, 1990: Upper ocean response to a wind relaxation event in the coastal transition zone. *J. Geo. Res.*, submitted.

Strub, P. T., and the CTZ Group, 1990: The nature of the cold filaments in the CCS. *J. Geo. Res.*, submitted.

Tchernia, P., 1980: *Descriptive Regional Oceanography*. Pergamon Press Inc., 253 pp.

Traganza, E. D., V. M. Silva, D. M. Austin, W. E. Hanson, and S. H. Bronsink, 19°3: Nutrient mapping and recurrence of coastal upwelling centers by satellite remote sensing: its implication to primary production and the sediment record. *Coastal Upwelling: Its Sediment Record*. Eds. E. Seuss and J. Thiede. Plenum Press, pp. 61-83.

Washburn, L., D. C. Kadko, B. H. Jones, T. Hayward, P. M. Kosro, T. P. Stanton, A. Huyer, S. R. Ramp, and T. Cowles, 1990: Water mass subduction and the transport of phytoplankton in a coastal upwelling system. (manuscript)

INITIAL DISTRIBUTION LIST

	No. Copies
1. Defense Technical Information Center Cameron Station Alexandria, VA 22304-6145	2
2. Library, Code 52 Naval Postgraduate School Monterey, CA 93943-5000	2
3. Chairman (Code OC/Co) Department of Oceanography Naval Postgraduate School Monterey, CA 93943-5000	1
4. Chairman (Code MR/Hy) Department of Meteorology Naval Postgraduate School Monterey, CA 93943-5000	1
5. Professor Timothy P. Stanton (Code OC/St) Department of Oceanography Naval Postgraduate School Monterey, CA 93943-5000	1
6. Professor Steven R. Ramp (Code OC/Ra) Department of Oceanography Naval Postgraduate School Monterey, CA 93943-5000	1
7. Professor I. M. Navon Department of Mathematics Florida State University Tallahassee, FL 32306-4052	1

8. Dr. Francisco Chavez — 1
MBARI
160 Central Avenue
Pacific Grove, CA 93950

9. Dr. Libe Washburn — 1
Department of Geography
University of California
Santa Barbara, CA 93106

10. Commander — 1
Naval Oceanography Command
Stennis Space Center
MS 39529-5000

11. Commanding Officer — 1
Fleet Numerical Oceanography Center
Monterey, CA 93943-5005

12. LCDR Roland E. de Jesus — 1
NOCC/JTWC COMNAVMARIANAS
Box 12
FPO San Francisco, CA 96630

13. LT. James R. Mallette, Jr. — 1
519 Dorado Drive
Fort Walton Beach, FL 32548